Enhanced Upconversion Photoluminescence by Novel Plasmonic Structures

The author declare that the work presented in this thesis is by his own. Where information has been derived from other sources, it was confirmed that this had been indicated in the thesis.

Heng Qin

2018

Department of Materials

Imperial College London

Supervised by Dr. Fang Xie and Professor Mary Ryan

This thesis is submitted in fulfilment of the requirements for the degree of Doctor of Philosophy (PhD), Imperial College London

Declaration of Originality

I declare that this work is my own and that any references to other work are appropriately referenced. Some of the work in this thesis has been published in the following journal article[1,2]:

1. Qin, H. *et al.* Enhancement of the upconversion photoluminescence of hexagonal phase $NaYF_4:Yb^{3+}$, Er^{3+} nanoparticles by mesoporous gold films. Physical Chemistry Chemical Physics **19**, 19159-19167, doi:10.1039/C7CP01959A (2017).
2. Qin, H. et al. Tuning the upconversion photoluminescence lifetimes of $NaYF_4:Yb^{3+}$, Er^{3+} through lanthanide Gd^{3+} doping. Scientific Reports 8, 12683, doi:10.1038/s41598-018-30983-9 (2018).

Journal articles in preparation:

1. Au nanostructured arrays for the UCPL enhancement of $NaYF4:Yb^{3+}$, Er^{3+} (In preparation)
2. Plasmonic Enhanced Triplet-Triplet Annihilation Upconversion for Broadband Photocatalysis (In submission stage)

Declaration of Copyright

Abstract

The emerging field of plasmon-enhanced upconversion photoluminescence has a significant impact on a variety of technologies, including high-efficiency solar energy systems and biotechnology. To date, the upconversion efficiency of best reported rare-earth doped upconversion nanoparticles cannot meet the requirements of practical utilizations in these fields. Therefore, it is of great significance to find new approaches for the enhancement of upconversion efficiency. This thesis mainly aims to explore the enhanced upconversion photoluminescence by several novel plasmonic nanostructures.

In this PhD work, I first studied the properties of rare-earth doped upconversion nanomaterials, which are capable of the spectral conversion of the otherwise lost sub-band-gap photons from the solar spectrum. The extra Gd^{3+} ion doping strategy was introduced in the hydrothermal synthesis process, which can provide an approach to tune the geometry and upconversion efficiency of upconversion nanoparticles (UCNPs). To achieve higher upconversion efficiency, advances in the experimental improvements in plasmon-enhanced upconversion photoluminescence (UCPL) efficiency are explored, by using Au mesoporous film, Au nanotriangle array or nanohole array substrates for the enhancement of upconversion photoluminescence. It is demonstrated that the best plasmonic nanostructures can achieve about 360 times UCPL enhancement. These experimental results demonstrated the great potential of the plasmonic effect for UCPL enhancement. Furthermore, a triplet-triplet annihilation based upconversion nanoparticles (TTA-UCNPs) were synthesized, which have much higher intrinsic upconversion efficiency than the rare-earth based upconversion nanoparticles. A plasmon-enhanced upconversion photoluminescence substrate was designed for high performance photocatalysis applications under solar simulator (AM 1.5 G) irradiation. Five times faster photocatalytic activity rate was achieved by this plasmonic/TTA-UCNPs/Au@TiO_2 system, which demonstrates great value of plasmonic and upconversion mechanisms.

The combination of excellent plasmonic substrate and high efficiency TTA-UCNPs makes it possible for the realization of industrial level applications of the plasmonic and upconversion in the photocatalytic field.

This work is dedicated to my family and my parents for their endless support and love;

This work is also dedicated to the memories of my friends and sharing so many memories together.

Acknowledgements

My highest gratitude goes to my supervisor, Dr. Fang Xie for her continuous support and guidance for doing research during my PhD study. Her dedication, hard-work and creativity are the landmarks for me to follow in life. I would like to especially thank her encouragement that allowed to reach the end. I extend thanks and appreciation to my co-supervisor Prof. Mary Ryan for inspiring the passion for this field of science in me. Her guidance always encouraged me, and our scientific discussions provide me various research directions.

I would like to express my deepest thanks to my parents who have always supported me along this journey, no matter what difficulties happened. I would have never made it this far without their unconditional love and support. I owe them everything I have and much more.

I would like to thank my group members, Jing Pang, Daniel Darvill, Xu Wu, Danyang Wu, Xiangyu Xie, Qianfan Jiang, Ioannis G. Theodorou, Jawad ZAR, Lukas Malms, Dick Ferieno Firdaus, Kangyu Ji, Xueming Xia. We spent wonderful times in the labs, did research and shared so many funny moments. You always present for helping me throughout my time at Imperial College London.

I am also grateful to my colleagues from other groups, Ahmed Shamso, Weixin Song, Tiesheng Wang, Dr. Yi. Li, Dr. Andrei P. Mihai, Dr. Peter Petrov, Dr. Mark Oxborrow, Dr. Juna Sathian, Dr. Anthony Centeno. Your ideas, suggestions and helps really pushed my research forward. It is my honor to have worked with you, from whom I have learned a lot of research skills and how to think different.

With a special mention to my friends and colleagues outside Imperial College London who spent valuable times and shared novel insights and emotions with me: Fei Gao, Hongchao Xie, Yi Liao, Linan Tian,Yue Wang, Jinlong Wang, Linxu Du, Jiajia Song. Your wisdom, enthusiasm, optimism and hard-working inspired me so much. Without the memories with you, my life would be totally different.

Finally, special thanks to Dr. Fang Xie's Group at Imperial College London, where I spent the last four years in my life. This is the most special place that I will never forget.

Table of Content

List of Abbreviation

APTES: aminopropyltriethoxysilane

CB: conductive band

DDA: discrete dipole approximation

DI: deionized

ET: energy transfer

ESA: excited-state absorption

ETU: energy-transfer upconversion

FRET: fluorescence resonance energy transfer

FDTD: finite-difference time-domain

E_{gap}: band gap energy

EDS: energy-dispersive X-ray spectroscopy

EOT: extraordinary optical transmission

LSPR: localized surface plasmon resonance

MPTMS: (3-Mercaptopropyl)triethoxysilane

NIR: near-infrared

NSL: nanosphere lithography

MO: methylene orange

ODE: octadecene

PA: photon avalanche

PL: photoluminescence

PS: polystyrene

RE: rare earth

SEM: scanning electron microscopy

SPP: surface plasmon polariton

SB: Schottky barrier

TEM: transmission electron microscopy

TCSPC: time-correlated single-photon counting

TTA-UCNPs: triplet-triplet upconversion nanoparticles

TTA-UCPL: triplet-triplet annihilation upconversion photoluminescence

UV: ultra-violet

UCNPs: upconversion nanoparticles

UCPL: upconversion photoluminescence

UCQY: upconversion quantum yield

VIS: visible

VB: valence band

XRD: X-ray (powder) diffraction

List of Figures

List of Tables

Chapter 1 Introduction

Our global energy system that relies on fossil fuels and nuclear energy is facing great challenges. On one hand, it is estimated that the fossil fuel demands may exceed annual production within the next two decades.[1] On the other hand, to meet the increased global energy demands by large-scale exploitation of fossil fuel and nuclear energy would contribute to a number of severe environmental, economic and social threats.[2] To tackle these issues, renewable energy sources like wind power, hydro power, biomass, and solar energy are urgently needed to play a major role in the near future. Sunlight offers our planet 10000 times more energy than the global daily consumption;[3] it appears to be virtually unlimited. Various strategies have been proposed to achieve high performance solar energy systems. Among them, photon upconversion, converting otherwise lost photons into usable energy, and plasmonic enhancement are two promising approaches to enhance light harvesting and hence the performance of solar photocatalytic systems.

In this thesis, plasmonic enhanced upconversion was investigated by using various designs of plasmonic nanostructures. Two upconversion systems were investigated: 1) Sodium Y fluoride doped with Yb and Er ions ($NaFY_4$:Yb, Er); 2) triplet-triplet annihilation upconversion (TTA-UC). Significance plasmonic enhancement were observed for both systems. TTA was further investigated in a photocatalytic system, 5-fold enhancement of photocatalytic rate were achieved with the designer plasmonic system, using AM1.5G. Chapter 1 in this thesis briefly outlines the motivation and thesis structure. A literature review of the upconversion, plasmonic and photocatalysis are provided in chapter 2. Theoretical and experimental studies for plasmon-enhanced upconversion are illustrated in the literature review. In chapter 3, the synthesis and properties of upconversion nanoparticles by hydrothermal method was investigated. A novel Gd^{3+} doping strategy in $NaYF_4$ host materials, realized tuning of upconversion photoluminescence (UCPL)

lifetimes at selective emissions was adopted. Time-correlated single-photon counting (TCSPC), was applied to measure the photoluminescence lifetimes accurately. We demonstrated the large dynamic range of lifetimes of upconversion nanoparticles with good upconversion quantum yields, mainly owing to the dominance of highly efficient energy transfer upconversion mechanism. The exceptional tuneable properties of upconversion materials also allows great potential for them to be utilized in biotechnology and life science.

In chapter 4, novel three-dimensional (3D) mesoporous gold films were fabricated by a low-cost and facile dealloying approach to improve the upconversion photoluminescence efficiency. The mesoporous Au films exhibit good chemical stability, large-area uniformity and abundant distribution of porous nanospaces. Varying the time of the dealloying process leads to modification of pore size distribution, surface roughness and residual Ag content, resulting in effective tuning the wavelength of the broadband localized surface plasmon resonance (LSPR). Enhancement factors were identified to be a function of the dealloying time. With the optimized upconversion photoluminescence enhancement, a 41-fold increase was achieved by the mesoporous gold substrate which had been dealloyed for 8 days.

Subsequently, chapter 5 was motivated by the low-cost and versatile technique-nanosphere lithography, which can be applied to achieve well-defined, periodic and large area Au nanostructure arrays such as nanotriangle array and nanohole array, etc. By improving the technique and combining with other technique including oxygen plasma etching, surface modification of upconversion nanoparticles, the LSPR and SPP bands can be precisely tuned, and the distribution of UCNPs on Au nanostructure was optimized. In our study, significant 360-fold upconversion photoluminescence enhancement was realized by flat Au/10 nm SiO_2 spacer/Au nanotriangle array architecture. These results pave the way to overcome

the limitation of poor upconversion efficiency for widespread practical applications in life sciences and energy applications.

In chapter 6, the application of TTA-UC nanoparticles coupled with plasmonic nanostructures for TiO_2 photocatalysis enhancement are studied. The practical applicability of the combination of upconversion and plasmonics remains challenging in the oxygen-rich aqueous phase environment at sunlight excitation. In this chapter, we developed an Au nanohole film/TTA-UCNPs/Au@TiO_2 architecture, which can be applied to improve the photocatalytic performance of semiconductors. It was demonstrated that triplet-triplet annihilation upconversion photoluminescence (TTA-UCPL) can be significantly enhanced by Au nanohole array substrate by a factor of 15. Furthermore, increased TTA-UCPL, hot electrons generated from surface plasmon decay of Au nanostructure and the plasmon-induced resonant energy transfer (PIRET) from Au to TiO_2 can enhance the photocatalytic activity of Au@TiO_2 by a factor of 5.

In the final chapter (Chapter 7), a summary of this PhD project is given and followed by outlooks and future work. The results pave the way for the exploration of plasmon-enhanced upconversion photoluminescence, and their practical application for high performance photocatalysis under sunlight.

Chapter 2 Literature Review

This review aims to survey the theoretical foundations of upconversion and the major relevant studies in the field of plasmon-enhanced upconversion. Besides, basic mechanisms and recent experimental advances at plasmon-enhanced upconversion and their application in photocatalysis are reviewed.

2.1 Upconversion Nanomaterials

The term upconversion refers to nonlinear anti-stokes optical processes that a successive absorption of two or more lower-energy photons leads to the emission of one higher-energy photon. The origin of the research on upconversion can be traced back to an idea of Bloembergen in 1959, who proposed an infrared quantum counters in ion-doped systems.[1] The upconversion phenomenon was subsequently discovered by Auzel in the 1960s.[2] Ever since then, enthusiasm for the research on lanthanide-doped upconversion nanoparticles has been greatly driven by their diverse potential applications.

2.1.1 Synthesis Methods

There are a number of synthesis routes for the upconversion nanoparticles, such as hydrothermal synthesis, thermal decomposition, sol-gel processing, etc. For simplicity, this section only reviews hydrothermal synthesis and thermal decomposition method.

2.1.1.1 Hydrothermal method

Hydrothermal method can be described by any heterogeneous reactions within high pressure and temperature solvents to dissolve and recrystallize materials. This method has the capability to create highly crystalline phases at relatively low temperature and simultaneously implement a set of reactions. Therefore, the size, shape, phase and stoichiometric composition can be precisely controlled by hydrothermal method. However, one notable disadvantage is the need for specialized reaction vessel

named as autoclave, which may lead to safety risks. Typically, appropriate solvents, reaction precursors, and surfactants are homogeneously mixed and then heated in an autoclave. The control of the crystalline phase, size and the functional group on the surface of UCNPs can be realized by surfactants selections.

2.1.1.2 Thermal decomposition method

Another widely adopted synthesis method is called thermal decomposition method. The method can produce high yield monodispersed UCNPs, and the as-synthesized UCNPs can be in well-controlled size and shape at given experimental conditions. During the thermal decomposition process, rare-earth precursors are dissolved in high-boiling point organic solvents (e.g. oleic acid (OA), oleyamine (OM), and 1-octadecne (ODE)) at temperature exceeding 300 ℃. Mai *et al.* realized the synthesis of monodispersed cubic and hexagonal phase $NaYF_4$ by thermal decomposition method. They discovered the reaction time and temperature are important to overcome the free energy barriers for the phase transformation from cubic phase to hexagonal phase.[6] The drawbacks of this method are the air-sensitive condition during the reaction and the toxic by-products generation.[7]

2.1.2 Selection of Host, Activator and Sensitizer for Lanthanide UCNPs

In general, lanthanide upconverting nanocrystals are comprised of an inorganic host (i.e. fluoride phosphors) and rare earth dopant ions (i.e.Yb^{3+}, Er^{3+},Tm^{3+}, etc.). The choice of the host materials and lanthanide ions as activators and sensitizers has a strong impact on the upconversion process. The optimization of the upconversion process has been explored by combining a variety of nanoscale host crystals and dopants. Some key considerations are the determination of distance between dopant ions, the types of anions surrounding the dopants and the relative spatial position.[8] Furthermore, ideal host material should not only have a lattice well-matched with doped-ions, but also with low lattice phonon energies in

order to suppress the non-radiative loss. Due to the stretching vibration of the host lattice of oxides, their phonon energies are relatively high and generally larger than 500 cm^{-1}. Compared with heavy halides and oxides, fluorides usually exhibit both good chemical stability and low lattice photon energies (typically 350 cm^{-1}). Currently, the most efficient upconversion nanomaterial is determined as $NaYF_4$ co-doped with Er^{3+}or Yb^{3+}, Tm^{3+}. It is discovered that hexagonal-phase $\beta - NaYF_4$: Yb^{3+} Er^{3+} bulk materials have upconversion efficiencies about 10 times more than their cubic-phase counterparts.[9] Yb^{3+} ions have an absorption cross-section larger than those of lanthanide ions. There is a perfect resonance between the $^2F_{7/2}$ - $^2F_{5/2}$ energy transition of Yb^{3+} and many f-f transitions of lanthanide ions (i.e.$Er^{3+}, Tm^{3+}, Ho^{3+}$). This resonance facilities efficient energy transfer (ET) processes between Yb^{3+} and lanthanide ions.

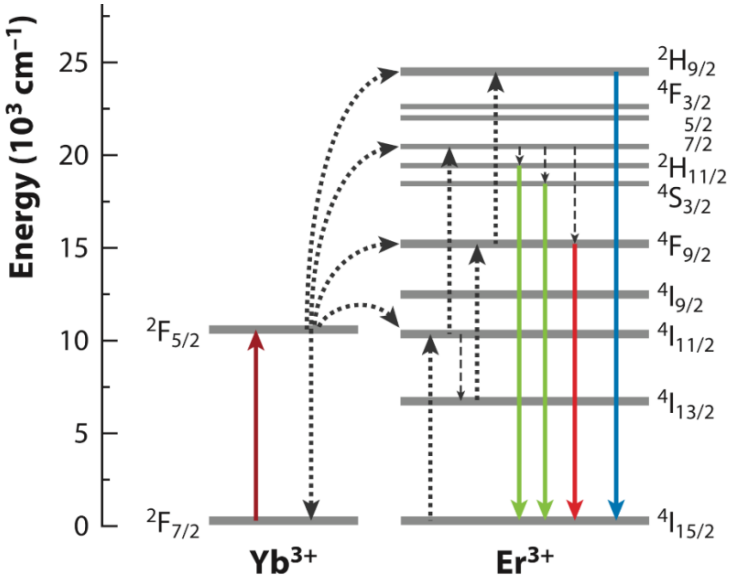

Figure 2- 1 Upconversion mechanism of the UCNPs co-doped with lanthanide Yb^{3+}, Er^{3+}.[10] This figure is reprinted from ref-10.

Figure 2-1 illustrates the visible upconversion emission of Yb^{3+}, Er^{3+} co-doped UCNPs. The UCPL arises from 4f-4f orbital electronic transitions within an individual lanthanide ion, and the outer 5s and 5p shells have a shielding effect on 4f electrons to minimize the appearance of photobleaching. Green emissions (520nm, 540nm) are linked to the transitions from the $^2H_{11/2}$ and $^4S_{3/2}$ to the $^4I_{15/2}$ (ground state). A red emission peak at 660nm is attributed to the $^4F_{9/2}$ to ground state transition. Likewise, upconversion emission at 451nm, 646nm and 800nm can be observed for Yb^{3+}, Tm^{3+}co-doped $NaYF_4$ nanoparticles.

2.1.3 Upconversion Mechanism of Lanthanide-Doped Nanoparticles

As trivalent lanthanide ions have abundant energy-level structure (Dieke diagram), they are selected to be the prime candidates to realize spectral conversion with high efficiency. In general, three main upconversion processes have been identified, including excited-state absorption (ESA), energy-transfer upconversion (ETU), and photon avalanche (PA).[11] All of these processes sequentially absorb two or more photons. In lanthanide based UCNPs, the most efficient mechanisms are some combinations of ESA and ETU. Since photon avalanche is uncommon, the following discussion will be focused on ESA and ETU.

Excited-state absorption (ESA) is an appropriate pumping process for single ion doped UCNPs. In a general ESA energy scheme, two photons are absorbed successively under a suitable excitation. It requires that the energy of transition from the ground state 1 to the excited metastable state 2 is resonant with the excitation energy. This resonant pumping energy immediately allows the successive excitation from metastable state 2 to higher excited state 3. Subsequently, populated photon drops from excited state 3 to ground state 1, which results in the upconversion emission. It is essential to keep a low concentration of active ions to avoid cross-relaxation between luminescent centers. In addition, it is recognized that the ESA process can be enhanced by suppressing the transfer losses through cross-relaxation.[12]

It is acknowledged that the most efficient upconversion process in rare earth ions doped systems is energy transfer upconversion (ETU). The ETU is similar to ESA as both processes involve the successive absorption of two photons to excite the metastable state 2. However, there is a key difference between ESA and ETU. In ETU process, two (or more) ions in close vicinity are involved in the upconversion process. Energy transfer results in one ion to be found in a higher excited state whereas the other ion in a lower excited state.

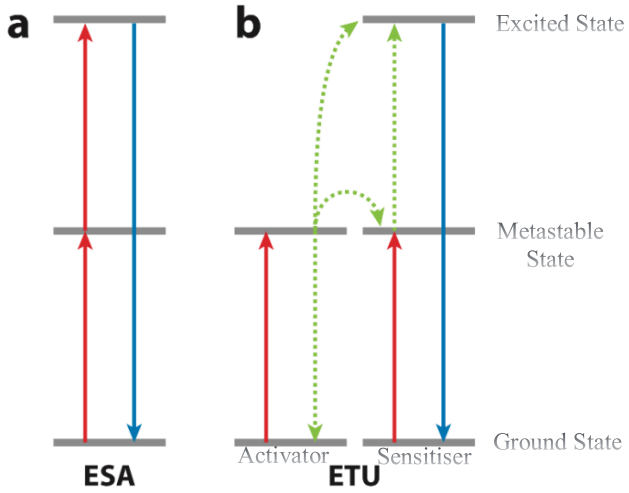

Figure 2- 2 Basic energy transfer mechanisms of rare earth–related upconversion emissions: (a) excited state absorption (ESA), (b) energy transfer upconversion (ETU).[13]

Five types of ETU process are identified as (1) Energy transfer followed by excited-state absorption (2) Successive energy transfers (3) Cross relaxation upconversion (4) Cooperative sensitization (5) Cooperative luminescence. For the first three mechanisms, energy-transfer process from sensitizer to activator followed by excited-state absorption promotes the metastable state 2 to excited state 3 in the activator. While for the latter two mechanisms, cooperative interplays of energy transfer between ions produce the upconversion emissions. By measuring the photoluminescence decay curve under a pulsed excitation, the dominating upconversion pathway can be determined. The ESA process is associated with

a simple exponential curve without a rise time. In contrast, the ETU process displays a peak in the decay curve，which is caused by the slower energy transfer step. This decay curve will be studied in chapter 3. It is also recognized that only one pump is essential for ETU. Importantly, the efficiency of an energy transfer upconversion strongly depends on the concentration of the neighboring ions.

2.1.4 Nonlinear Nature of Upconversion

Comprehensive studies on the nonlinear effect of upconversion in lanthanide-based systems have been reported by Pollnau et al.[14] and Suyver et al.[15] In brief, the luminescence of upconversion is owing to the intra 4f-4f orbital electronic-dipole transitions of lanthanide ions. These features of lanthanide ions lead to the nonlinear nature of upconversion photoluminescence (UCPL), which generally is a function of the excitation density[16]

$$I_{uc} = KP^{n} \qquad \text{(Equ 2-1)}$$

Where I_{uc} represents the intensity of upconversion photoluminescence, K refers to a material coefficient, P is the power of laser, and n is denoted as the number of the excitation photons required to produce the upconversion photoluminescence. The value of n could be determined by the log-log relation of equation 2-1 associated with the upconversion photoluminescence peaks at a very low density of excitation.[17] At high excitation density, non-radiative relaxations increase and the competition processes between the decay rate and the upconverted rate at the metastable energy levels lead to smaller n values. This is termed as the saturation effect, which must be carefully avoided when distinguishing the photon processes of upconversion photoluminescence peaks.

2.1.5 Efficiency of Upconversion Materials

The upconversion quantum yield (UCQY) is one of the most significant quantities for various applications, especially for solar energy spectral conversion. As noted above, the efficiency of an upconversion process is strongly linked to the density of incident excitation. In literature, there are two common definitions of the UCQY: one is the internal UCQY (iUCQY) and another one is the external UCQY (eUCQY). The eUCQY[18] is defined as the photon flux of upconverted photons emitted by the upconverter divided by the photon flux of the photons incident on the upconverter sample,

$$\text{eUCQY} = \frac{\text{upconverted photon flux}}{\text{incident photon flux}} \qquad \text{(Equ 2-2)}$$

As external UCQY describes the overall efficiency of the upconversion process, it provides more useful information for most applications. However, in literature the iUCQY is a more popular term, which is defined as the fraction of the photon flux of upconverted photons divided by the photon flux of absorbed photons，

$$\text{iUCQY} = \frac{\text{upconverted photon flux}}{\text{absorbed photon flux}} = \frac{1}{\text{absorptance}}\ \text{eUCQY} = \frac{1}{\text{absorptance}}\frac{I_{uc}}{P} \qquad \text{(Equ 2-3)}$$

The iUCQY is also one of key factors, reflecting intrinsic efficiency of the UC process. By inserting (Equ 2-1) into (Equ 2-3), a new relation can be obtained,

$$\text{iUCQY} \propto P^{n-1} \qquad \text{(Equ 2-4)}$$

To sum up, we can also find a relationship between the efficiencies of solar cells and UCQY.

$$\eta \propto I_{sc}^{UC} \propto P_{in}^{n} \propto \text{iUCQY} \propto \text{eUCQY} \qquad \text{(Equ 2-5)}$$

It can be recognized that the iUCQY and eUCQY are linked by a parameter absorbance of the sample. Due to the low absorption cross-section of rare earth ions, internal UCQY is always dramatically greater than the external UCQY. In addition, since the emission of one photon in the upconversion process demands at least two lower energy photons, the value of UCQY will always be lower than 0.5. It is

noteworthy that a common issue is the lack of transparency in the determination of the iUCQY and eUCQY in literature. In 2013，a detailed protocol for transparent solutions was published in order to achieve benchmark standard to determine the upconversion efficiency.[19] To date, however, it seems that reliability and uncertainty are still a general existing challenge.

Until now, poor upconversion efficiencies of UCNPs remain the most critical limitation for a range of applications. During the past 5 years, a rising number of papers have reported the data of upconversion efficiency. Van Veggel *et al.* measured the absolute efficiencies of UCNPs by using the barium sulfate-coated integrating sphere.[20] The samples were held in a quartz curvet placed in the center of the integrating sphere and were illuminated by a 980nm laser. The sample holder was covered by baffles to avoid the collection of scattered excitation or emission light before scattering off the inside of the sphere. In addition, Cohen *et al.* reported protein-sized (4.5nm-15nm) hexagonal $\beta-NaYF_4$：Yb^{3+}, Er^{3+} nanocrystals with a QY of 0.18%.[21] Prasad *et al.* reported $NaYF_4$ co-doped with Yb^{3+} and Er^{3+}, reaching a QY up to 1.2% upon a 1490 nm excitation,[22] which is about 4 times stronger than the upconversion photoluminescence efficiency reported to date for 100nm $\beta-NaYF_4$: Yb^{3+}, Er^{3+} illuminated by 980nm laser. In Fischer's work，$\beta-NaYF_4$: Er^{3+} 25% upconversion nanoparticles showed the iUCQY of 11.96% for 1523nm emission under excitation intensity of 0.402 $W\cdot cm^{-2}$. At a lower excitation intensity of 0.016 $W\cdot cm^{-2}$, iUCQY was determined to be 1.99%. The iUCQY means internal upconversion quantum yield, higher excitation intensity means more photons can be used to excite upconversion nanoparticles. However, if eUCQY was calculated, higher excitation intensity should give lower eUCQY, since a large portion of excitation photons cannot be absorbed by upconversion nanoparticles. Although this is one of the highest efficiency values to date in literature, the method of measurement and the detection wavelength are different to other work. Since most of the optical characterizations of UCQY were based on home-made

instruments, the results of the UCNPs efficiency should be carefully interpreted. Indeed, further studies of the enhancement of UCQY of UCNPs are needed to fulfill their practical applications in the future.

2.2 Plasmon-Enhanced Upconversion

It has been well studied that noble metal nanoparticles exhibit novel optical properties. Surface plasmon resonance (SPR) refers to collective and coherent oscillation of conduction electrons in the surface of metal nanoparticles, which is stimulated by the electric field of incident excitation.[23] The resonance occurs when the natural frequency of oscillating surface electrons in metal nanostructures matches the frequency of incident light, producing an enhancement of the electric field. This intense local electric field results in the enhancement of linear and nonlinear optical effect. Plasmonic nanostructures support two types of SPR: 1) Localized surface plasmon resonance (LSPR), in which oscillating electric dipoles are confined within nanoparticles. 2) Surface plasmon polaritons (SPP), in which the plasmon wave propagates along the metal surface.

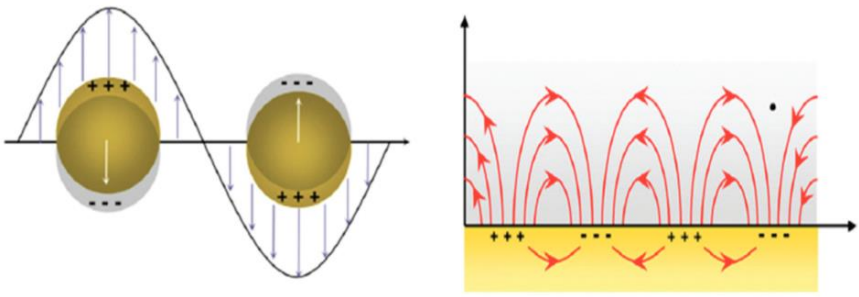

Figure 2- 3 Schematic illustrations showing the mechanisms of localized surface plasmon resonance (LSPR) (oscillating induced dipole, left side) produced by metal and surface plasmon wave propagating (SPP) along a metal-dielectric interface (right side). This figure is reprinted from ref-23.

The plasmon oscillation will be confined within the metal nanoparticle if the mean free path length of electrons is shorter than the particle size. At a certain frequency, the nanoparticle acts as a resonant cavity,

in which an electron is forced to oscillate due to the incident electric field and the Coulomb attraction between the nucleus and the electron. Then the nanoparticles can effectively store the incident sunlight energy in a LSPR mode (Figure 2-3).

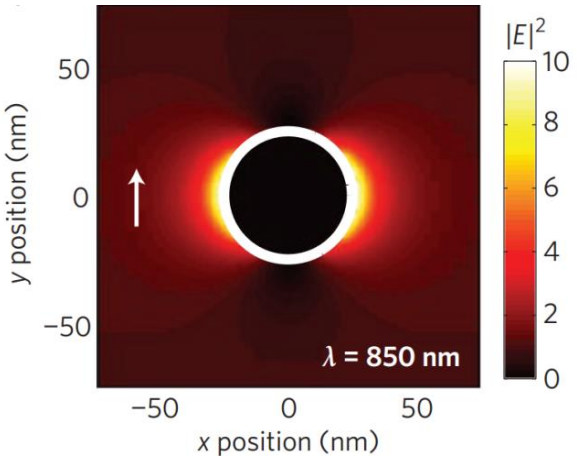

Figure 2- 4 Diagram for a localized surface plasmon mode. An intense near-field electric intensity is closed to the surface of metal nanoparticles.[24]

Surface plasmon polaritons are the propagation of surface electromagnetic waves in the direction along the metal/dielectric interfaces.[25] The resonance occurs when the frequency of incident photons equals the natural oscillating frequency of surface electrons. These oscillations are quite sensitive to any modification of the interface. By judicious engineering of the metallic/dielectric structures, the concentrated and folded light within a thin semiconductor layer can lead to the enhancement of the light absorption.[24] In addition, the SPR can be tuned from visible to near infrared range by modifying size shape, composition and surroundings of nanostructures, favoring a specific optical process. Despite all these unique properties, more systematic studies are demanded to realize the advantageous plasmonic in upconversion enhancement and solar applications.

In lanthanide ions doped UCNPs, the upconversion emission intensity can be calculated by equation:

$$I=\varphi\sigma_s\eta_{ET}\varphi_A \qquad \text{(Equ 2-6)}$$

Where φ is the photon flux of the incident excitation source, σ_s is the absorption cross-section of the sensitizer ions, η_{ET} represents the efficiency of the energy transfer from the sensitizer (i.e. Yb) to the activator (i.e. Er), and the luminescence quantum yield of the activator is denoted by φ_A. The plasmonic nanostructure can greatly influence the luminescence of nearby UCNPs (emitter) in three main ways:[26] (1) Enhancing the absorption of the sensitizer by locally concentrating the incident field through electric-field coupling. (absorption enhancement) (2) Enhancing the radiative decay rate of the activator (emission enhancement). On the other hand, the plasmons can possibly quench emission by increasing the nonradiative decay. (3) Increasing the energy-transfer (ET) from the sensitizer to activator. These three ways can interplay with each other if there are spectral overlap between the resonances, absorption/emission frequencies, polarization, and incident excitation.

For upconversion photoluminescence, surface plasmon resonance (SPR) can induce a strong local electric field (E).[27] The photon flux (φ) in equation 2-6 is proportional to the square of the electric field (E),

$$\varphi \propto E^2 \qquad \text{(Equ 2-7)}$$

When a UC nanoparticle is located at the vicinity of a metallic structure, an effective coupling exists between the transition dipole of the UCNP and the SPR induced electric field. Hence the light harvesting of sensitizer ions can be improved, which leads to plasmon-enhanced upconversion. A theoretical study demonstrated that the luminescence enhancement of upconversion is proportional to the fourth power of the local field enhancement, $(E_{loc}/E_0)^4$, in contrast to the square proportion described by Equ. 2-7 [28] Another upconversion plasmonic enhancement depends on the increased radiative decay rate of the activator doped in a UCNP. The radiative decay rate is influenced by a great deal of coupling between the electrons and phonons in metal nanoparticles. This kind of coupling modifies the photonic-mode density of UCPL. The quantum yield (φ_A) and the lifetime of UCPL can be described by two equations:

$$\varphi_A = \frac{k_r + k_m}{k_r + k_m + k_{nr}} \quad \text{(Equ 2-8)}$$

$$\tau = \frac{1}{k_r + k_m + k_{nr}} \quad \text{(Equ 2-9)}$$

Where $k_r, k_m,$ and k_{nr} are the radiative decay rate, metal induced radiative decay rate and non-radiative decay rate, respectively.[29] The coupling effect of the noble metal nanoparticles is very sensitive to distance. Accordingly, the quenching effect refers to a direct electron transfer (or FRET) when a UCNP and a noble metal particle are placed too closed to each other (around 5nm). Förster resonance energy transfer (FRET), is a mechanism describing energy transfer between two light-sensitive molecules. This effect indicates that a spacer thicker than 5nm is needed to enhance the UCQY.

To favor a specific optical process, the wavelength of surface plasmon resonance is of great importance. When the particle size is considered to be much smaller than the wavelength of incident light, the quasistatic approximation can be used to study the dipole plasmon resonance of metallic nanostructures. This approximation treats the electric field as constant, thus electrodynamics questions are simplified to electrostatic ones. The frequency and strength of the dipole plasmon resonance depends on $\varepsilon(\omega)$, wavelength-dependent dielectric function of the particle; ε_d, the dielectric constant of the local medium; R, the particle size, which determines the total number of electrons in the oscillating dipole. Thus, the polarizability for a nanosphere of radius R is:[30]

$$\alpha = 4\pi\varepsilon_0 R^3 \frac{\varepsilon - \varepsilon_d}{\varepsilon + 2\varepsilon_d} \quad \text{(Equ 2-10)}$$

Equation 2-10 indicates that the wavelength range of SPR is a function of the composition, particle's size and shape, as well as local environment. Consequently, optical tuneability of SPR can be achieved by modifying the surface dielectric particle size and particle shape. For instance, by embedding gold or silver nanoparticles in SiO_2, Si_3N_4 or Si,[31] the SPR can be tuned over the entire 500nm-1500nm spectral range. Anisotropic nanoparticles can also be tuned from the visible range to the NIR. In a classical core-shell

structure, the optical resonance can be tuned by varying the ratio of the core/shell radius. Moreover, the shape of particles also plays a significant part in determining the plasmon mode. Nanorods can exhibit transverse plasmon modes and longitudinal plasmon modes, respectively. Longitudinal modes of Au nanorods can be easily red-shifted from 700nm to 1100nm.[32] By contrast，the transverse modes show a weaker resonance at 520nm and can only be slowly shifted to 500nm.[33]

2.3 Experimental Studies on Plasmon-Enhanced Upconversion

To date, a number of plasmonic geometries have been investigated to enhance the upconversion luminescence. Normally experienced with newly emerging research topics such as research on the efficiency of upconversion, there is also a challenging issue to compare different types of work due to the lack of a detailed protocol in experimental parameters. As previously mentioned, upconversion is a non-linear process, which means the UCQY of upconversion material itself increases at stronger power densities. This nonlinear effect in fact allows absorption-matched plasmons to be more effective in boosting upconversion at relatively weak incident irradiance. To illustrate this phenomenon, Lu et al. compared the plasmon-enhanced upconversion in a well-designed silver gratings geometry at distinguished incident power density. Clearly, at incident power densities above $40\mathrm{kW/cm^2}$ only offered 4.4X enhancement, which was much lower than 38.8X enhancement observed at below $2\mathrm{kW/cm^2}$.[34] To date, one reasonable way to assess plasmon-enhanced upconversion is to normalize the intrinsic upconversion efficiency (UCQY) of the compared upconversion materials beforehand. Furthermore, ETU is a complicated mechanism involving multiple steps with distinguished processes. It has been proved that light absorption, emission and Forster resonance energy transfer (FRET) are strongly sensitive to the enhanced local electric field.[34] Taking above-mentioned significant caveats into account, figure 2-5

highlights a number of interesting studies involving diverse geometries. This figure serves as a visual summary of the plasmonic enhancements achieved for two-photon upconversion in literature.

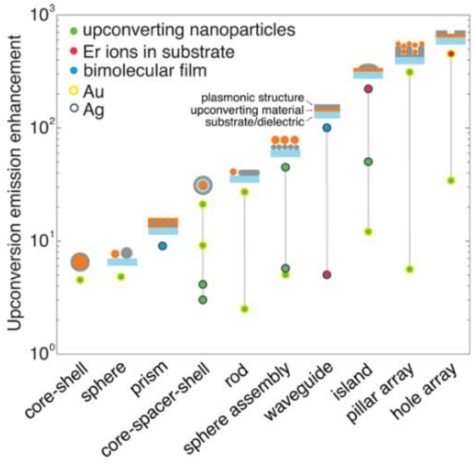

Figure 2- 5 A number of plasmonic geometries reported for the enhancements of two-photon upconversion. Green dots represent lanthanide-doped upconverting nanoparticles. Red dots and blue dots represent erbium-doped upconverting nanoparticles and bimolecular films, respectively. Yellow (Au) and gray (Ag) rings indicate the plasmonic materials. This figure is reproduced from ref 26. As mentioned above, lanthanide-doped systems are utilized as the most popular UCNPs and $NaYF_4$：Yb^{3+}, Er^{3+} has been identified as the material with the highest UCQY.[35] As a result, the table below will mainly focus on the studies of the enhancement on $NaYF_4$：Yb^{3+}, Er^{3+} with emissions at 540nm or 660nm upon excitation at 980nm continuous wave laser， which dedicates to explore the plasmon-enhanced upconversion influenced by the role of spectral overlap between the plasmonic resonance and emitter, power density of incident irradiance, metallic nanostructures and distinct size of $NaYF_4$：Yb^{3+}, Er^{3+}, etc.

Table 2- 1 Summarize of the plasmon-enhanced $NaYF_4$ nanoparticles, with information on plasmonic nanostructures, enhancement factors, emissions of surface plasmon resonance, particle size distribution, excitation conditions of representative studies. CSS means core shell structure.

Structure	Emission Enhancement at 540nm or at other wavelengths(nm)	Plasmon resonance	$NaYF_4$ Size	Laser density	Plasmonic/ spacer	Ref.
Pillars (Gratings)	540-100X 660-301X	920nm	25nm	100 W/cm^2	Au	36
	2.29X(red) 2.78X(green)	998nm	65nm	CW980 3mW	Au	37
	25.9X (red)	N/A	N/A	980nm	Au	38
	540-32.6X 660-34.0X	930nm	70nm	1.06W, 0.05 W/mm^2	Au 30nm layer on glass	39
	540-30X 650-45X	420nm (Ag)	30nm	1.06W 0.05 W/mm^2	Ag	40
Holes array	540-5.2X 650-3.5X	529 (Au)	30nm	1.06W 0.05 W/mm^2	Au	40
Sphere	4.8X 2.7X (blue)	540nm	30nm	973nm 2×10^5 W/cm^2	Au 30nm/60nm	41
	522-12X, 550-5X, 652-5X	600nm	250 nm	About20-30 mW/cm^2	Au 20nm	42
	11.2X	560nm	90 nm	2 W/cm^2	Au 2.5nm	42
Islands	2.3X	420nm	30nm	980nm diode laser	Ag 8nm	43
Nanowire	4.4X	400 nm	28nm	N/A	Ag	44
CSS	2.5X	900 nm	30nm	35 mW/cm^2	Au	45
Css	0.6X	820 nm	30nm	35 mW/cm^2	Au	46
	0.5X	650 nm	30nm	35 mW/cm^2	Au	46
	0.3X	580 nm	30nm	35 mW/cm^2	Au	46
	542-14.4X,656-12.2X	420nm	45nm	400mW	Ag15nm/SiO_2 10nm	47
	542-9.5X,656-10.8X	420nm	45nm	400mW	Ag30/SiO_2 10nm	47
	545-2.6X 660-2.3X	580 nm,660 nm,820 nm, 900 nm	30nm	35mW/cm^2	Au2.8nm/SiO_2 18nm	48
	450-49.8X(5W); 20X(19W)	520 nm	160nm	19W/cm^2 5 W/cm^2	Au-10nm	49

The tunable surface plasmon resonance (SPR) of metal nanostructures can be easily achieved by adjusting the nanoparticle size, shape, composition of the plasmonic materials or surface dielectric.[50] Therefore, the wavelength of SPR can be tuned from the ultraviolet region, to visible, to the NIR of the electromagnetic spectrum. Thus, great efforts have been done to design and optimize the plasmonic configurations for the purpose of enhancing upconversion emission intensity. Extended structures include various geometries such as gratings, nanopillars/holes, islands, sphere assembly, and all of them exhibited a strong dependence on spacer thickness. In 2012, Saboktakin *et al*. reported a metal/oxide/upconversion multi-layered structure.[39] After a systematic investigation, the maximum upconversion enhancement of 45-fold occurred when a 10 nm spacer was separated between the silver film and UCNPs. In their experiment, the enhancement value dropped below 5-fold with only 5 nm modification on the spacer thickness. In the next year, the same group managed to achieve a UCPL enhancement up to a total 35-fold by designing gold nanohole arrays.[40] The nanohole array with a 930 nm SPR peak enhanced the 980 nm to 540 nm upconversion emission by 32.6-fold. This enhancement value is in line with a full field simulation, which showed a 36-fold enhanced electric field at the center of the hole. Simultaneously, the decay rate of the intermediate state was also increased by the enhanced electric field. It is widely acknowledged that silver has an intrinsic stronger plasmonic response than gold due to its plasmon resonance is free from inter-band transitions overlap.[51] However, this work indicated that silver does not consistently give better enhancement of UCPL than gold.

In 2012, Chou *et al*. observed another significant enhancement in UCPL, which further elucidate the importance of the considerably increased excitation field. They deliberately designed a 3D plasmonic antenna architecture: disk-coupled dots-on-pillar antenna array. By carefully tuning the height of the pillar, the best 310-fold UCPL over a large area was achieved.[52] More recently, Kagan's group designed a single

heterodimer with upconverting nanocrystals attached at the tips of gold nanorod.[53] The heterodimer was first illuminated under the light's polarization along the length of the rod and then under perpendicular polarization. The former illumination showed 6-fold upconversion emission, which demonstrated the plasmonic enhancement of UCPL strongly depends on the excitation light's polarizations. These studies independently highlighted the significance of studying the 3D plasmonic nanoantenna architecture.

Interestingly, when the peak of the SPR is neither emission-matched nor absorption-matched, some studies still demonstrated upconversion emission enhancement. Apart from enhancing the light absorption of the sensitizer and an improvement over the radiative decay rate of the activator, surface-plasmon coupling can also increase the energy-transfer (ET) from the sensitizer to activator. Nagpal *et al*. tested this idea by using gold pyramid arrays.[54] To decouple distinct effects of patterned metal nanostructures on upconversion photoluminescence, they compared the experimental results measured from the glass substrate, flat Au coated on glass, and as-prepared Au pyramid substrates. Accordingly, a 6-fold rate amplification in the energy transfer (ET) from Yb^{3+} to Er^{3+} in the architecture of gold pyramid arrays was reported.

2.4 Plasmonic photocatalysts and upconversion

Over the past 40 years, the main limitations of semiconductor photocatalysts such as TiO_2 and iron (III) oxide (Fe_2O_3) have been the short-range light response due to narrow band gap, poor light absorption rate, and quick recombination rate of electron/hole pairs. Recently, considerable efforts have been spent to develop plasmonic photocatalytic systems to overcome these limitations. In this part, we will introduce some studies of plasmonic photocatalysts as a potential candidate for enhancing utilization of the solar spectrum. Plasmonic photocatalysts have been regarded as a promising alternative sustainable approach for effectively harnessing sunlight to tackle global environmental and energy issues. Among the various

photocatalytic systems, plasmonic photocatalytic composites represent one of the most popular photocatalytic system since they have excellent solar energy utilization efficiency. In this system, the energy transfer from plasmonic nanoparticles to semiconductor is the key mechanism for the improvement of photocatalytic performance. Generally, semiconductor materials are characterized especially by their band gap energy (E_{gap}). The band gap energy is primarily determined by the periodic crystal lattice and the binding energy of the atom of the semiconductor.[55] Under an ideal illumination, an electron-hole pair is excited when the energy of incident photon $h\omega$ equalizes E_{gap} and electrons are subsequently populated into the conductive band. If the incident photon has energy larger than E_{gap}, the excessive energy will be transferred into heat via lattice vibrations. However, incident photons with energy less than E_{gap} cannot be absorbed and will be transmitted through the device. These lost photons are termed as sub-band-gap photons. The plasmonic photocatalysts aims to effectively utilize of sub-bandgap visible range photons, known as 'visible light photocatalysis'.[56]

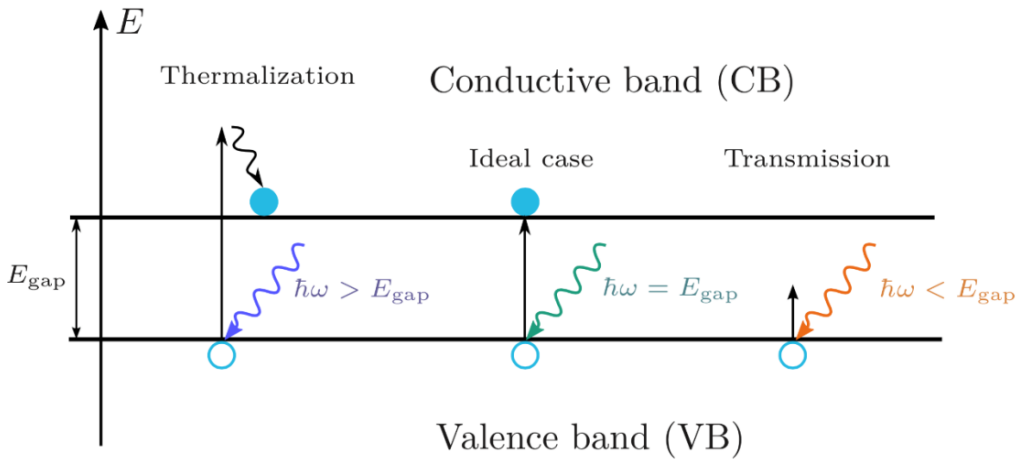

Figure 2- 6 Schematic diagram of the spectral losses of solar cells associated with a discrete band gap energy E_{gap}. This figure is reprinted from ref-18.

Plasmonic nanoparticles can efficiently absorb solar energy via localized surface plasmon resonance and convert it to energetic electrons/holes in the neighboring of semiconductor. Plasmonic effects can improve the photocatalytic performance of semiconductor via several mechanisms, including improve harnessing of visible light, prolong the lifetime of the charge carriers, improve activation of electron-hole pairs and enhance the redox reaction potential (figure 2-7).[57] At the same time, the generation of excess of electrons and holes can increase the rate of redox reaction.

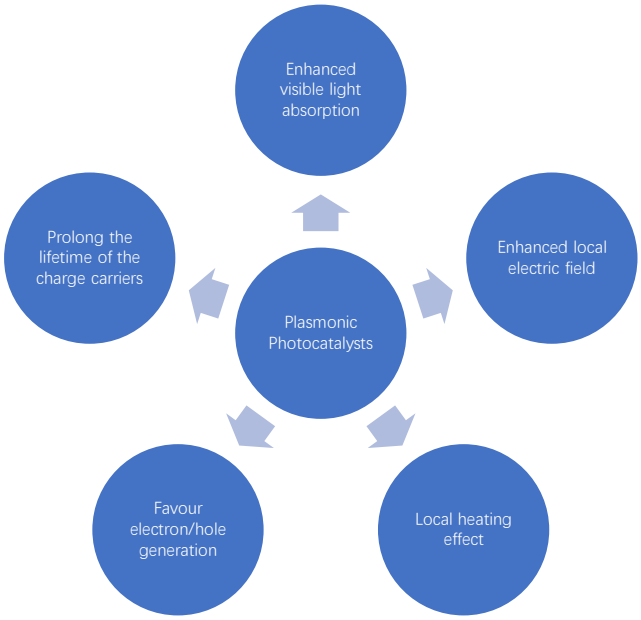

Figure 2- 7 Schematic diagram of plasmonic effect for the photocatalyst enhancement.

Noble metals (such as Au, Ag, Pt) in the form of nanostructures or nanoparticles are good candidates for high absorption of visible light. The unique characteristics of the LSPR effect in noble metal can enhance the photons within the visible solar spectrum. Intense studies have revealed the physics of LSPR of plasmonic nanoparticles.[58,59] However, the mechanisms of energy transfer between plasmonic nanoparticles and semiconductors are not very clear. Three energy transfer processes have been proposed so far, including: 1. plasmon-induced hot electron injection, 2. plasmon-induced resonance energy transfer and 3. plasmon-induced radiative energy transfer.

2.4.1 Plasmon-induced hot electron injection

To date, the key role of LSPR related energy transfer for photocatalytic performance has been well acknowledged. The term hot electron here refers to electrons that are not in thermodynamic equilibrium with the atoms in a noble metal nanomaterial. The hot electrons are generated during the non-radiative relaxation process mainly via electron-electron scattering, which results in intra- and inter-band excitation of conduction electrons. In the case of plasmonic photocatalysts, a Schottky junction can be created between a noble metal and a semiconductor due to retard of the recombination rate of electrons and holes.[60] The energies of hot electrons in Au plasmonic nanoparticles are reported between 1 eV and 4eV.[61] Such energetic hot electrons may migrate to the neighboring semiconductor if their energies are higher than the Schottky barrier (SB) at the interface. In addition, hot electrons with energies lower than the Schottky barriers may also be injected into the semiconductor by tunneling effect.[62]

The Atwater and Louie groups also studied the generation of hot carriers through the decay of surface plasmon polaritons (SPPs) on metal-dielectric interfaces.[63,64] Their theoretical studies show that Au is beneficial for the generation of hot holes rather than hot electrons due to the special electronic structures. Their calculation also indicates that the energies of some modes of SPPs were large enough to excite the d to s inter-band transitions. The first experimental evidence of plasmon induced hot electrons migration from Au to TiO_2 was reported by Zhao *et al*. [65] When the excitation matches the LSPR absorption of Au plasmonic nanoparticles, an increase in the anodic photocurrent was observed for a TiO_2 film electrode containing plasmonic components. Furube *et al.* [66] realized direct observation of the injection of hot electrons into the conduction band of TiO_2,[67] any possible direct electron transfer from Au to TiO_2 was detected by femtosecond-resolved IR probing. The IR absorption signal demonstrated that the ultrafast hot electron transfer from Au nanodots to TiO_2 was determined to be within 240 fs.

2.4.2 Plasmon-induced resonance energy transfer

There are two terms refer to the plasmon-induced energy transfer: energy transfer through near-field enhancement and energy transfer through dipole-dipole coupling.[68] It is demonstrated that the plasmonic dipole can induce near-field enhancement. Electromagnetic simulations using finite-difference time-domain (FDTD) or discrete dipole approximation (DDA) method indicated that the intensity of the plasmon induced near-field can be enhanced tens to thousands of times compared to the incident light.[69,70] If the LSPR band overlap with the inter-band or other optical transitions in the intimate semiconductor, the full enhancement of light absorption can be estimated using the equation:

$$FE=\frac{\int_v dz \int dx\, dy\, |E(x,y,z)|^2}{\int_v dz \int dx\, dy\, |E_0|^2} \qquad \text{(Equ 2-11)}$$

Where the integrating volume V refers to the volume in the semiconductor covered by the near field. E(x,y,x) represents the value at near-field at the point of (x,y,z). E_0 refers to the electric field of incident light. The energy transfer via near field enhancement have been experimentally demonstrated in a number of researches.[71,72]

Cushing *et al*. proposed the term plasmonic resonance energy transfer in 2012.[73] In this case, electron/hole pairs were excited by plasmonic resonance in the semiconductors due to the coupling of plasmonic dipole to the electron-hole pair dipole. Based on the plasmon-induced resonance energy transfer mechanism, three key factors can influence the energy transfer efficiency: the overlap between LSPR absorption band and the optical transitions in the semiconductor, the intensity of the enhanced near field, and the volume of the enhanced near-field that can cover. The LSPR of plasmonic nanoparticles can also decay radiatively. As a result, the emitted high energy photons may be absorbed by the neighboring semiconductor and generate electron/hole pairs. Kumar *et al*. discovered evidence of this energy transfer experimentally.[74]

The special energy transfer mechanisms from plasmonic nanomaterials to semiconductor is a prominent characteristic of plasmonic photocatalysts. In most cases, the plasmon-induced energy transfer mechanism is relatively weak compared to plasmon-induced hot electron injection. In general, plasmon-induced hot electron injection and plasmon-induced resonance energy transfer are two major effects, while plasmon-induced radiative energy transfer is negligible. The energy transfer efficiency is very sensitive to the structure of plasmonic photocatalytic composite. Both the generation and injection of hot electrons are influenced by the specific structure. On the other hand, the geometry of plasmonic nanostructure will influence the LSPR absorption band and will thus influence the overlap between the LSPR and optical transitions in semiconductors. In addition, proper band alignment and electronic coupling between the metal and semiconductors are significant for the hot electron injection process. Francesca Pincella *et al*. demonstrated a bottom-up approach to fabricating a visible light-driven titania photocatalyst device, which bears an embedded 2D array of gold nanoparticles as a near-field light generating layer. The visible light activity of their device was tested by using photocatalytic degradation of methylene blue (MB) by 700 nm visible light excitation. Compared with the benchmark sample, the device showed 1.7 times higher photocatalytic activity than titania under UV irradiation.[75]

In recent years, a burgeoning concept, plasmon-enhanced upconversion photocatalyst system was proposed. To explore a better energy transfer pathway between the plasmonic, upconversion and photocatalysts, which may ultimately realize the industrialization of photocatalytic technology. D. Ma *et al*. designed Core@Shell microspheres based on lanthanide-doped $NaYF_4$, TiO_2 and Au photocatalytic system, which achieved enhanced broadband photocatalytic activity.[76] This is an early work towards the concepts of plasmonic and upconversion to realize broadband photocatalysts. The role of $NaYF_4$@TiO_2@Au microspheres is to capture photons over a wide wavelength range from UV, visible to

NIR, significantly superior to the benchmark photocatalyst of P25 TiO_2. However, as stated in the section of rare-earth based upconverison nanoparticles, the upconversion efficiencies are still very limited so far. Therefore, it is desired to search for an alternative upconversion candidate. In 2012, J-H. Kim reported the first instance of aqueous-phase photosensitization of semiconductor photocatalysts (WO_3 loaded with Pt) via triplet-triplet annihilation upconversion (TTA-UC) of sub-bandgap photons.[77] In 2016, H. Kim *et al*. demonstrated a plasmon-enhanced sub-bandgap photocatalysis via Triplet-Triplet annihilation upconversion (TTA-UC) for volatile organic compound degradation. This work is the first reported photocatalytic decomposition via TTA-UC.[78] The photocatalytic efficiency was amplified by the broadband surface plasmon resonance of AgNP-SiO_2 particles incorporated into the TTA-UC films. Although this is just a proof-of-concept stage research, it validated the low-energy, low intensity indoor light to clean contaminated air assisted by TTA-UPNPs.

In summary, research on plasmon-enhanced upconversion has driven by great enthusiasm, with a surging of studies on conjugation of UCNPs and plasmonic nanostructures. Theoretical and experimental studies are gradually revealing the fundamental principle for plasmon-enhanced upconversion. However, various underlying mechanisms still needed to be explored in detail. Recent explorations in plasmon-enhanced upconversion for photocatalysis enhancement have demonstrated great potential. Inspired by these previous work, further explorations based on these studies will be conducted in this thesis.

Reference

1. Bloembergen, N. Solid state infrared quantum counters. *Physical Review Letters* **2**, 84 (1959).
2. Auzel, F. Upconversion and anti-stokes processes with f and d ions in solids. *Chemical reviews* **104**, 139-174 (2004).
3. Zhang, F. *et al.* Uniform nanostructured arrays of sodium rare-earth fluorides for highly efficient multicolor upconversion luminescence. *Angewandte Chemie International Edition* **46**, 7976-7979 (2007).
4. Wei, Y., Lu, F., Zhang, X. & Chen, D. Synthesis and characterization of efficient near-infrared upconversion Yb and Tm codoped NaYF4 nanocrystal reporter. *Journal of alloys and compounds* **427**, 333-340 (2007).
5. Yin, Y. & Alivisatos, A. P. Colloidal nanocrystal synthesis and the organic–inorganic interface. *Nature* **437**, 664 (2004).
6. Mai, H.-X. et al. High-quality sodium rare-earth fluoride nanocrystals: controlled synthesis and optical properties. *Journal of the American Chemical Society* 128, 6426-6436 (2006).
7. Mader, H. S., Kele, P., Saleh, S. M. & Wolfbeis, O. S. Upconverting luminescent nanoparticles for use in bioconjugation and bioimaging. *Current opinion in chemical biology* 14, 582-596 (2010).
8. Chen, G., Qiu, H., Prasad, P. N. & Chen, X. Upconversion Nanoparticles: Design, Nanochemistry, and Applications in Theranostics. *Chemical Reviews* 114, 5161-5214, doi:10.1021/cr400425h (2014).
9. Chan, E. M. et al. Combinatorial discovery of lanthanide-doped nanocrystals with spectrally pure upconverted emission. *Nano letters* 12, 3839-3845 (2012).
10. Sun, L.-D., Dong, H., Zhang, P.-Z. & Yan, C.-H. Upconversion of rare earth nanomaterials. *Annual review of physical chemistry* **66**, 619-642 (2015).

11. F.Zhang, Nanostructure Science and Technology, *Spriger*, (2014)

12. Wang, R., Li, X., Zhou, L. & Zhang, F. Epitaxial Seeded Growth of Rare-Earth Nanocrystals with Efficient 800 nm Near-Infrared to 1525 nm Short-Wavelength Infrared Downconversion Photoluminescence for In Vivo Bioimaging. *Angewandte Chemie International Edition* 53, 12086-12090 (2014).

13. Sun, L.-D., Dong, H., Zhang, P.-Z. & Yan, C.-H. Upconversion of rare earth nanomaterials. *Annual review of physical chemistry* 66, 619-642 (2015).

14. Pollnau, M., Gamelin, D. R., Lüthi, S., Güdel, H. & Hehlen, M. Power dependence of upconversion luminescence in lanthanide and transition-metal-ion systems. *Physical Review B* 61, 3337 (2000).

15. Suyver, J., Grimm, J., Krämer, K. & Güdel, H.-U. Highly efficient near-infrared to visible up-conversion process in NaYF4: Er3+, Yb3+. *Journal of Luminescence* 114, 53-59 (2005).

16. Haase, M. & Schäfer, H. Upconverting nanoparticles. *Angewandte Chemie International Edition* 50, 5808-5829 (2011).

17. Wang, G., Peng, Q. & Li, Y. Lanthanide-doped nanocrystals: synthesis, optical-magnetic properties, and applications. *Accounts of chemical research* 44, 322-332 (2011).

18. S.Fischer, Freiburg im Breisgau, Germany, 2014

19. Würth, C., Grabolle, M., Pauli, J., Spieles, M. & Resch-Genger, U. Relative and absolute determination of fluorescence quantum yields of transparent samples. *Nature protocols* 8, 1535 (2013).

20. Boyer, J.-C. & van Veggel, F. C. J. M. Absolute quantum yield measurements of colloidal NaYF4: Er3+, Yb3+ upconverting nanoparticles. *Nanoscale* 2, 1417-1419, doi:10.1039/C0NR00253D (2010).

21. Ostrowski, A. D. et al. Controlled synthesis and single-particle imaging of bright, sub-10 nm lanthanide-doped upconverting nanocrystals. *ACS nano* 6, 2686-2692 (2012).

22. Chen, G., Ohulchanskyy, T. Y., Kachynski, A., Ågren, H. & Prasad, P. N. Intense visible and near-infrared upconversion photoluminescence in colloidal LiYF4: Er3+ nanocrystals under excitation at 1490 nm. *ACS nano* 5, 4981-4986 (2011).

23. Wang, J. et al. Surface plasmon resonance sensors on raman and fluorescence spectroscopy. *Sensors* 17, 2719 (2017).

24. Atwater, H. A. & Polman, A. Plasmonics for improved photovoltaic devices. *Nature Materials* 9, 205, doi:10.1038/nmat2629 (2010).

25. Wang, X. et al. Excitation and propagation of surface plasmon polaritons on a non-structured surface with a permittivity gradient. *Light: Science &Amp; Applications* 5, e16179, doi:10.1038/lsa.2016.179 (2016).

26. Wu, D. M., García-Etxarri, A., Salleo, A. & Dionne, J. A. Plasmon-enhanced upconversion. *The journal of physical chemistry letters* 5, 4020-4031 (2014).

27. Lakowicz, J. R. Radiative decay engineering 5: metal-enhanced fluorescence and plasmon emission. *Analytical biochemistry* 337, 171-194 (2005).

28. Esteban, R., Laroche, M. & Greffet, J.-J. Influence of metallic nanoparticles on upconversion processes. *Journal of Applied Physics* 105, 033107 (2009).

29 Klimov, V. V., Pavlov, A. A., Guzatov, D. V., Zabkov, I. V. & Savinov, V. D. Radiative decay of a quantum emitter placed near a metal-dielectric lamellar nanostructure: Fundamental constraints. *Physical Review A* 93, 033831, doi:10.1103/PhysRevA.93.033831 (2016).

30. Thomas, S. et al. Size-dependent surface plasmon resonance in silver silica nanocomposites. *Nanotechnology* 19, 075710 (2008).

31. Xu, G., Tazawa, M., Jin, P., Nakao, S. & Yoshimura, K. Wavelength tuning of surface plasmon resonance using dielectric layers on silver island films. *Applied Physics Letters* 82, 3811-3813 (2003).

32. Liu, L., Guo, Z., Xu, L., Xu, R. & Lu, X. Facile purification of colloidal NIR-responsive gold nanorods using ions assisted self-assembly. *Nanoscale research letters* 6, 143 (2011).

33. Huang, X., Jain, P. K., El-Sayed, I. H. & El-Sayed, M. A. Plasmonic photothermal therapy (PPTT) using gold nanoparticles. *Lasers in medical science* 23, 217 (2008).

34. Lu, D. et al. Plasmon enhancement mechanism for the upconversion processes in NaYF4: Yb3+, Er3+ nanoparticles: Maxwell versus Förster. *ACS nano* 8, 7780-7792 (2014).

35. Suyver, J. et al. Novel materials doped with trivalent lanthanides and transition metal ions showing near-infrared to visible photon upconversion. *Optical Materials* 27, 1111-1130 (2005).

36. Zhang, W., Ding, F. & Chou, S. Y. Large Enhancement of Upconversion Luminescence of NaYF4: Yb3+/Er3+ Nanocrystal by 3D Plasmonic Nano-Antennas. *Advanced Materials* **24**, OP236-OP241 (2012).

37. Paudel, H. P. *et al.* Enhancement of near-infrared-to-visible upconversion luminescence using engineered plasmonic gold surfaces. *The Journal of Physical Chemistry C* **115**, 19028-19036 (2011).

38. Bayat, K. *et al.* Design, fabrication, and characterization of a plasmonic upconversion enhancer and its prospects for photovoltaics. *Journal of Photonics for Energy* **3**, 035598 (2013).

39. Saboktakin, M. *et al.* Plasmonic enhancement of nanophosphor upconversion luminescence in Au nanohole arrays. *ACS nano* **7**, 7186-7192 (2013).

40. Saboktakin, M. *et al.* Metal-enhanced upconversion luminescence tunable through metal nanoparticle–nanophosphor separation. *ACS nano* **6**, 8758-8766 (2012).

41. Schietinger, S., Aichele, T., Wang, H.-Q., Nann, T. & Benson, O. Plasmon-enhanced upconversion in single NaYF4: Yb3+/Er3+ codoped nanocrystals. *Nano letters* **10**, 134-138 (2009).

42. Kannan, P. *et al.* Enhanced emission of NaYF4: Yb, Er/Tm nanoparticles by selective growth of Au and Ag nanoshells. *RSC Advances* **3**, 7718-7721 (2013).

43. Feng, W., Sun, L.-D. & Yan, C.-H. Ag nanowires enhanced upconversion emission of NaYF4: Yb, Er nanocrystalsvia a direct assembly method. *Chemical Communications*, 4393-4395 (2009).

44. Deng, W. *et al.* Upconversion in NaYF4: Yb, Er nanoparticles amplified by metal nanostructures. *Nanotechnology* **22**, 325604 (2011).

45. Priyam, A., Idris, N. M. & Zhang, Y. Gold nanoshell coated NaYF4 nanoparticles for simultaneously enhanced upconversion fluorescence and darkfield imaging. *Journal of Materials Chemistry* **22**, 960-965 (2012).

46. Lantigua, C. *et al.* Engineering upconversion emission spectra using plasmonic nanocavities. *Optics letters* **39**, 3710-3713 (2014).

47. Yuan, P. *et al.* Plasmon enhanced upconversion luminescence of NaYF4: Yb, Er@ SiO 2@ Ag core–shell nanocomposites for cell imaging. *Nanoscale* **4**, 5132-5137 (2012).

48. Priyam, A., Idris, N. M. & Zhang, Y. Gold nanoshell coated NaYF4 nanoparticles for simultaneously enhanced upconversion fluorescence and darkfield imaging. *Journal of Materials Chemistry* **22**, 960-965, doi:10.1039/C1JM14040J (2012).

49. Liu, N., Qin, W., Qin, G., Jiang, T. & Zhao, D. Highly plasmon-enhanced upconversion emissions from Au@β-NaYF4:Yb,Tm hybrid nanostructures. *Chemical Communications* **47**, 7671-7673, doi:10.1039/C1CC11179E (2011).

50. Rurack, K. & Martínez-Máñez, R. The supramolecular chemistry of organic-inorganic hybrid materials. (John Wiley & Sons, 2010).

51. Amendola, V., Bakr, O. M. & Stellacci, F. A study of the surface plasmon resonance of silver nanoparticles by the discrete dipole approximation method: effect of shape, size, structure, and assembly. *Plasmonics* 5, 85-97 (2010).

52. Zhang, W., Ding, F. & Chou, S. Y. Large Enhancement of Upconversion Luminescence of NaYF4:Yb3+/Er3+ Nanocrystal by 3D Plasmonic Nano-Antennas. *Advanced Materials* 24, OP236-OP241, doi:10.1002/adma.201200220 (2012).

53. Greybush, N. J. et al. Plasmon-enhanced upconversion luminescence in single nanophosphor–nanorod heterodimers formed through template-assisted self-assembly. *ACS nano* 8, 9482-9491 (2014).

54. Sun, Q.-C. et al. Plasmon-enhanced energy transfer for improved upconversion of infrared radiation in doped-lanthanide nanocrystals. *Nano letters* 14, 101-106 (2013).

55. Vogl, á., Hjalmarson, H. P. & Dow, J. D. A semi-empirical tight-binding theory of the electronic structure of semiconductors. *Journal of Physics and Chemistry of Solids* 44, 365-378 (1983).

56. Leong, K. H. et al. Mechanistic insights into plasmonic photocatalysts in utilizing visible light. *Beilstein Journal of Nanotechnology* 9, 628-648, doi:10.3762/bjnano.9.59 (2018).

57. Wang, Z. et al. Progress on extending the light absorption spectra of photocatalysts. *Physical Chemistry Chemical Physics* 16, 2758-2774, doi:10.1039/C3CP53817F (2014).

58. Fan, X., Zheng, W. & Singh, D. J. Light scattering and surface plasmons on small spherical particles. *Light: Science & Applications* 3, e179 (2014).

59. Kelly, K. L., Coronado, E., Zhao, L. L. & Schatz, G. C. The Optical Properties of Metal Nanoparticles: The Influence of Size, Shape, and Dielectric Environment. *The Journal of Physical Chemistry B* 107, 668-677, doi:10.1021/jp026731y (2003).

60. Wang, X. et al. A New Insight of the Photothermal Effect on the Highly Efficient Visible-Light-Driven Photocatalytic Performance of Novel-Designed TiO2 Rambutan-Like Microspheres Decorated by Au Nanorods. *Particle & Particle Systems Characterization* 33, 140-149 (2016).

61. Linic, S., Christopher, P. & Ingram, D. B. Plasmonic-metal nanostructures for efficient conversion of solar to chemical energy. *Nature materials* 10, 911 (2011).

62. Mubeen, S., Hernandez-Sosa, G., Moses, D., Lee, J. & Moskovits, M. Plasmonic photosensitization of a wide band gap semiconductor: converting plasmons to charge carriers. *Nano letters* 11, 5548-5552 (2011).

63. Sundararaman, R., Narang, P., Jermyn, A. S., Goddard III, W. A. & Atwater, H. A. Theoretical predictions for hot-carrier generation from surface plasmon decay. *Nature communications* 5, 5788 (2014).

64. Bernardi, M., Mustafa, J., Neaton, J. B. & Louie, S. G. Theory and computation of hot carriers generated by surface plasmon polaritons in noble metals. *Nature communications* 6, 7044 (2015).

65. Zhao, G., Kozuka, H. & Yoko, T. Sol—gel preparation and photoelectrochemical properties of TiO2 films containing Au and Ag metal particles. *Thin Solid Films* 277, 147-154 (1996).

66. Furube, A., Du, L., Hara, K., Katoh, R. & Tachiya, M. Ultrafast plasmon-induced electron transfer from gold nanodots into TiO2 nanoparticles. *Journal of the American Chemical Society* 129, 14852-14853 (2007).

67. Asbury, J. B., Hao, E., Wang, Y., Ghosh, H. N. & Lian, T. Ultrafast Electron Transfer Dynamics from Molecular Adsorbates to Semiconductor Nanocrystalline Thin Films. *The Journal of Physical Chemistry B* 105, 4545-4557, doi:10.1021/jp003485m (2001).

68. Ma, X.-C., Dai, Y., Yu, L. & Huang, B.-B. Energy transfer in plasmonic photocatalytic composites. *Light: Science &Amp; Applications* 5, e16017, doi:10.1038/lsa.2016.17 (2016).

69. Kelly, K. L., Coronado, E., Zhao, L. L. & Schatz, G. C. The Optical Properties of Metal Nanoparticles: The Influence of Size, Shape, and Dielectric Environment. *The Journal of Physical Chemistry B* 107, 668-677, doi:10.1021/jp026731y (2003).

70. Ma, X. et al. Electron–hole pair generation of the visible-light plasmonic photocatalyst Ag@ AgCl: enhanced optical transitions involving midgap defect states of AgCl. *The Journal of Physical Chemistry C* 118, 12133-12140 (2014).

71. Thomann, I. et al. Plasmon enhanced solar-to-fuel energy conversion. *Nano letters* 11, 3440-3446 (2011).

72. Torimoto, T. et al. Plasmon-enhanced photocatalytic activity of cadmium sulfide nanoparticle immobilized on silica-coated gold particles. *The journal of physical chemistry letters* 2, 2057-2062 (2011).

73. Cushing, S. K. et al. Photocatalytic activity enhanced by plasmonic resonant energy transfer from metal to semiconductor. *Journal of the American Chemical Society* 134, 15033-15041 (2012).

74. Kumar, M. K. et al. Field effects in plasmonic photocatalyst by precise SiO2 thickness control using atomic layer deposition. *Acs Catalysis* 1, 300-308 (2011).

75. Pincella, F., Isozaki, K. & Miki, K. A visible light-driven plasmonic photocatalyst. *Light: Science & Applications* 3, e133 (2014).

76. Xu, Z. *et al.* Harvesting lost photons: plasmon and upconversion enhanced broadband photocatalytic activity in core@ shell microspheres based on lanthanide-doped NaYF4, TiO2, and Au. *Advanced Functional Materials* **25**, 2950-2960 (2015).

77. Kim, J.-H. & Kim, J.-H. Encapsulated triplet–triplet annihilation-based upconversion in the aqueous phase for sub-band-gap semiconductor photocatalysis. *Journal of the American Chemical Society* 134, 17478-17481 (2012).

78 Kim, H.-i. et al. Plasmon-Enhanced Sub-Bandgap Photocatalysis via Triplet–Triplet Annihilation Upconversion for Volatile Organic Compound Degradation. *Environmental Science & Technology* 50, 11184-11192, doi:10.1021/acs.est.6b02729 (2016).

Chapter 3 Tuning the upconversion photoluminescence lifetimes of $NaYF_4:Yb^{3+}$, Er^{3+} through lanthanide Gd^{3+} doping

3.1 Introduction

This chapter studies the properties of rare-earth doped upconversion nanoparticles $NaYF_4:Yb^{3+}$, Er^{3+}, including their hydrothermal synthesis, geometrical properties, upconversion efficiency and lifetimes modification according to a Gd^{3+} doping strategy. Based on the upconversion efficiency measurements, the low upconversion efficiency of $NaYF_4:Yb^{3+}$, Er^{3+} implies their drawbacks to be applied in solar energy fields. However, the availability to fine-tune the lifetimes of $NaYF_4:Yb^{3+}$, Er^{3+} suggests their great potential to be utilized in the biotechnology and life science. The major work of this chapter has been published in Qin, H. *et al.* Enhancement of the upconversion photoluminescence of hexagonal phase $NaYF_4:Yb^{3+}$, Er^{3+} nanoparticles by mesoporous gold films. Physical Chemistry Chemical Physics **19**, 19159-19167, doi:10.1039/C7CP01959A (2017).

Optical multiplexing gains significant attention in biotechnology and life science due to the capability of identifying and quantifying multiple biomolecular species.[1] To realize efficient multiplexing, one of the great challenges is the exploration of optical markers possessing a matrix of optical codes, which could be identified with minimal time, high sensitivity and accuracy. However, conventional fluorescence materials, including quantum dots and organic dyes, only exhibit lifetimes in the order of nanoseconds,[2] and are simply too short for the temporal identification of fluorescence interference from scattered excitation photons. In contrast to these short-lived fluorescence counterparts, lanthanide ions doped upconversion nanoparticles (UCNPs) demonstrate distinct photoluminescence lifetimes from microseconds to even milliseconds.[3,4] Upconversion photoluminescence nanoparticles, not only can

realize frequency conversion via converting two (or more) low-energy photons into one high-energy photon, but also exhibit unique optical properties such as high resistance to optical blinking, sharp and multiple luminescence peaks, as well as high photostability.[5] All these advantages make UCNPs a great candidate for multiplexing, allowing the creation of extra coding dimensions. Current research has already suggested that Ln-doped fluorides (i.e., $NaYF_4$:Yb^{3+} 20%, Er^{3+} 2%) are the most promising and efficient nanomaterial to achieve desirable UCPL.[6,7,8] However, poor upconversion efficiencies of UCNPs remains to be one of the most critical limitation for a range of applications.[9,10] Further studies of the enhancement of upconversion quantum yield (UCQY) of UCNPs are needed to fulfil their full potential for practical applications. Recent advances demonstrated the availability of systematically tuning various properties of UCNPs, including phase, morphology, and quantum yield through designing lanthanide doping strategy and novel nanostructure, such as core-shell structure[11], nanoarrays structure[12], etc. Liu realized simultaneous phase and size control of UCNPs with strong UCPL by additional doping of Gd^{3+} ions.[13] Despite these progresses have been achieved, it remains a challenge to precisely tune the UCPL lifetimes of $NaYF_4$ nanocrystals, with high efficiency UCPL to overcome the limitation in emission selectivity for the multiplexed applications.

In this chapter, we developed a facile Gd^{3+} doping strategy in a hydrothermal process to synthesize a set of upconversion nanomaterials with distinct luminescent properties. The dominant role of energy transfer upconversion (ETU) process in Sensitizer–Activator-coupled UCNPs system was identified by accurate lifetime measurement (TCSPC). Accordingly, we observed that the lanthanide Gd^{3+} ion doping approach leads to a clear prolonged lifetime of photoluminescence, and the lifetimes of both green emission (at 540 nm) and red emission (at 656 nm) exhibit as a function of the internal upconversion quantum yield (iUCQY). In addition, X-ray powder diffraction (XRD), field emission scanning electron microscopy (FE-

SEM) were used to characterize the UCNPs. Our results indicate that tunable UCPL lifetimes have remarkable potential for optical multiplexing applications.

3.2 Experimental methods

3.2.1 Chemicals

All reagents were of analytical grade. Yttrium(III) nitrate hexahydrate ($Y(NO_3)_3 \cdot 6H_2O$, Sigma-Aldrich, ≥99.9%), ytterbium(III) nitrate pentahydrate ($Yb(NO_3)_3 \cdot 5H_2O$, Sigma-Aldrich, ≥99.9%), erbium(III) nitrate pentahydrate ($Er(NO_3)_3 \cdot 5H_2O$, Sigma-Aldrich, ≥99.9%), gadolinium(III) chloride hexahydrate ($GdCl_3 \cdot 6H_2O$, Sigma-Aldrich, ≥99.9%), gadolinium(III) oxide (Gd2O3, Sigma-Aldrich, ≥99.99%), sodium fluoride (NaF, Alfa Aesar, ≥99.99%), oleic acid (OA, Fisher Scientific, ≥97%), ethanol absolute (VWR International, ≥99.7%), and sodium hydroxide (NaOH, VWR International, 40% W/V) were used as supplied.

3.2.2 Synthesis of $NaYF_4$:$Yb3^+$, Er^{3+} co-doped Gd^{3+} Upconversion Nanoparticles

In a typical synthesis process, the rare earth (RE) nitrate $RE(NO_3)_3$ (Re = Y^{3+}, Yb^{3+}, and Er^{3+}) and gadolinium chloride $GdCl_3$ were dissolved in DI water to obtain the aqueous solutions, respectively. Then, a 29.28 mL solution containing 1.952 mmol RE nitrate was mixed with 20 mL ethanol and 25 mL oleic acid under vigorous stirring. The ytterbium nitrate and erbium nitrate solutions were added to the resulting solutions according the calculated quantities. The molar ratio of Yb^{3+}: Er^{3+} was controlled to be 20 mol% and 2 mol%, respectively. And the molar ratio of the Gd^{3+} ion dopant was controlled to be 30 mol%, 50 mol% and 70 mol% respectively. The gadolinium chloride aqueous solution was added to the resulting mixture according the calculated quantities. Then, 1 mL NaOH solution and 0.85 g NaF powder were slowly added into the aqueous

solution under vigorous stirring. After another vigorous agitation for 30 minutes, the mixture was transferred into a 100 mL Teflon-lined autoclave, and then heated at 200 ℃ for 20 hours. The resulting white precipitates were obtained by centrifugation, washed with DI water 5 times to remove the residues. The final powder samples were collected and dried at 80 ℃ for 24 hours in a vacuum furnace.

3.2.3 X-Ray Diffractometer characterization

The crystal phases of the products were identified by X-Ray Diffractometer (XRD) with 2θ range from 10° to 70° at a scanning rate of 4° per minute, with Cu Ka irradiation (k=1.5406 Å), step size 0.0167°, scanning angle 20°-70°. The 980 nm CW laser (Beijing Hi-Tech Optoelectronic Co., Ltd.) was used as the excitation source with the power being set at 20 $W \cdot cm^{-2}$. The upconverting fluorescence spectra were recorded on DCS200PC Photon Counting (Beijing Zolix Instruments Co., Ltd) with single-photon sensitivity through an Omni-λ500 monochromator (Beijing Zolix Instruments Co., Ltd).

3.2.4 Photoluminescence Lifetime measurement

Time-correlated single-photon counting (TCSPC), which is considered as the most sensitive digital technique for determining photoluminescence lifetime to date, was used to obtain a dynamic picture of the upconversion photoluminescence of the as-prepared samples (Figure 3-1(a)).[14] With well-defined Poisson statistics, TCSPC is a method based on the detection of the arrival time of individual photon after optical excitation of a sample. Importantly, this mechanism allows only one photon can be counted at any one time and the measured lifetimes are not affected by changes in source intensity. It is worth to mention that the lifetimes of UCNPs in general cases are independent of excitation power density in the low power regime ($< 100\ Wcm^{-2}$).[15] We

precisely modulated the pulse duration of the 980 nm pulsed laser to statistically characterize the time dependent photoluminescence emission profiles of the as-synthesized UCNPs by repeating the excitation-emission process to 10000 counts.

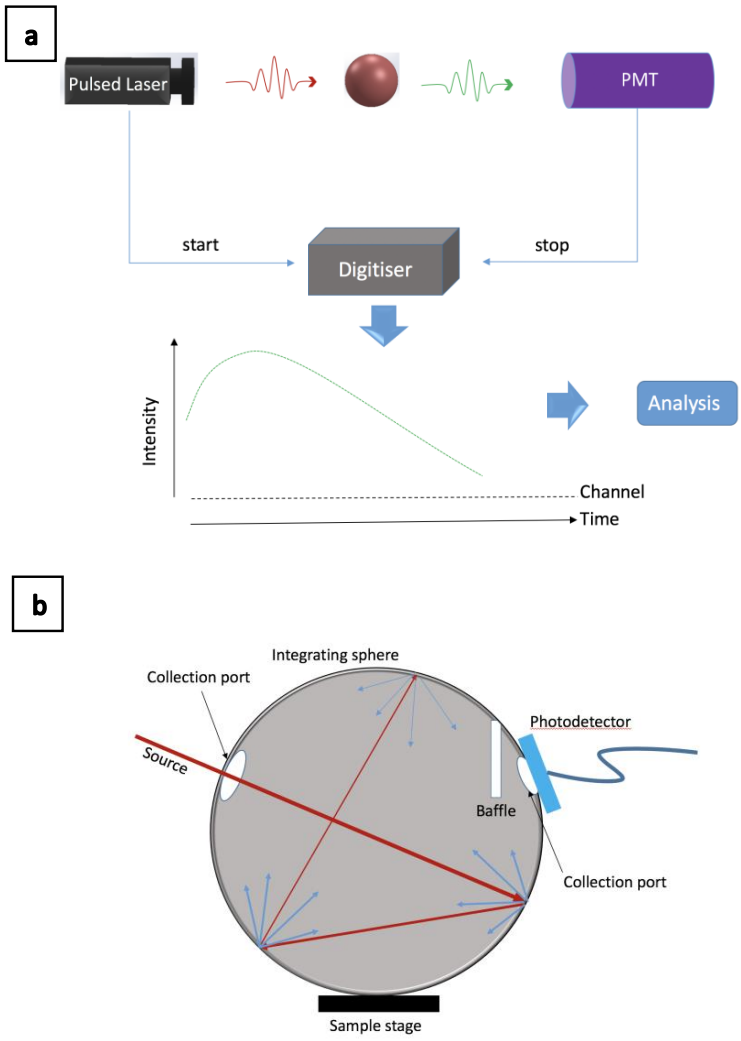

Figure 3- 1 (a) Schematic diagram for TCSPC setup. (b) Schematic diagram of the integrating sphere setup to measure the quantum yield values.

3.2.5 Absolute quantum yield measurement

The absolute quantum yields were measured with an integrating sphere setup (Figure 3-1b). To make the measured results comparable, all external-influence factors were controlled in the same condition. This setup consisted of eight major components: integrating sphere, sample stage, 980 nm diode laser, focusing lens, baffle, collection port, optical fiber, and spectrometer. During the experiment, the resulting powder samples were excited under 980 nm laser at an input intensity of 4.13 W cm^{-2}. The 980 nm laser was placed inside the sample chamber and directed towards the specimen through a focusing lens with a 15 cm focal length. Finally, the fluorescence emission output from the sphere was obtained by a liquid light guide and then transmitted to the detector. The efficiency of UCNPs is typically defined by internal upconversion quantum yield (iUCQY), which is calculated using the following equation:

$$\boldsymbol{iUCQY} = \frac{\boldsymbol{number\ of\ photons\ emitted}}{\boldsymbol{number\ of\ photons\ absorbed}} \qquad \text{(Equ 3-1)}$$

The upconverting fluorescence spectra were recorded on DCS200PC Photon Counting (Zolix Instruments Co., Ltd) with single-photon sensitivity through an Omni-λ500 monochromator (Zolix Instruments Co., Ltd).

3.3 Results and discussion

3.3.1 Morphology and Structure of the Nanocrystals

All samples were first examined by X-ray powder diffraction. Figure 3-2 shows the XRD patterns of $NaYF_4$:Yb^{3+}, Er^{3+} materials doped with 0% - 70% Gd^{3+} ions synthesized at 200℃ for 20 hours. The diffraction patterns show evidence of the co-existence of cubic phase (JCPDS File No. 772042) and hexagonal phase $NaYF_4$ (JCPDS File No. 16-0334) without Gd^{3+} doping prepared in this synthesis condition. Notably, the XRD patterns demonstrate the formation of hexagonal phase

$NaYF_4$:Yb^{3+}, Er^{3+} when doping additional 30% Gd^{3+} according to standard hexagonal XRD spectra of $NaYF_4$. This suggests extra dopant Gd^{3+} ions can effectively induce a cubic to hexagonal phase transition under this synthesize condition. No extra diffraction peaks appeared with further increase of the Gd^{3+} concentration from 30 mol% to 70 mol%, which implies the formation of a homogeneous Y-Gd solid solution. Since the Y^{3+} ions were substituted by larger Gd^{3+} ions in the host lattice, the diffraction peaks shifted to lower diffraction angles with the increasing of Gd^{3+} ions concentration.

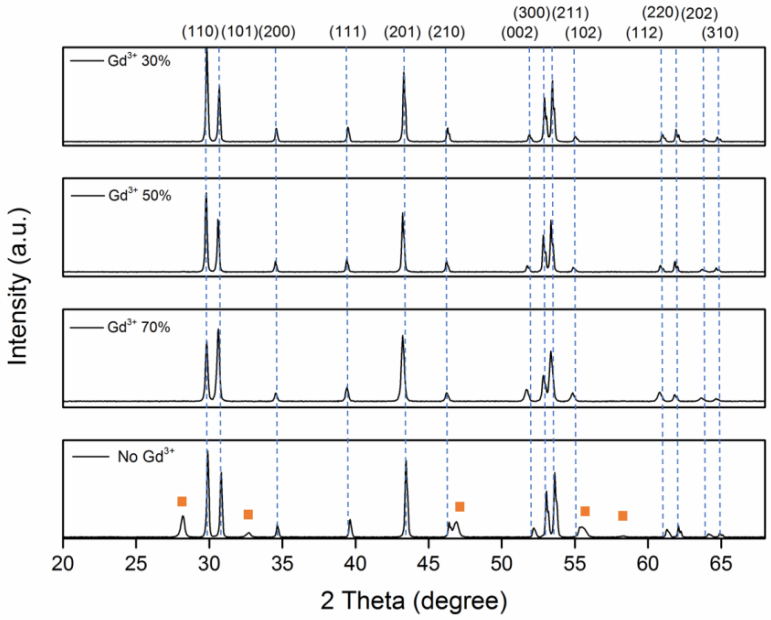

Figure 3- 2 XRD patterns of $NaYF_4$ doped with 0 mol% - 70 mol% Gd^{3+} ions and synthesized by a hydrothermal method heated under 200℃ for 20 hours. The orange squares indicate the characteristic peaks of cubic phase.

To study the crystallite size and phase of $NaYF_4$:Yb^{3+}, Er^{3+} doped with different concentrations of Gd^{3+} ions, all the samples were synthesized under a same heating condition and characterized by scanning

electron microscopy (SEM). A brief summary of the synthetic parameters of $NaYF_4:Yb^{3+}$, Er^{3+}, Gd^{3+} materials are listed in Table 3-1.

Table 3- 1 Reaction parameters and conditions for sample of $NaYF_4/Yb^{3+},Er^{3+}$ doped with different concentration of Gd^{3+}.

Samples	Host/Sensitizer, Activator	Gd^{3+} Conc%	Molar ratio (Sensitizer: Activator)	Reaction parameters	Temp. and time
1	$NaYF_4/Yb^{3+},Er^{3+}$	0 mol % Gd^{3+}	20:2	Ethanol 20mL OA 25 mL NaOH 1 mL NaF 0.85 g	200 ℃ 20 hours
2	$NaYF_4/Yb^{3+},Er^{3+}$	30 mol % Gd^{3+}			
3	$NaYF_4/Yb^{3+},Er^{3+}$	50 mol% Gd^{3+}			
4	$NaYF_4/Yb^{3+},Er^{3+}$	70 mol% Gd^{3+}			

The influence of Gd^{3+} doping on crystallite size distribution and crystal phase of $NaYF_4:Yb^{3+}$, Er^{3+} nanoparticles are listed in Table 3-2. The range of width and length were obtained by measuring the smallest and largest values observed in SEM images of upconversion nanoparticles. The values have been estimated to integer value for convenience.

Table 3- 2 illustrates the summary of the phase, size, and size distribution of the $NaYF_4$:Yb^{3+}, Er^{3+} (20, 2) nanocrystals with various concentrations of Gd^{3+} dopant ions (0 mol%, 30 mol%, 50 mol%, and 70 mol%)

Sample	Concentrations of Gd^{3+} doping	Phase	Width (nm)	Length (nm)
$NaYF_4$:Yb^{3+}, Er^{3+}	0 mol%	Cubic	50-100	50-100
		Hexagonal	300-500	1900-2200
$NaYF_4$:Yb^{3+}, Er^{3+}	30 mol%	Hexagonal	200-450	700-1000
$NaYF_4$:Yb^{3+}, Er^{3+}	50 mol%	Hexagonal	130-490	600-950
$NaYF_4$:Yb^{3+}, Er^{3+}	70 mol%	Hexagonal	150-550	200-700

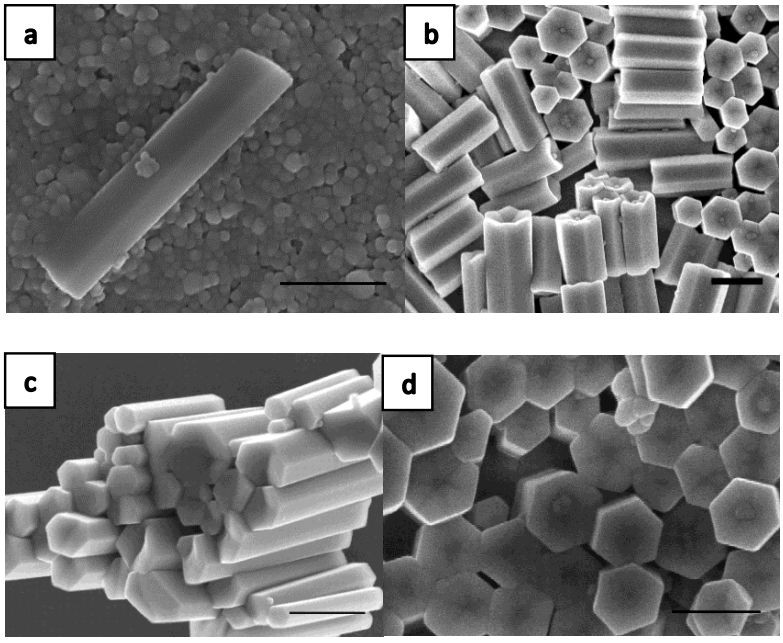

Figure 3- 3 (a-d) SEM images of $NaYF_4$: Yb^{3+}, Er^{3+} (20, 2 mol%) nanoparticles doped with various concentrations of Gd^{3+} ions. The scale bar in figure (a-d) are 500 nm.

Figure 3-3(a) confirmed the co-existence of hexagonal phase and cubic phase $NaYF_4$. Clearly, there were significant differences in morphology as a function of the dopant concentration of Gd^{3+}. Figure 3-3(b) demonstrated that pure hexagonal phase of $NaYF_4$ was formed when the Gd^{3+} ion concentration reached 30 mol%, and this as-prepared sample was of good crystallite size uniformity. In addition, the length of the nanorods decreased gradually when the Gd^{3+} doping concentration increased from 30 mol% to 70 mol%. The transition from cubic phase to hexagonal phase could be well controlled by modulating the doping concentration of Gd^{3+}. In view of geometry of UCNPs, 30 mol% Gd^{3+} doped sample shows larger physical dimension, high crystallinity and a smaller ratio of surface area to volume. On the contrary, both 50 mol% and 70 mol% Gd^{3+} doping samples have a relatively smaller size, less homogenous morphology, and lower crystallinity. High Gd^{3+} concentrations are associated with an increase of unwanted surface impurities, ligands and lattice defects, which could change the origin phonon energy of the host matrix. Moreover, the size ranges become broader when the Gd^{3+} doping content is raised from 30 mol% to 70 mol%, indicates the tendency of less homogeneity with a higher concentration of lanthanide doping. Notably, when the Gd^{3+} ions are doped into the $NaYF_4$:Yb^{3+}, Er^{3+} nanoparticles, hexagonal tubes have a protruding centre and distortional tubular structure with the end face convex in the centre and concave between the centre and the edge. The evolution of morphology can be partly attributed to the surface modification effect of dopant Gd^{3+} ions on crystal growth.[16]When the Gd^{3+} doping concentration is 30 mol%, and F^-/Ln^{3+} molar ratio is calculated as 8:1, the obtained UCNPs are the most uniform ones and have the smoothest morphologies among the three lanthanide doping samples.

3.3.2 Predominant role of the energy transfer (ET) upconversion

In a typical Sensitizer–Activator-coupled UCNPs system, ground state absorption/excited state absorption (GSA/ESA), energy transfer upconversion (ETU) and cooperative sensitization (CS) are three

main mechanisms for upconversion.[17] ETU, which comprises multiple competing transitions between multiple energy levels in the Yb^{3+} - Er^{3+} couples system, is considered to be the most efficient mechanism in upconversion process.[18,19] $NaYF_4:Er^{3+},Yb^{3+}$ exhibits a combination of ESA and ETU process. Er^{3+} ion is excited from the ground-state $^4I_{15/2}$ to the excited-state $^4I_{11/2}$ by one of the two following processes: ground-state absorption by absorbing one 980 nm laser photon (GSA), or energy transfer (ET) from the excited Yb^{3+} ions

$$^4I_{15/2}\ (Er) + {}^2F_{5/2}\ (Yb) \rightarrow {}^4I_{11/2}\ (Er) + {}^2F_{7/2}\ (Yb) \qquad \text{(Equ 3-2)}$$

Then, the ions in the $^4I_{11/2}$ state can be immediately excited to the $^4F_{7/2}$ level of Er^{3+} ions by absorbing another Yb^{3+} ion. The Er^{3+} ions could decay non-radiatively to the luminescent states $^2H_{11/2}$, $^4S_{3/2}$, and $^4F_{9/2}$. Furthermore, the Er^{3+} ions at the excited state $^4I_{11/2}$ could undergo a non-radiative decay to the $^4I_{13/2}$ level and subsequently be excited to the $^4F_{9/2}$ state by absorbing a second 980 nm photon.[20]

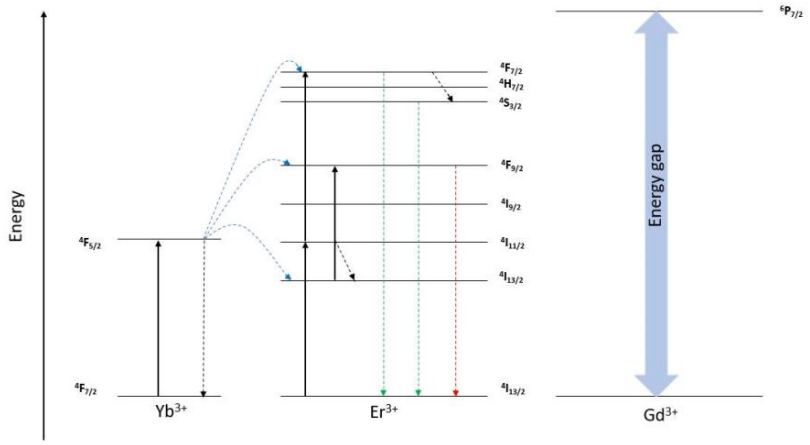

Figure 3- 4 Energy level diagram and upconversion mechanism for the Yb^{3+} and Er^{3+} and Gd^{3+} co-doped UCNPs system upon 980 nm laser excitation. The large energy gap of Gd indicates that the doping of extra Gd ions will not change the original energy transfer pathway of $NaYF_4:Er^{3+},Yb^{3+}$.

As illustrated in figure 3-4, three major emission peaks centered at 520 nm, 540 nm, and 656 nm are observed in the range of UV to visible light spectrum, where two green emissions at 520 nm and 540 nm are assigned to the $^2H_{11/2} \rightarrow {}^4I_{15/2}$ and $^4S_{3/2} \rightarrow {}^4I_{15/2}$ transition, respectively; and the red emission at 656 nm is assigned to the $^4F_{9/2} \rightarrow {}^4I_{15/2}$ transition. The UCPL of Er^{3+} and Yb^{3+} ions co-doped nanoparticles excited by a 980 nm laser emit yellowish green light, which is a combination of green and red color emissions. In brief, the unique properties of UCPL is owing to the intra 4f-4f orbital electronic-dipole transitions of lanthanide ions. The long-lived intermediate energy states in lanthanide ions can be attributed to the quantum mechanical forbidden nature of the 4f-4f transition, which allows energy transfers between two or more ions and favor the successive excitations in a single lanthanide ion.[21] Since Yb^{3+} ions have a much broader absorption cross-section than that of Er^{3+} ions for 980 nm light, the ETU process should play a predominant role among these mechanisms.[22] To investigate the ETU process, figure 3-5(a) and 3-5(b) signify the time evolution of upconversion photoluminescence intensity measured under different excitation duration times of the pulsed laser (109 μs, 1092 μs, 4368 μs, 4586 μs, respectively). These figures comprise both the rise and decay curves of photoluminescence intensity versus time, which are proportional to the population of the excited states of Er^{3+} as a function of time. In terms of decay lifetime, longer time indicates slower decay rate and favours the accumulation of population.[23]

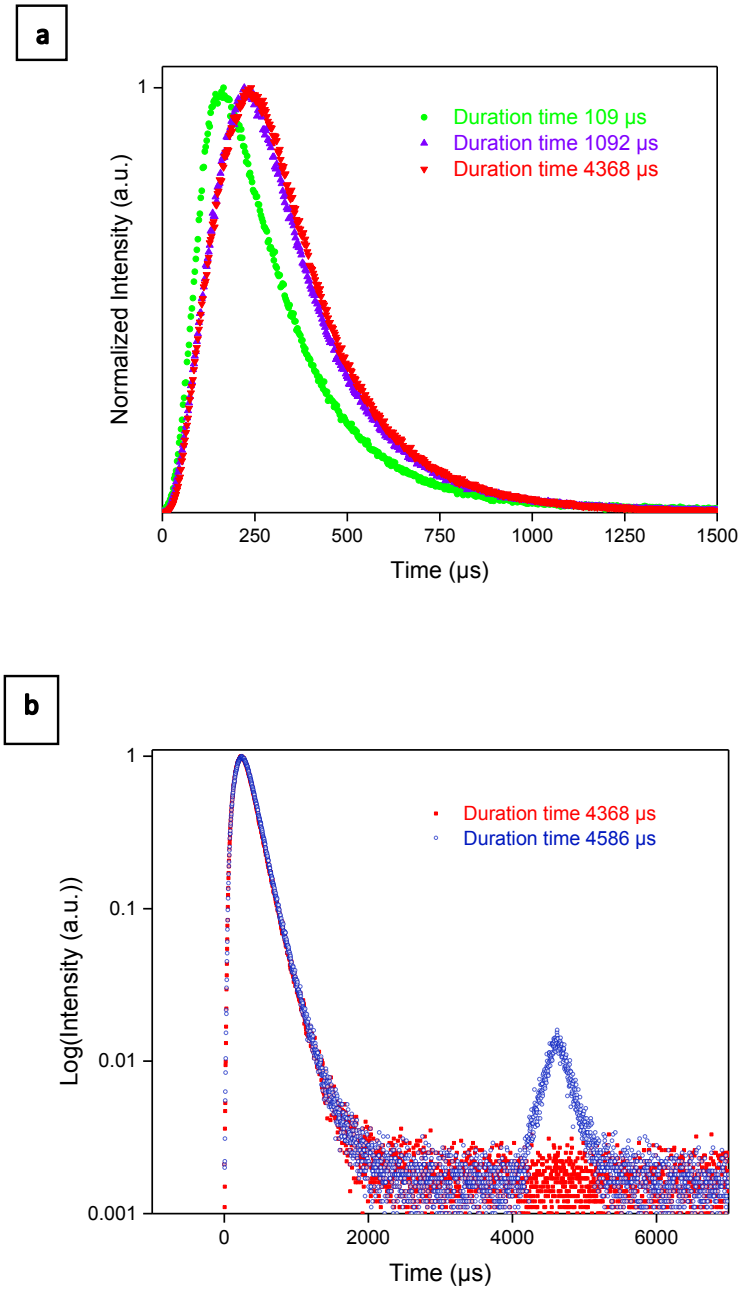

Figure 3- 5 (a) Time evolution of upconversion photoluminescence intensity measured under three different excitation duration times (109 μs, 1092 μs, 4368 μs, respectively) of the pulsed laser. We observed the dynamic picture of rise time versus excitation duration for 30% Gd^{3+} doped $NaYF_4$ sample.

The excitation is 980 nm pulsed laser, and the signals collected are 541 nm emissions. We fitted the values of decay lifetimes and rise lifetimes by using algorithm in DAS6 analysis software, which allows re-convolution analysis of time-domain luminescence data with two exponentials. (b) Time evolution of upconversion photoluminescence intensity measured under two different excitation duration times (4368 μs and 4586 μs, respectively) of the pulsed laser.

The temporal evolution of the photoluminescence of $NaYF_4$ as a function of time can be described by a Vial's type equation[24],

$$I(t)= I_1\exp(-t/\boldsymbol{\tau_D})+I_2\exp(-t/\boldsymbol{\tau_R}) \quad \text{(Equ 3-3)}$$

where I(t) represent the photoluminescence intensity at a specific time point corresponding to the on and off of the pulsed laser. $\boldsymbol{\tau_D}$ is decay lifetime of the UCPL, which can be influenced by the lifetime of excited emitting level and the lifetime of energy levels that feed the emitting level via the ET process. While $\boldsymbol{\tau_R}$ represents the rise time, which is also influenced by the lifetime of the emitting state and ET rate. We observed a pronounced rise lifetime dependence on excitation duration for 30% Gd^{3+} doped $NaYF_4$ sample. Within the entire measurement range of 11,000 μs, as the pulsed laser duration times prolonged from 109 μs to 1092μs, the rise time was delayed from 74.6 μs to 125.3 μs. It was revealed that all GSA/ESA excitation only occurs within the duration of a short laser pulse, when the sample is irradiated.[25] In contrast, the contribution of ETU process can be identified by the slower increase rate and delayed maximum in the time evolution picture of the GSA/ESA and ETU co-existence upconversion photoluminescence. Interestingly, four times longer duration time, 4368 μs, leads to only a slight increased rise time, compared with the 1092 μs duration time measurement. With further extension of the duration time to 4586 μs, there were negligible change of rise time. This result could be attributed to the saturation of the intermediate levels.[10] The appearance of a secondary peak at 4600 μs in figure 3-5(b) corresponds to the

initiation of re-excitation of the ground state when the duration time (4586 μs) reached a critical period of time (T_c). Thus, in the following measurements, duration time of 4368 μs was selected to overcome the restriction of re-excitation effect.

3.3.3 Gd^{3+} concentration dependent photoluminescence lifetimes

In order to demonstrate the Gd^{3+} dopant concentration dependent photoluminescence dynamics, the lifetime decay curves of the green (550 nm) and red (656 nm) emissions of $NaYF_4$:Yb^{3+}, Er^{3+}, Gd^{3+} were measured in samples with increased concentration of Gd^{3+} dopant under excitation of 980 nm pulsed laser.

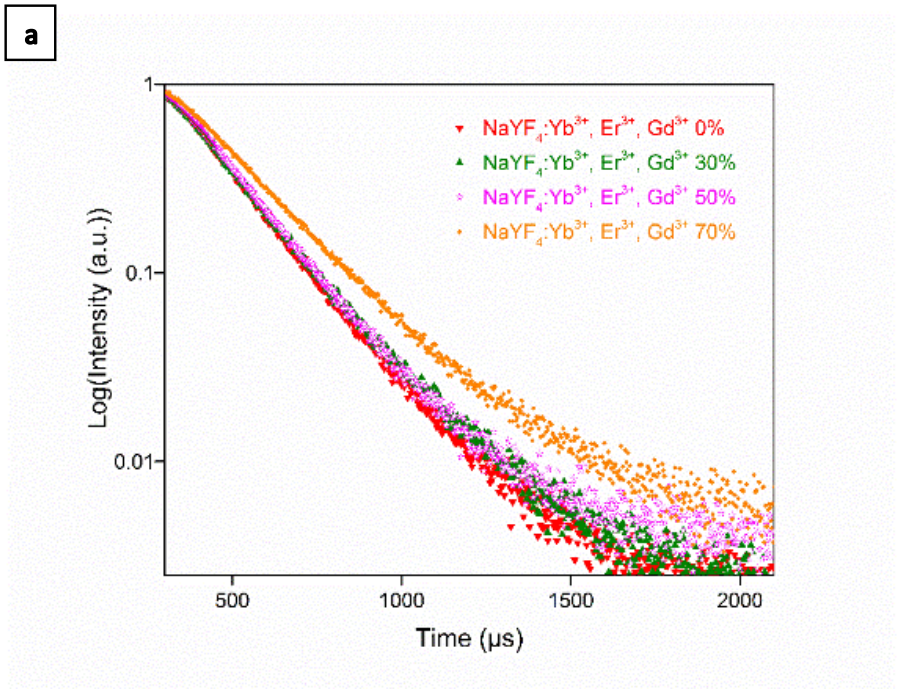

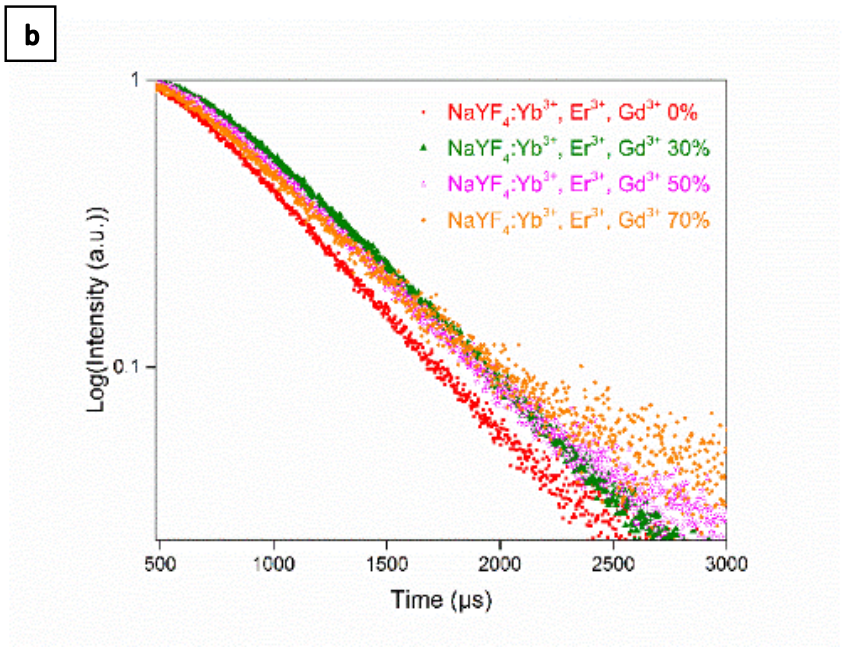

Figure 3- 6 (a) Decay curves for the green emission (540 nm) of $NaYF_4$ doped with different molar ratio of Gd^{3+} ions. (b) The decay curves for the red emission (656 nm) of $NaYF_4$ doped with different molar ratio of Gd^{3+} ions.

Table 3- 3 Photoluminescence lifetimes of green emission (540 nm) and red emission (656nm) for $NaYF_4$ samples, with different Gd^{3+} molar concentration.

Samples	0% Gd^{3+}	30% Gd^{3+}	50% Gd^{3+}	70% Gd^{3+}
Lifetime 540 nm	194.44μs ±0.38 μs	209.62μs ±0.62 μs	211.61μs ± 0.82 μs	232.43μs ± 0.43 μs
Lifetime 656 nm	442.69μs ±3.14 μs	495.13μs ±2.62 μs	499.84μs ±3.04 μs	503.69μs ±2.43 μs

The results in table 3-3 shows that the decay lifetime $\boldsymbol{\tau}$ in creased with the increase of Gd^{3+} concentration. Clearly, the photoluminescence lifetimes of both green and red emissions were prolonged accordingly as a function of increasing the molar concentration of Gd^{3+} doping in $NaYF_4$. In case of samples doped with 30 mol%, 50 mol% Gd^{3+} ions, the green lifetimes increase slightly from 209.62$\boldsymbol{\mu s}$ to 211.61$\boldsymbol{\mu s}$, and from 495.1 $\boldsymbol{\mu s}$ to 499.8 $\boldsymbol{\mu s}$ for red emission. Theoretically, the lifetime ($\boldsymbol{\tau}$) of an excited state is expressed as,[26]

$$1/\boldsymbol{\tau}=1/\boldsymbol{\tau_{rad}}+1/\boldsymbol{\tau_{nr}}+\boldsymbol{k_{ET}} \qquad \text{(Equ 3-4)}$$

where $\boldsymbol{\tau_{rad}}$ represents the radiative decay, $\boldsymbol{\tau_{nr}}$ represents the non-radiative decay lifetime, and $\boldsymbol{k_{ET}}$ is energy transfer rate. As previously results informed, the upconversion process is dominated by ETU mechanisms in the sensitizer to activator (S-A) coupled system (figure 3-7). Dexter's theory[27] described the relationship of energy transfer probability ($\boldsymbol{W_{S-A}}$) and the S-A separation ($\boldsymbol{r_{S-A}}$), which can be simplified as,

$$\boldsymbol{W_{S-A}} \propto \frac{\mathbf{1}}{(\boldsymbol{R_{S-A}})} \qquad \text{(Equ 3-5)}$$

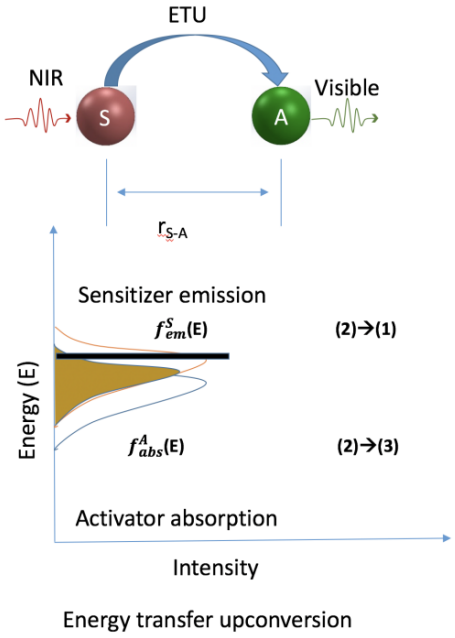

Figure 3- 7 Schematic diagram of energy transfer upconversion (ETU) in sensitizer to activator, (S-A) coupled system.

This relationship indicates that S-A separation is a significant factor influencing the energy transfer probability. The strong dependence of energy transfer rate on the interionic distance, $(\boldsymbol{r_{S-A}})$ directly leads to the significance of sensitizer and activator ions concentration in the host of UCNPs. With the increased Gd^{3+} ions doped into the $NaYF_4$ nanocrystals, more Y^{3+} and Yb^{3+} ions were substituted by Gd^{3+} in the crystal lattice of $NaYF_4$. With the average S-A separation($\boldsymbol{r_{S-A}}$) increased accordingly, a decreased energy transfer rate between sensitizer and activator could lead to the prolonged lifetime of $NaYF_4$ Nanocrystals.

3.3.4 Tuning of the upconversion quantum yield

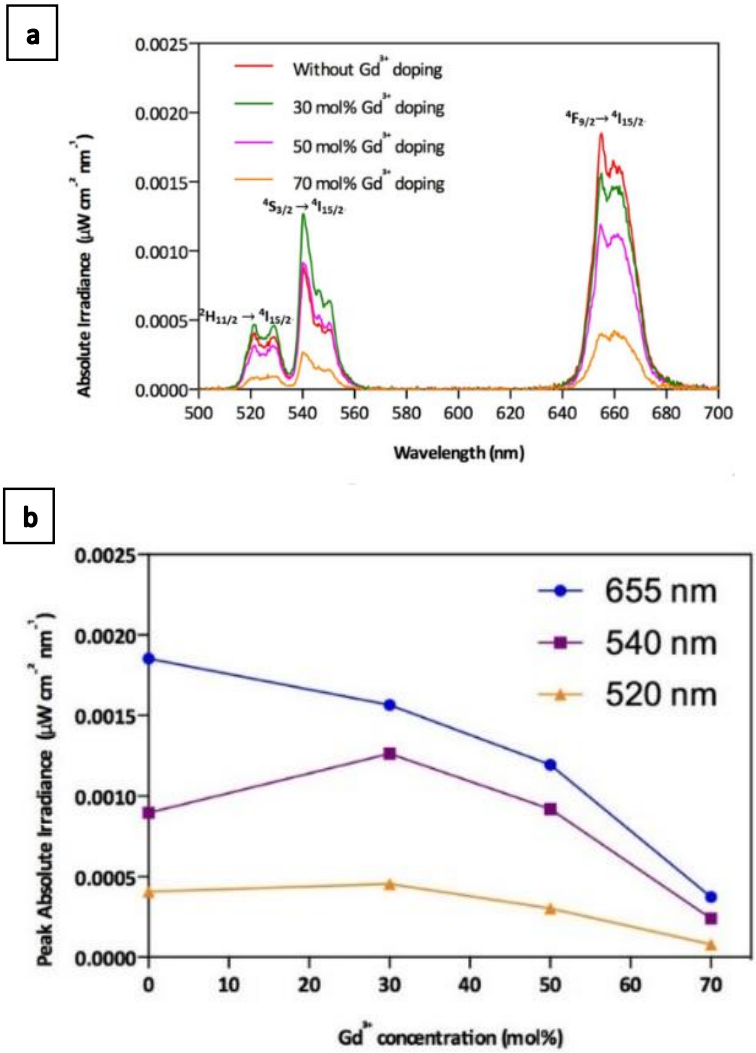

Figure 3- 8 (a) Irradiance of UCPL spectra of the resulting $NaYF_4:Yb^{3+}$, Er^{3+} when tuning the Gd^{3+} dopant molar concentration from 0 to 70 mol% upon 980 nm laser excitation. 3-8 (b) shows the UC luminescence intensity at 656 nm, 540 nm, and 520 nm versus different Gd^{3+} doping concentration (0, 30 mol%, 50 mol%, and 70 mol%).

Figure 3- 9 This figure demonstrates the white precipitates of UC nanoparticles under 980 nm laser excitation at an input intensity of 4.13 W cm^{-2}. A yellowish green was obtained under 980 nm laser excitation.

To investigate the photoluminescence of $NaYF_4:Yb^{3+}$, Er^{3+} UCNPs as a function of the Gd^{3+} concentration, the absolute quantum yields of upconversion nanoparticles were measured (figure 3-8a). Clearly, the absolute quantum yield of both green light emission (500 nm-570 nm) and red emission (620 nm-700 nm) varied as a function of the Gd^{3+} ions doping concentration. The calculated quantum yields at different emission bands with various Gd^{3+} concentrations are summarized in table 3-4.

Table 3- 4 Absolute Internal Upconversion Quantum Yield values at different wavelengths (521 nm, 541 nm, 656 nm represent the center of different upconversion emissions) of UCNPs doped with various Gd^{3+} concentrations.

Gd^{3+} Conc.%	0%	30%	50%	70%
521 nm	0.196%	0.177%	0.116%	0.037%
541nm	0.338%	0.379%	0.266%	0.081%
656 nm	1.445%	0.991%	0.720%	0.276%
Total	1.980%	1.548%	1.102%	0.394%

In figure 3-8(a), the shapes of the emission spectra for the four samples are similar, which suggests the same combination of upconversion pathways for these as-prepared samples. Besides, the intensity ratio of green and red emission demonstrated a remarkable change as a result of the incorporation of Gd^{3+} ions into $NaYF_4$: Yb^{3+}, Er^{3+} host lattice. With 30 mol% Gd^{3+} doping, the UC luminescence efficiency is enhanced at 540 nm and 520 nm, compared to those without doping. However, the highest emission peak occurs at 656 nm when Gd^{3+} ions are not doped into the $NaYF_4$:Yb^{3+}, Er^{3+} UC systems. These results reveal that the suitable lanthanide doping and controlled dopant ion concentration are able to modify the UCPL efficiency at selective wavelengths. In the perspective of the ladder-like energy levels in the sensitizer and activator, Gd^{3+} doping induces large local distortion in crystal lattice, reducing the site symmetry of the activators. Therefore, the probabilities of different pathways in the ETU process could be changed due to the modified lattice symmetry, unit cell parameters and intra-4f transition probability. In addition, the iUCQY were proved to be in correlation with the evolution trend of UCPL lifetimes. Therefore, both the UCPL lifetimes and iUCQY were proved to be influenced by the tailoring of ETU efficiency.

3.4 Conclusions

In summary, we demonstrate that UCPL lifetimes and iUCQY at selective emissions can be tuned by varying the molar concentration of the Gd^{3+} ions. In addition, the properties of UCPL are identified highly sensitive to the energy transfer rate between the sensitizer and activator. Based on the precise control of UCPL lifetimes in the wide range timescale, this doping strategy make it possible to create extra temporal-domain coding dimension promising significant potential for practical multiplexed applications. The low upconversion quantum yield was measured in this study, which indicates their limitations to be applied in solar energy systems.

This chapter represents our initial trial of synthesis high efficiency upconversion nanoparticles by hydrothermal method. Based on previous work of Wang, F. *et al.*[13], we modified the synthesis strategy, further explored the influence of lifetime by introducing extra ion Gd^{3+}. Experimental results show that both upconversion photoluminescence and upconversion emission lifetimes can be modified by this doping strategy. However, the minor improvements still cannot meet the requirements of high efficiency upconversion for practical applications. As a result, we will explore the UCPL enhancement of UCNPs by plasmonic substrates in the next chapter.

Reference

1. Lu, Y. *et al.* Tunable lifetime multiplexing using luminescent nanocrystals. *Nature Photonics* 8, 32, doi:10.1038/nphoton.2013.322 information (2013).
2. Resch-Genger, U., Grabolle, M., Cavaliere-Jaricot, S., Nitschke, R. & Nann, T. Quantum dots versus organic dyes as fluorescent labels. *Nature Methods* 5, 763, doi:10.1038/nmeth.1248 (2008).
3. Gnach, A. & Bednarkiewicz, A. Lanthanide-doped up-converting nanoparticles: Merits and challenges. *Nano Today* 7, 532-563, doi:https://doi.org/10.1016/j.nantod.2012.10.006 (2012).
4. Deng, R. & Liu, X. Tunable lifetime nanocrystals. *Nature Photonics* 8, 10, doi:10.1038/nphoton.2013.353 (2013).
5. Wang, F. & Liu, X. Multicolor Tuning of Lanthanide-Doped Nanoparticles by Single Wavelength Excitation. *Accounts of Chemical Research* 47, 1378-1385, doi:10.1021/ar5000067 (2014).
6. Zhou, J., Liu, Q., Feng, W., Sun, Y. & Li, F. Upconversion Luminescent Materials: Advances and Applications. *Chemical Reviews* 115, 395-465, doi:10.1021/cr400478f (2015).
7. Li, C. & Lin, J. Rare earth fluoride nano-/microcrystals: synthesis, surface modification and application. *Journal of Materials Chemistry* 20, 6831-6847, doi:10.1039/C0JM00031K (2010).
8. Dyck, N. C., van Veggel, F. C. J. M. & Demopoulos, G. P. Size-Dependent Maximization of Upconversion Efficiency of Citrate-Stabilized β-phase NaYF4:Yb3+,Er3+ Crystals via Annealing. *ACS Applied Materials & Interfaces* 5, 11661-11667, doi:10.1021/am403100t (2013).
9. Wang, J. *et al.* Photon energy upconversion through thermal radiation with the power efficiency reaching 16%. *Nature Communications* 5, 5669, doi:10.1038/ncomms6669 (2014).
10. Wu, X. *et al.* Upconversion Nanoparticles: A Versatile Solution to Multiscale Biological Imaging. *Bioconjugate Chemistry* 26, 166-175, doi:10.1021/bc5003967 (2015).

11. Li, Z. *et al*, Multicolor Core/Shell-Structured Upconversion Fluorescent Nanoparticles, *Advanced Materials*, 20, 4765-4769. doi:org/10.1002/adma.200801056 (2008)
12. Zhang, F., Wan, Y., Shi, Y., Tu, B. & Zhao, D. Ordered Mesostructured Rare-Earth Fluoride Nanowire Arrays with Upconversion Fluorescence. *Chemistry of Materials* 20, 3778-3784, doi:10.1021/cm800489e (2008).
13. Wang, F. *et al.* Simultaneous phase and size control of upconversion nanocrystals through lanthanide doping. *Nature* 463, 1061, doi:10.1038/nature08777 (2010).
14. Wahl, M., Rahn, H.-J., Gregor, I., Erdmann, R., and Enderlein, J., Dead-time optimized time-correlated photon counting instrument with synchronized, independent timing channels, *Review of Scientific Instruments*,78, 033106, (2007)
15. Gargas, D. J. *et al.* Engineering bright sub-10-nm upconverting nanocrystals for single-molecule imaging. *Nature Nanotechnology* 9, 300, doi:10.1038/nnano.2014.29 (2014).
16. Shang, Y. *et al.* Synthesis of Upconversion β-NaYF4:Nd3+/Yb3+/Er3+ Particles with Enhanced Luminescent Intensity through Control of Morphology and Phase. *Nanomaterials* 5, doi:10.3390/nano5010218 (2015).
17. Villanueva-Delgado, P., Krämer, K. W. & Valiente, R. Simulating Energy Transfer and Upconversion in β-NaYF4: Yb3+, Tm3+. *The Journal of Physical Chemistry C* 119, 23648-23657, doi:10.1021/acs.jpcc.5b06770 (2015).
18. Park, W., Lu, D. & Ahn, S. Plasmon enhancement of luminescence upconversion. *Chemical Society Reviews* 44, 2940-2962, doi:10.1039/C5CS00050E (2015).
19. Lu, D., Mao, C., Cho, S. K., Ahn, S. & Park, W. Experimental demonstration of plasmon enhanced energy transfer rate in NaYF4:Yb3+,Er3+ upconversion nanoparticles. *Scientific Reports* 6, 18894, doi:10.1038/srep18894 (2016).

20. Ding, M. *et al.* Simultaneous morphology manipulation and upconversion luminescence enhancement of β-NaYF4:Yb3+/Er3+ microcrystals by simply tuning the KF dosage. *Scientific Reports* 5, 12745, doi:10.1038/srep12745 (2015).
21. Chen, G., Qiu, H., Prasad, P. N. & Chen, X. Upconversion Nanoparticles: Design, Nanochemistry, and Applications in Theranostics. *Chemical Reviews* 114, 5161-5214, doi:10.1021/cr400425h (2014).
22. Xu, S. *et al.* Upconversion fluorescence spectroscopy of Er3+/Yb3+-codoped lead oxyfluorosilicate glass. *Chemical Physics Letters* 385, 263-267, doi:https://doi.org/10.1016/j.cplett.2003.12.104 (2004).
23. Wei, T. *et al.* Mid-infrared fluorescence, energy transfer process and rate equation analysis in Er3+ doped germanate glass. *Scientific Reports* 4, 6060, doi:10.1038/srep06060 (2014).
24. Yu, W., Xu, W., Song, H. & Zhang, S. Temperature-dependent upconversion luminescence and dynamics of NaYF4:Yb3+/Er3+ nanocrystals: influence of particle size and crystalline phase. *Dalton Transactions* 43, 6139-6147, doi:10.1039/C3DT53562B (2014).
25. Yersin, H. & Donges, D. in *Transition Metal and Rare Earth Compounds: Excited States, Transitions, Interactions II* (ed Hartmut Yersin) 81-186 (Springer Berlin Heidelberg, 2001).
26. Chen, G., Liu, H., Liang, H., Somesfalean, G. & Zhang, Z. Upconversion Emission Enhancement in Yb3+/Er3+-Codoped Y2O3 Nanocrystals by Tridoping with Li+ Ions. *The Journal of Physical Chemistry C* 112, 12030-12036, doi:10.1021/jp804064g (2008).
27. Dexter, D. L. A Theory of Sensitized Luminescence in Solids. *The Journal of Chemical Physics* 21, 836-850, doi:10.1063/1.1699044 (1953).

Chapter 4 Enhancing the Upconversion Photoluminescence of Hexagonal Phase $NaYF_4:Yb^{3+}$, Er^{3+} Nanoparticles by Mesoporous Gold Films

4.1 Introduction

As introduced in Chapter 2, upconversion photoluminescence (UCPL) is a nonlinear process, through which one photon at a shorter wavelength is emitted, following successive absorption of two or more photons, at longer wavelengths. Research on lanthanide-doped upconversion nanoparticles (UCNPs) has recently attracted considerable attention, driven by their diverse potential applications, including in solar cells, biomedical imaging, solid-state lasers, display technology, and security printing.[1] Upconversion is one potential approach to enhance the performance of all classes of solar cells, and is theoretically predicted to be able to increase the efficiency above the Shockley-Queisser limit.[2] The Shockley–Queisser limit, refers to the maximum theoretical efficiency of a solar cell using a single p-n junction to collect power from the cell. Currently, the dominant losses (about 35%) of solar cell efficiency are due to the sub-band-gap energy losses.[3] An efficient luminescence upconversion system could potentially improve the efficiency of traditional solar cells, by harvesting the otherwise lost sub-band-gap photons in the solar spectrum. However, the efficiency of the most promising upconversion materials, $NaYF_4$ host lattice doped with Yb^{3+}/Er^{3+}, remains low due to the small absorption cross sections arising from formally forbidden *f-level* atomic transitions of the dopants.[4] As a result, there is negligible progress in the enhanced performance of devices by incorporating upconversion materials. A very recent report[5] demonstrated a 7.9% power conversion efficiency (PCE) enhancement of perovskite solar cells by placing the upconversion single crystal on the front of the device. Improving the efficiency of UCNPs is urgently needed for their practical applications, especially in solar cells. The emerging field of plasmon-enhanced upconversion is a promising avenue for improving the upconversion efficiency of rare-earth (RE) doped materials. To date, a number of plasmonic geometries such as nanograting,[4] disk-coupled dots-on-pillar

antenna array[6] and core-shell nanostructure[7,8] have been investigated for enhancing UCPL. These nanostructures lead to the UCPL enhancement from 2.3 times[8], to tens of times[9,10], to about 300 times,[6] respectively. In our opinion, the wide range of such enhancement factors being reported are not comparable, as the individual systems reported have different pumping power. In addition, the enhancement factors are also relying on various factors such as the choice of plasmonic materials, the structural morphology, the distance between UCNPs and nanostructure surface and the optical properties of UCNPs and plasmonic nanostructures *etc.* However, the difficulties in fabricating high quality plasmonic substrates over a large area, without stringent experimental conditions, still hinder the practical applications of plasmon enhanced upconversion luminescence. In some cases, the plasmons even quenched rather than enhanced emission.[11,12]

In this work, we utilized a three-dimensional (3D) mesoporous gold (Au) film by a free corrosion dealloying process, to enhance the UCPL of hexagonal phase β-$NaYF_4$:Yb^{3+}, Er^{3+} co-doped nanocrystals (Figure 4-3a). This dealloying approach is effective for producing mesoporous Au substrates with tuneable pores sizes, extended framework. Compared with other reported plasmonic structures, the mesoporous Au films have a large area and uniform distribution of porous nanospaces. Due to the existence of abundant nanospaces, these structures also exhibit high carrier density, provide surfaces with sufficient functional sites and thus fascinating optical properties.[13] Moreover, the fabrication method utilized is low-cost, large-scale and easy to control. In this work, by tuning the pore size of mesoporous Au films, a 41-fold luminescence enhancement over a large area (~1.0 cm^2) was achieved. A localized surface plasmon resonance (LSPR) was measured experimentally at ~550 nm due to the nanopores. To obtain physical insights of UCPL enhancement, both the red emission and green emission lifetimes were measured, together with electromagnetic modelling. It was found that, for green emission (~540 nm), the

enhancement was dominated by non-resonant enhancement at the pumping wavelength which increased with increasing pore size. While for red emission (~650 nm), both emission enhancement and field enhancement contributed to the UCPL enhancement. This chapter is based on the published paper: Qin, H. *et al.* Enhancement of the upconversion photoluminescence of hexagonal phase $NaYF_4$:Yb^{3+}, Er^{3+} nanoparticles by mesoporous gold films. Physical Chemistry Chemical Physics **19**, 19159-19167, doi:10.1039/C7CP01959A (2017).

4.2. Experimental

4.2.1 Materials and methods

All reagents were of analytical grade. Yttrium (III) chloride anhydrous powder (YCl_3 99.9%), Erbium(III) chloride anhydrous powder ($ErCl_3$ 99.9%), Ytterbium (III) chloride anhydrous powder ($YbCl_3$ 99.9 Ammonium fluoride (NH_4F ≥99.99% trace metals basis), Sodium hydroxide (NaOH ACS reagent, ≥97.0%, pellets) and 1-Octadecene (technical grade, 90%) was purchased from Sigma-Aldrich. Oleic Acid (OA 70%) was purchased from Fisher Chemical (UK). All alloy silver/gold used in this work was purchased from Sepp Leaf Products (New York). Concentrated nitric acid (HNO_3) (Sigma Aldrich, ACS reagent, ≥90.0%) and 18.2 Megohm-cm Ultrapure water) were used.

4.2.2 Fabrication of mesoporous gold films

The silver and gold (Ag-Au) alloy films were bought commercially from Sepp Leaf Products (New York). Silver and gold (Ag-Au) alloy films, with the thickness of ~100 nm, were floated on the surface of concentrated nitric acid (HNO_3), based on a method described by Ding *et al.*,[16] as illustrated in Figure 4-1. The samples were exposed to the acid solution for different times (1 min, 3 min, 10 min, 30 min, 2 h, 12 h, 24 h, 3 days, or 8 days), to study the effect of dealloying time on the morphology and pore sizes of

mesoporous Au film (Figure 4-4, Figure 4-5). The leaf was then transferred to ultrapure water for 35 min to completely quench the dissolution and diffusion reactions. The floated films were then "fished" out of the solution on the surface of glass substrates previously coated with an amine self-assembled monolayer, by treating them with 4% v/v APTES (aminopropyltriethoxysilane) in acetone. This amine monolayer has a high affinity to Au atoms, increases adhesion of the Au film to the glass substrate and prevents its delamination during following processing steps. The fished samples were finally allowed to dry in ambient atmosphere and used for morphological and optical characterization, and subsequent fabrication processes.

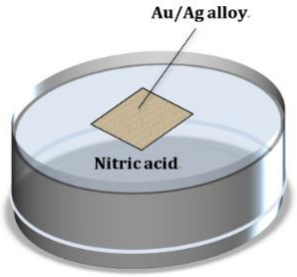

Figure 4- 1 Schematic illustration of the free corrosion dealloying process used to fabricate Au mesoporous films.

4.2.3 Synthesis of β-$NaYF_4$:Yb^{3+}, Er^{3+} UCNPs by co-precipitation method

In chapter 3, we applied a hydrothermal method to synthesis $NaYF_4$:Yb^{3+}, Er^{3+} upconversion nanoparticles. However, considering the size and phase of as-prepared UCNPs are hard to control, a different approach co-precipitation synthesis process[22,23] was applied in this chapter. Chloride-based rare earth precursors Yttrium Chloride (YCl_3 99%), Ytterbium Chloride ($YbCl_3$ 99%), and Erbium Chloride ($ErCl_3$ 99%), were used as a dopants precursor. To fulfil the percentage composition, 0.75 mmol of Yttrium Chloride (YCl_3 99%), 0.064 mmol of Ytterbium Chloride ($YbCl_3$ 99%), and 0.02 mmol of Erbium

Chloride ($ErCl_3$ 99%) were all mixed into three-neck round-bottom flask with 4 mL of Oleic Acid (OA) and 15 mL of Octadecene (ODE). All of the mixtures then heated at 150 C in the open environment to remove all of the unnecessary elements such as oxygen and water for 40 minutes. The colour of the mixture should change from soft yellowish cloudy transparent to clear strong yellowish solution. The change of colour indicates that all of the powder precursors had been dissolved completely. Then 2.5 mmol of sodium hydroxide (NaOH) in 5 mL methanol and 4 mmol of ammonium fluoride (NH_4F) in 5 mL methanol were prepared separately and sonicated for about 15 minutes to be fully dissolved. Afterwards, both of them were quickly injected into the dopant solution at room temperature with vigorous stir. After injection sodium hydroxide and ammonium fluoride methanol solution simultaneously, the mixed solution of dopant and crystal host solution was heated up to 50 C for 30 minutes under vacuum to remove methanol. Then, the solution was continued to be heated up to 320 C under gentle argon gas flow for 90 minutes. Finally, the UCNPs product were washed and centrifuged (4500 r.p.m.) by ethanol and cyclohexane in sequence and was repeated for 3 times, respectively. The colloid of UCNPs in cyclohexane can be stored in a refrigerator (4 C) for further use.

4.2.4 Characterisation of UCNPs and plasmon-enhanced upconversion structure

The particle size, size distribution, phase, and homogeneity of as-synthesized UCNPs were characterized by transmission electron microscopy (JEOL JEM-2100F,) combined with energy-dispersive X-ray spectroscopy (EDX, Oxford Instruments, UK), under an accelerating voltage of 200 kV. In brief, the resulting white precipitates of synthesized UCNPs were dispersed in cyclohexane by ultrasonic sonication for 30 minutes. Several drops of the suspension were drop-casted onto a carbon-coated copper TEM grid. Finally, the samples were allowed to dry in air for 120 minutes and analysed by TEM. Scanning electron microscopy (SEM) was performed using a LEO Gemini 1525 field emission gun (FEG) SEM (Carl Zeiss Microscopy GmbH, UK), to further characterize the phase and phase distribution of UCNPs. The

suspension was then drop-casted onto a clean transparent glass substrate. Then, a 10 nm layer of gold (Au) was sputter-coated on the surface of the glass substrate with UCNPs, to inhibit charging and reduce thermal damage. SEM was also used to investigate the surface morphology of Au mesoporous substrates.

4.2.5 Optical characterization

UV Visible (UV-vis) absorption spectroscopy was performed using the Agilent Cary 5000 UV-Vis-NIR spectroscopy system, to characterize the plasmonic properties of the mesoporous Au films. Glass substrates were used for holding all the samples, as they do not have a restricted wavelength range within our scanning range. Scans were performed over the range from 300-2400 nm, using a scanning rate of 100 nm/min, and a bandwidth of 0.1 nm. The baseline correction was performed using clean glass substrates. All the spectra presented here were obtained using un-polarized light.

4.2.6 Photoluminescence (PL) Measurements

The fluorescence emission measurements were obtained using a Fluorolog®-3 Spectrofluorometer system from Horiba Scientific, equipped with a LSR980H steady state laser with adjustable power supply from LASEVER. The angle of acquisition was fixed at 30° for accuracy and consistency of the measurements. The samples were excited by 980 nm NIR light laser excitation with a power density of $500\ \mathrm{mW \cdot cm^{-2}}$ and the upconversion emissions were measured in the range of 450-700 nm, using a 5 nm slit size. The enhancement factor due to the plasmonic Au substrates was estimated using the equation:

$$E = \frac{I_{UC,NPG} - I_{Glass}}{I_{UC,Glass} - I_{Glass}} \qquad \text{(Equ 4-1)}$$

Where $I_{UC,NPG}$ represents the upconversion photoluminescence intensity obtained from UCNPs coated on top of a mesoporous Au substrate, while I_{Glass} represents the noise signal from clean glass substrate. This equation does not include any corrections for the surface area coverage of the UCNPs. Since our

substrates were prepared by the drop casting technique, which means the UCNPs densities on both Au mesoporous film and glass control were identical. This was further confirmed by counting the numbers of UCNPs within the same area on both surfaces of SEM images (Figure 4-7(a), (b)). Therefore, the UCPL enhancement observed is only due to the plasmonic influence of Au mesoporous films.

4.2.7 Photoluminescence Lifetime measurement

Time-correlated single-photon counting (TCSPC), which is considered as the most sensitive digital technique for determining photoluminescence lifetimes, was applied to obtain dynamic pictures of upconversion photoluminescence of the as-prepared samples.[25] We used the 980 nm pulsed laser to statistically characterize the time dependent photoluminescence emission profiles of the as-synthesized UCNPs by repeating the excitation-emission process up to 5000 counts. The DD-980L laser source has a peak wavelength at 980±10 nm, an extremely narrow 100 picosecond pulse width, 0.2 mW power on average and the repetition rate is 50MHz.

4.3 Results and discussions

4.3.1 Plasmon-enhanced upconverters

A simple and reproducible plasmonic upconversion structure was fabricated, as illustrated in Figure 4-2. The structure was composed of four parts: a transparent glass substrate for support, a mesoporous Au layer, followed by an approximate 8 nm SiO_2 spacer layer (thickness was controlled by a sensitive detector of Mantis Deposition System), and a sub-monolayer of the UCNPs on top. The fabrication of mesoporous Au films on glass substrates was based on a free-corrosion dealloying process, which produces continuous Au films with a wide range of tuneable pore sizes.[16,17,18] By exposing Au films to a concentrated nitric

acid solution for varying times, the morphology and pore size of mesoporous Au films could be modified.[18,19]

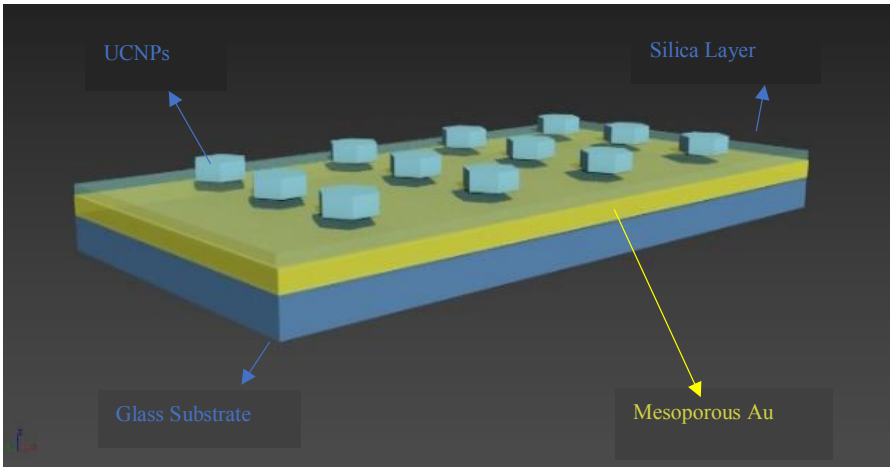

Figure 4- 2 Schematic diagram of the plasmon-enhanced upconversion structure designed and fabricated in this work. The structure was composed of four major components: (i) glass substrate on the bottom, (ii) gold (Au) mesoporous film, (iii) silica (SiO_2) spacer layer, and (iv) β-$NaYF_4$:Yb^{3+}, Er^{3+} UCNPs sub-monolayer.

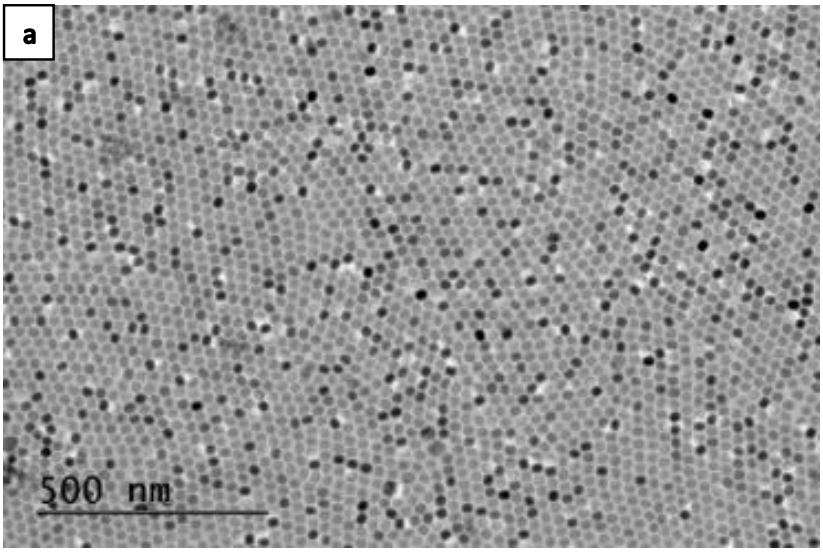

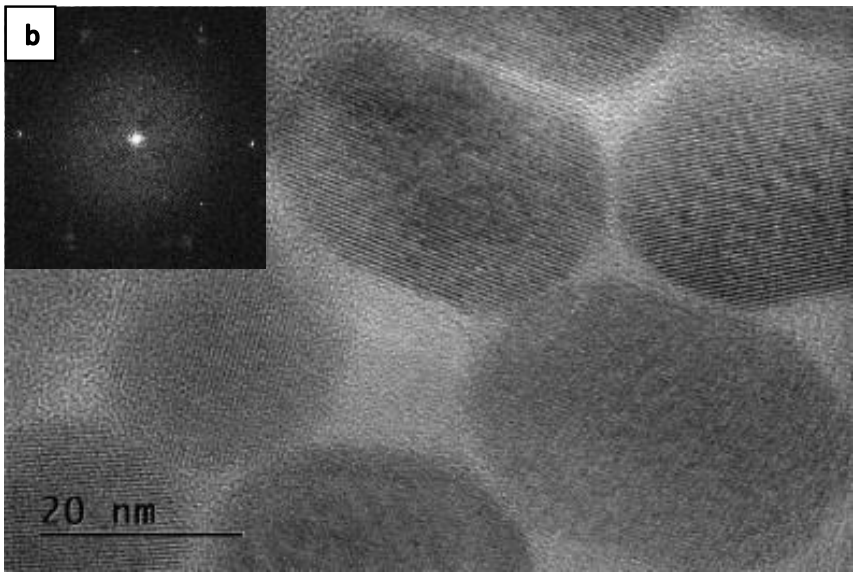

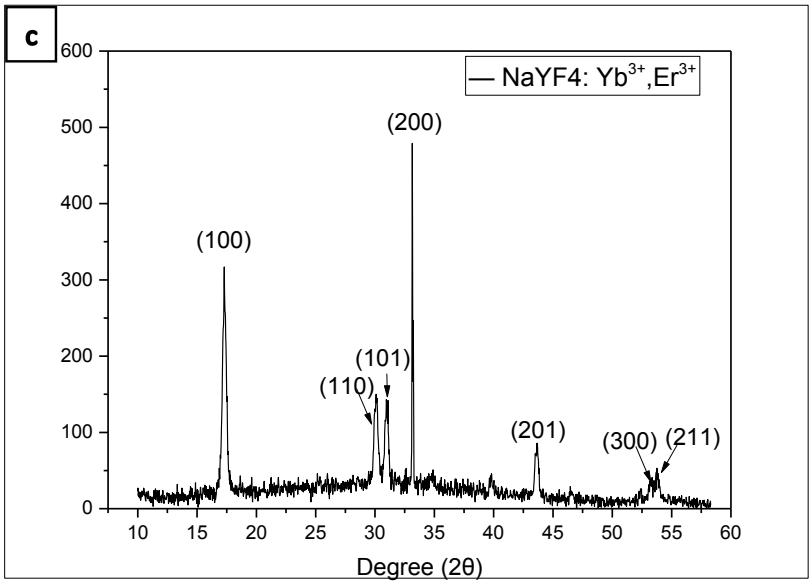

Figure 4- 3 (a) Transmission electron microscopy (TEM) image of hexagonal β-$NaYF_4$:Yb^{3+}, Er^{3+} nanocrystals. (b) High resolution (HR) TEM image of UCNPs with 300K magnification. The inset of Figure 4-3(b) is the live-FFT diagram of the UCNPs. (c) X-ray powder diffraction (XRD) pattern of β-$NaYF_4$:Yb^{3+}, Er^{3+} UCNPs.

In our study, hexagonal phase β-$NaYF_4$:20% Yb^{3+}, 2% Er^{3+} nanoparticles were synthesized by a thermal decomposition method. As shown in the transmission electron micrograph (TEM) in Figure 4-3a, the nanoparticles were hexagonal in shape and with mean vertical length of 36.1 nm (standard deviation of σ = 4.06 nm, for n=100 nanoparticles), with a lateral length of 25.5 nm (standard deviation of σ = 1.4 nm, for n=100 nanoparticles). The X-ray powder diffraction (XRD) pattern (Figure 4-3b) further confirmed that the UCNPs consisted of pure hexagonal phase $NaYF_4$ nanoparticles (β-NaYF4-JCPDS 16-0334). The crystal host doped with combinations of rare earth elements Yb^{3+} and Er^{3+} provides an opportunity to study UCPL in both the green and red regions of the spectrum, when illuminated under 980 nm laser.

4.3.2 Morphological and compositional analysis of mesoporous Au films

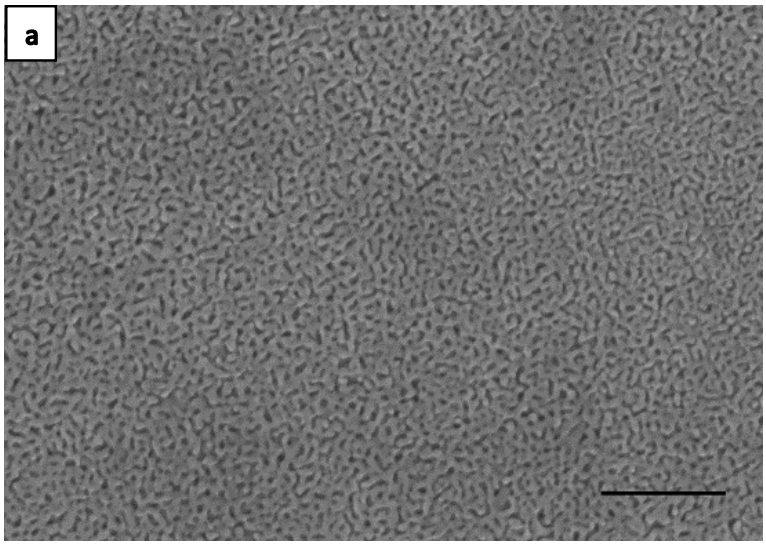

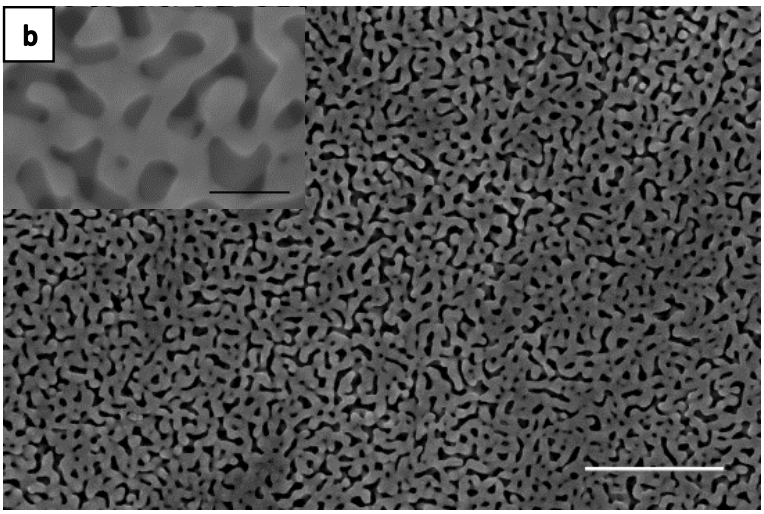

Figure 4- 4(a) Top-view SEM micrographs showing the porosity of Au mesoporous film with 2 hours dealloying time (with 500 nm scale bar and 50K magnification). (b) Top-view SEM micrographs showing the porosity of Au mesoporous film with 72 hours dealloying time (with 1000 nm scale bar). The inset of Figure 4-4(b) is Au mesoporous film with 72 hours dealloying time with higher magnification. The scalebar in the inset in 150 nm.

The Au mesoporous films used in this chapter were provided by Ahmed Shamso. When as-received Ag-Au alloy films (Ag-Au, with equal weights of Ag and Au alloy films and very thin cross section down to below 100nm) were floated on the surface of concentrated nitric acid through surface tension, Ag dissolution started immediately, initiating the dealloying process. Dealloying of the films was visually apparent by the change of their colour (from shiny golden to yellowish brown) SEM imaging revealed the porosity evolution of the films with dealloying time of 1 minutes and 8 days, respectively, which led to an increase in ligament and average pore sizes (Figure 4-4 (a), 4-4 (b) and Figure 4-5 (c)) in agreement with published literature.[19] For UCPL enhancement study, we only choose representative four samples, i.e. samples with dealloying times of 3 min, 10 min, 12 hours, and 8 days. The corresponding average pore sizes are 5 nm, 15 nm, 52 nm, and 72 nm, respectively. The significant decrease of Ag content with

time due to dissolution results in more pores generated in the structure of Au film. After 3 days of dealloying, the pore size reached its plateaus. The residual Ag content of the mesoporous Au films, which depends on dealloying time, was investigated by SEM-EDX analysis of the entire sample (Figure 4-5 (b)). EDX analysis showed that the Ag content declined rapidly after reaction with HNO_3. In these experiments Ag was not detected for dealloying times greater than 30 min, which could be attributed to the presence of Ag contents lower than the detection limit, but previous work[19] suggests that up to 8% Ag is trapped inside the Au ligaments.

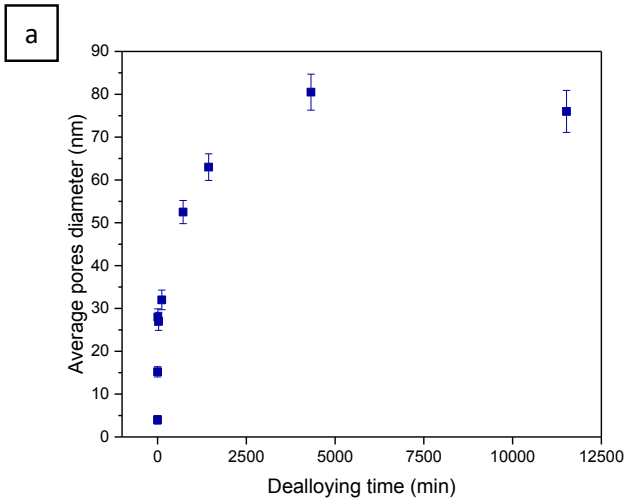

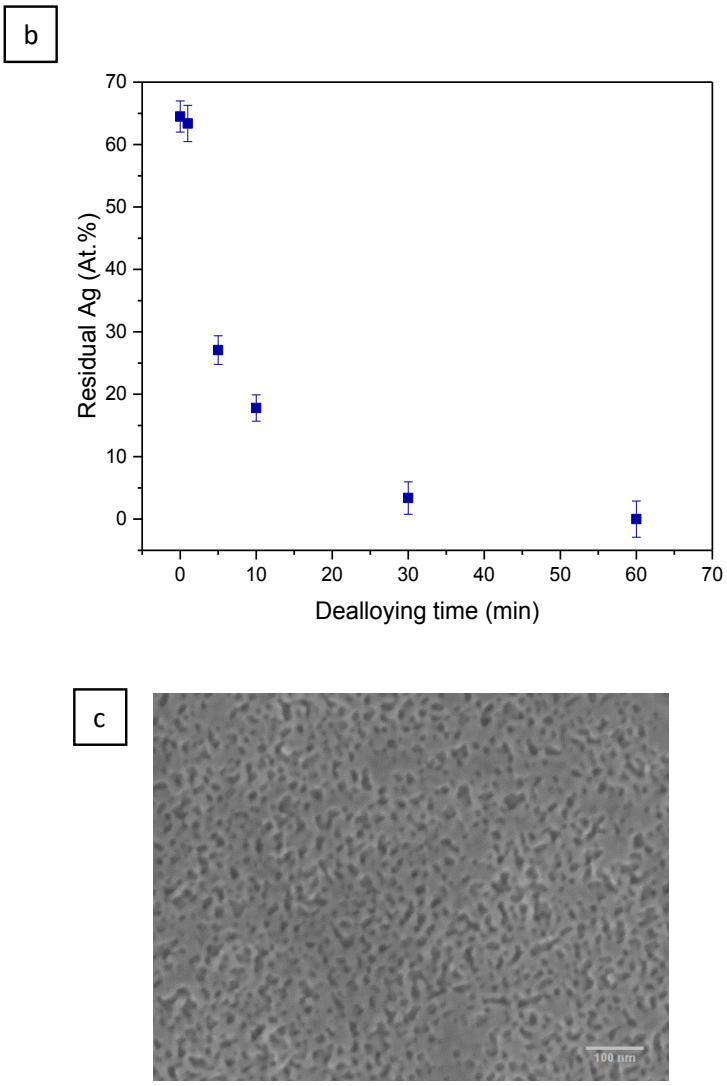

Figure 4- 5(a) Average pore size evolution as a function of dealloying time. (b) Residual silver content of Au mesoporous films as a function of dealloying time. (c) Top-view SEM micrographs showing the Au mesoporous film with 3 minutes dealloying time.

In addition to Ag dissolution, surface diffusion of Au is responsible for the porosity evolution. At the very early stages of reaction, the porous network is not continuous following dealloying times of 3 minutes (Figure 4-5(c)), and the porosity was not uniformly distributed. As dealloying times increased beyond 5

minutes, the porous structure becomes homogenous and well-developed, and porosity evolution becomes dominated by the surface diffusion processes. A growth in ligament size and spacing was observed, since Au atoms rearrange themselves in such a way to lower their free energy and entropy. Adjusting dealloying process parameters such as the alloy composition, time and temperature enable us to control the surface features of mesoporous Au films for the optimization of their specific performances. The optical properties of mesoporous films are in turn controlled by these resultant surface morphology and chemistry, features that can be tailored by processing time.

4.3.3 Plasmonic enhancement of β-$NaYF_4$:Yb^{3+} Er^{3+} UCNPs

Photoluminescence (PL) spectroscopy was used to investigate the plasmon-enhanced upconversion photoluminescence by the Au mesoporous films. The upconversion emission spectra of UC nanocrystals deposited on a series of plasmon-enhanced structures under 980 nm laser excitation with a power density of ~ 500 $mW \cdot cm^{-2}$ are shown in Figure 4-6(b).

a

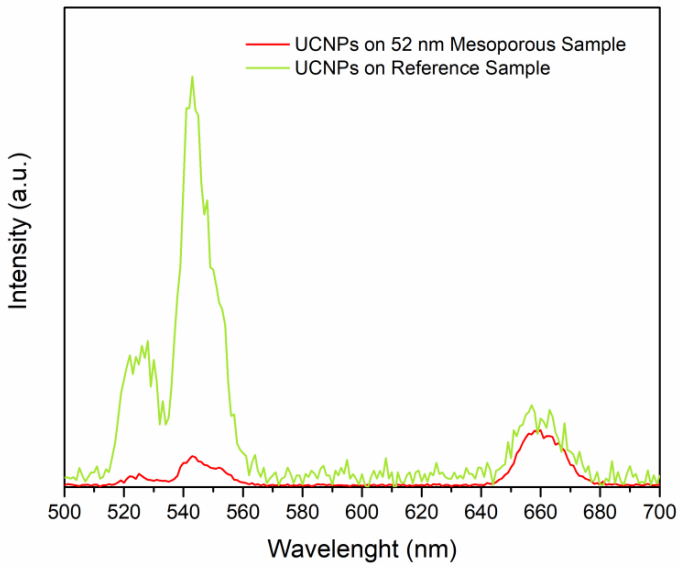

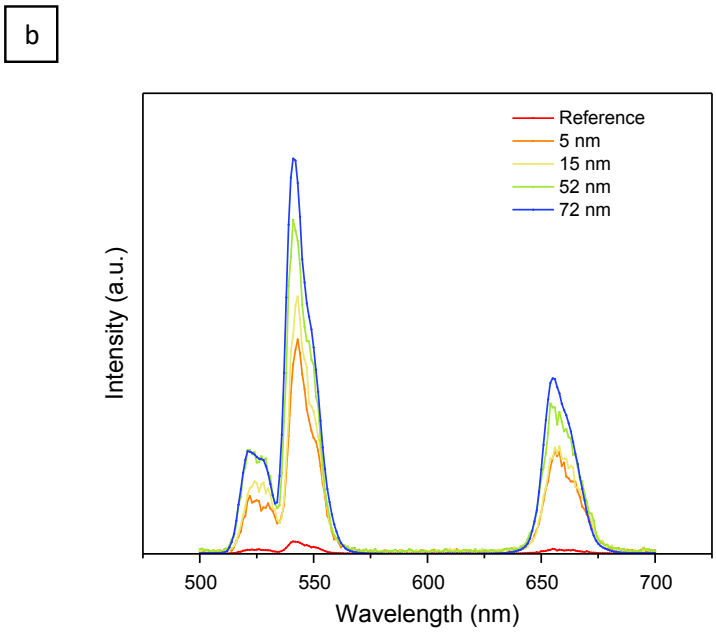

Figure 4- 6 (a) UCPL intensity of β-$NaYF_4$:Yb^{3+}, Er^{3+} nanoparticles on reference sample (glass) and 52nm Au mesoporous sample directly without 8 nm SiO_2 spacer layer. This measurement shows strong quenching effect at 541 nm emission and at 656 nm emission. (b) UCPL intensity of β-$NaYF_4$:Yb^{3+}, Er^{3+} NPs on reference substrate (glass) and Au mesoporous films with pore sizes of 72 nm, 52 nm, 15 nm and 5 nm, corresponding to different dealloying time for 8 days, 12 hours, 10 min, and 3 min, respectively.

This figure shows three main emission peaks centred at 520 nm, 540 nm, 660 nm, resulting from $^2H_{11/2}\rightarrow{}^4I_{15/2}$, $^4S_{3/2}\rightarrow{}^4I_{15/2}$, and $^2S_{9/2}\rightarrow{}^4I_{15/2}$ energy transitions in the Er^{3+} rare-earth ions, respectively. It has been previous reported that the effect of plasmonic structures on upconversion can be two competing processes, either enhancement or surface quenching, which is very distance sensitive.[20] The electromagnetic (EM) field strength decays exponentially as a function of inverse sixth-power distance away from the plasmonic surface.[21] In our case, UCPL measurement demonstrated a strong quenching effect of UCPL (Figure 4-6(a)), when UCNPs were deposited directly on mesoporous Au substrates without a spacer layer. In this situation, the emissions of UCNPs relaxed rapidly by nonradiative energy

transfer into the surface plasmon resonance. At an optimised distance from the plasmonic surface, fluorescence resonance energy transfer (FRET) from UCNPs to the Au plasmon surface is decreased, while the enhanced EM field can still strong enough to improve the UCPL efficiency. As shown in table 4-1, it was demonstrated that the PL signals was significantly enhanced on Au mesoporous film samples with 8 nm SiO_2 spacer. The PL intensity of UCNPs on mesoporous Au film with 72 nm averaged pore size, exhibited the best enhancement performance with 32X and 41X enhancement factors, for peaks centred at 541 nm and 656 nm, respectively. There are two main pathways of enhancement: excitation enhancement and emission enhancement. Excitation enhancement indicates the improvement of light absorption of sensitizer ions as a result of the dramatically strengthened local electric field (E) in the vicinity of the surface of plasmonic nanostructure. In parallel, emission enhancement indicates an increase of radiative decay rate of the activator doped in UCNPs, which can be significantly increased due to coupling between electrons and phonons.[26] Theoretical studies show that when a UCNP is located at the vicinity of a metallic structure, an effective coupling exists between the transition dipole of the UCNP and the SPR-induced electric field. The fundamental characteristic of excitation enhancement is that it directly enhances the local field of the UCNPs, thereby causing higher emission intensities without changing the intrinsic characteristics of decay processes. In contrast, emission enhancement occurs due to the increased radiative decay rate, reduced quenching effect and lower localized temperature.[10] In light of these considerations, the observed enhancement in upconversion efficiency can possibly due to both metal-induced enhancement of absorption of the excitation pump at 980 nm (excitation enhancement) *and* plasmonic enhancement of the emission of the UCNPs (emission enhancement).

Table 4- 1 UCPL enhancement factors at 541 nm and 656 nm, with respect to averaged pore size of 5 nm, 15 nm, 52 nm and 72 nm, respectively. Mesoporous substrates have 8 nm SiO_2 spacer layer. Note that the

enhancement factors have been corrected based on the densities of the UCNPs on glass and Au film substrates.

Averaged pore size	λ_e =541 nm	λ_e =656 nm
5 nm (3 min)	18	22
15 nm (10 min)	20.9	22.7
52 nm (12 hours)	27.2	32.4
72 nm (8 days)	32	41

Besides the significant enhancement factors, a clear trend was also observed that the UCPL signals were a function of the dealloying time, i.e., with the increase in the mesopore size and the reduction of residual Ag content in the mesoporous film. (Figure4- 6 and Table 4-1). After 3 days of dealloying process, the pore size of the mesoporous Au film reached its plateau. The film became unstable and fragile with extended dealloying times longer than 8 days. The increased enhancement factors with increasing pore sizes, indicating significantly increase interaction between electromagnetic waves with mesoporous gold surface at visible/NIR region, is possibly due to increased electromagnetic field enhancement around bigger pores. The plasmon oscillation of the free electrons around the centre of the uniform nanopores can effectively collect and confine light from the near-infrared (NIR) to the visible region into the cavity areas, building up a high density of 'hot spots' in the nanopores,[13,14] suggesting a significant upconversion photoluminescence enhancement is possible due to this electric field enhancement. The random coverage of UCNPs on the mesoporous Au film (Figure 4-7) means that there is still further potential to improve the enhancement, by adjusting the pore size of the mesoporous Au with respect to the size of UCNPs, as well as the distribution of UCNPs.

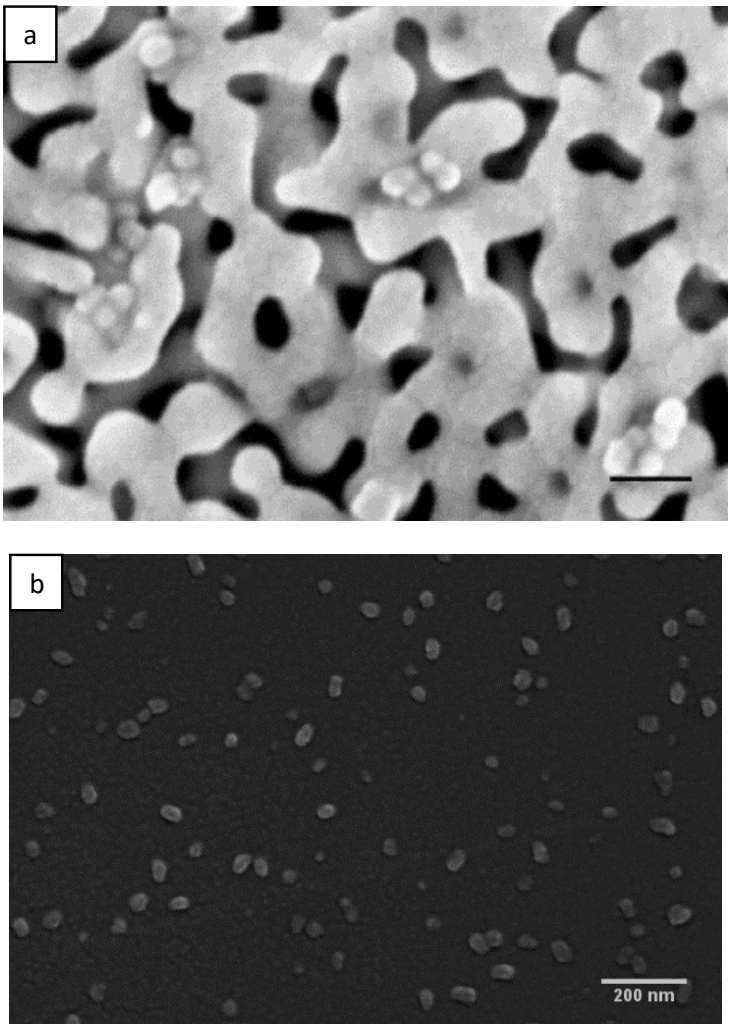

Figure 4- 7 (a) Top-view scanning electron microscopy (SEM) image of the UCNPs sub-monolayer deposited on 72 nm mesoporous Au substrates dealloyed for 8 days. The scalebar in this figure is 100 nm. (b) Top-view SEM micrographs showing the reference sample - glass substrate with UCNPs on the top. (With 120K magnification).

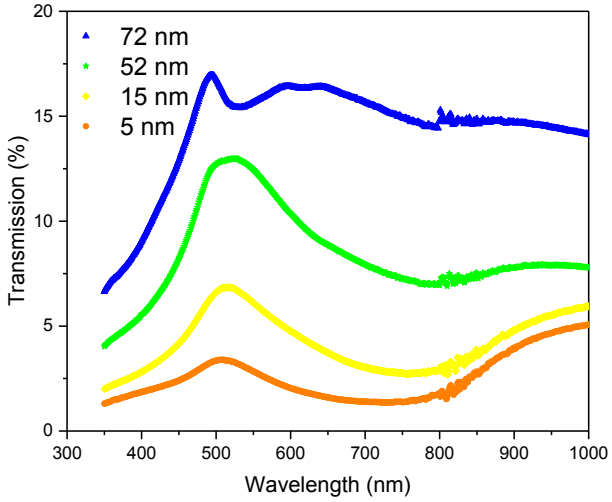

Figure 4- 8 UV-Visible spectroscopy measurement of Au mesoporous films with different pore sizes of 72 nm, 52 nm, 15 nm and 5 nm, which corresponding to different dealloying time for 8 days, 12 hours, 10 min and 3 min, respectively.

To investigate the fundamental optical properties of the mesoporous Au films, UV Visible (UV-vis) spectroscopy measurements were performed on selected mesoporous Au films. Figure 8 shows the UV-Vis transmission spectra corresponding to Au mesoporous films with averaged pore sizes of 5 nm, 15 nm, 52 nm and 72 nm, respectively. Structural imperfections, pore size distribution, surface roughness and residual Ag content may all affect the optical behaviour of Au films. The localised plasmon resonance is observed in all cases at around 530 nm and there is a slight red-shifting with increased pore size. The other observation is that the spectra has a broader band as the pore size increases, indicating a tuneable interaction of the mesopore structures with electromagnetic waves in the broad frequency region. As presented in Figure 4-8, the transmission of light increased gradually with the increase in the averaged pore size. Clearly, there is a spectral overlap between the 541 nm emission of UCNPs and the UV-Visible

spectra of mesoporous films, which may lead to the radiative energy transfer from 541 nm green emission to Au mesoporous film. This energy transfer effect may contribute to the fact that enhancement factors for green emissions (at 541 nm) was slightly weaker than red emissions (at 656 nm), table 4-1.

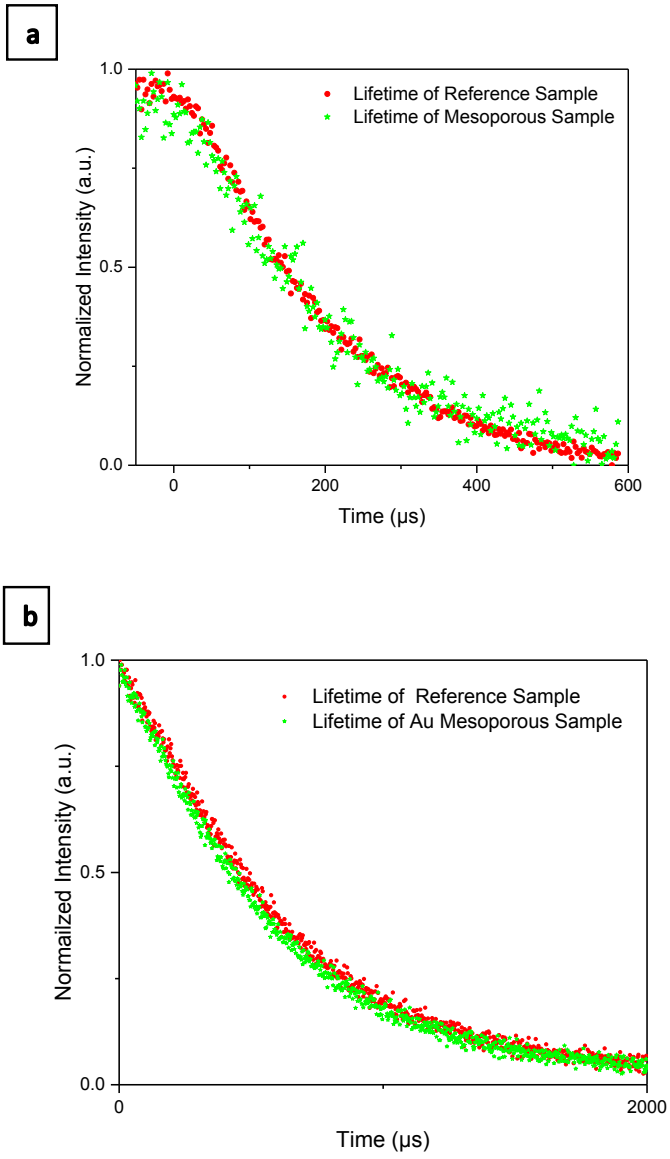

Figure 4- 9 (a) Time-resolved measurement of the upconversion emission at 541 nm of UCNPs. (b) Time-resolved measurement of the upconversion emission at 660 nm of UCNPs deposited on 12 hours dealloyed

mesoporous Au film (Green dots), and UCNPs deposited on the reference sample-clean glass substrate (Red dots), respectively.

To further obtain insight of the enhancement mechanism, the change in the decay rate of the UCNP at 541 nm was measured by time-resolved UCPL.[33] The decay times were measured by a series of duration controllable pulsed DeltaDiode laser, and the decay curves were fitted by a DAS6 Analysis software expressed as an exponential function:

$$I=A + B*\exp(-i/T) \qquad \text{(Equ 4-2)}$$

Table 4- 2 UCPL lifetimes (τ) at 541 nm and 656 nm, with respect to 52 nm mesoporous substrates (12 hours dealloying time) of and the reference sample, respectively.

Wavelength/Sample	τ at 541 nm	τ at 656 nm
Reference Sample	220 μs	506 μs
Mesoporous Sample	212 μs	467 μs

The decay curve is mainly determined by the second excited level of Er^{3+}, as well as the population of the first excited level of Er^{3+} and Yb^{3+}. The green emission (at 541 nm) lifetime measured on the glass substrate and on the mesoporous Au film were 220 μs and 212 μs, respectively. The two similar decay rates measured here (Figure 4-9(a)) suggest that the emission enhancement of UCPL at 541 nm was negligible. In contrast, the red emission lifetimes obtained from the reference glass sample and mesoporous Au film sample were 506 μs and 467 μs, respectively. The lifetime of upconversion red emission at 656 nm on mesoporous Au film was calculated to be 39 μs, shorter than its original lifetime

exhibited on reference sample. These results suggest that there is negligible enhancement due to the localised surface plasmon resonance.

4.4.4 Electromagnetic study of upconversion photoluminescence

The modelling information in this part is provided by Anthony Centeno. To consider this further electromagnetic modelling using the finite difference time domain (FDTD) technique was carried out.[27,28] The mesoporous structure is fairly random in morphology making it difficult to model using computational electromagnetic techniques. Nevertheless, some insight can be gained by considering a structure with periodic nanoholes with similar diameter to those of the average pore sizes. Here Finite Difference Time Domain (FDTD)[33] is used and the metal considered is 100% Au. A Drude-Lorentz model for Au is used.[34] The center-to-center spacing of the nanoholes is 140% of the hole diameter, and the thickness of the Au film 100 nm. The Au was on a glass slide with an 8 nm Silica film on top of the Au film. Figure 4-10 shows the optical absorption response obtained from the calculations. The results show the localized surface plasmon resonance by a transmission peak (or absorption minimum) which redshifts with hole diameter between 505 nm and 547 nm. These results suggest that the transmission maxima at around 550 nm in Figure 4-8 are the LSPR wavelength of the mesoporous Au films. To consider whether this could lead to emission enhancement small dipoles were placed 10 nm above the Silica film, to try and replicate the emission from the upconversion nanoparticles, similar to the procedure used previously when considering metal enhanced fluorescence[34]. The results are shown in Figure 4-11 for dipoles placed 20 nm above the center of the 72 nm nanohole and midway between adjacent holes (i.e. above the Au film). From Figure 4-11 is can be seen that there is little enhancement or some quenching (enhancement factor <1) around at 540 nm. For 660 nm there is some enhancement in both cases (< 2 times). The results provide further evidence that there will be negligible emission enhancement at 540 nm and some at 660 nm, consistent with the lifetime measurements.

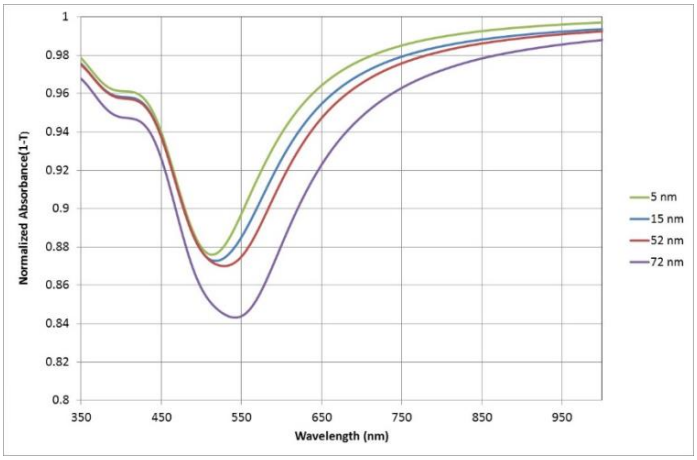

Figure 4- 10 Absorption (1-Transmisison) for 5 nm, 15 nm, 52 nm and 72 nm nanoholes in a 100 nm Au film.

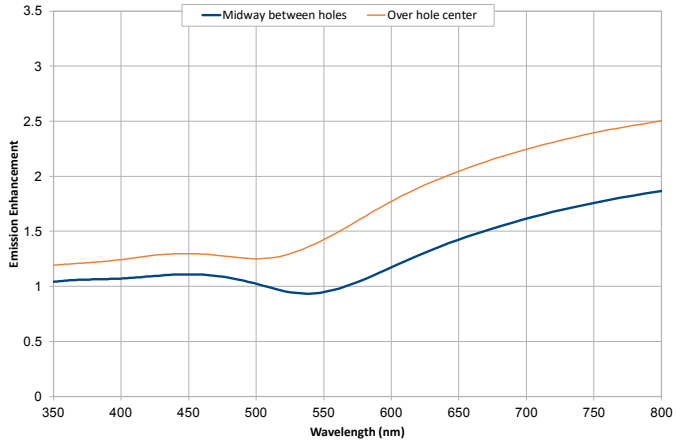

Figure 4- 11 Enhanced emission from a small dipole placed 20 nm above the Au-Nanohole surface.

The experimental and modelling data leads us to believe that the enhancement mechanism is at the excitation wavelength. Figure 4-12 shows the electric field enhancement at 980 nm for the periodic nanohole array with 72 nm holes obtained from the FDTD model. It shows some e-field enhancement but not of the magnitude required to explain the experimental results. The physical mechanism of the excitation enhancement due to the mesoporous films will be investigated in future work.

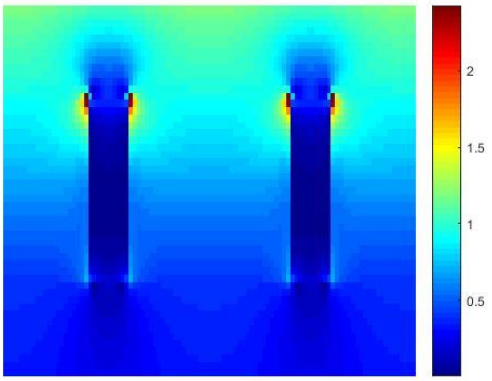

Figure 4- 12 Electric field enhancement at 980 nm (in the cross section through the centre of the holes). The incident plane wave was polarised parallel to the Au surface.

The details of the modelling are followed but to summarize nanoholes of same diameter as the average nanopores were considered in a periodic array. The holes had a depth or 100 nm and the spacing between adjacent holes was considered to be 40% of the hole diameter. The FDTD results (Figure 4-10) showed a red shift (505 nm to 547 nm) with increasing nanopore size (5 nm-72 nm) and a widening of the absorbance bandwidth. By considering small dipoles placed above the mesoporous film FDTD calculations also showed insignificant emission enhancement at 541 nm, and a small enhancement (1.4x-2x) dependent on the placement of the emitter at 656 nm (Figure 4-11). The electromagnetic modelling is in qualitative agreement with the lifetime measurement, in suggesting that the enhancement mechanism is predominantly excitation enhancement and not a plasmonic enhancement of the emission. Further calculated electromagnetic field enhancement at the excitation wavelength for periodic arrays of 72 nm nanoholes shows magnitudes of between 1 and 1.5 in the space above the holes (Figure 4-11). This leads us to believe that the enhancement is due to the random morphology of the mesoporous surface causing non-resonant enhancement. The exact mechanism will be the subject of future investigation. To further

rationalize the observed results of mesoporous Au film enhanced UCPL, one has to consider the intrinsic quantum efficiency of an emitter, Q, which is defined by,[29]

$$Q = k_{rad}/(k_{rad} + k_{nr}) \quad \text{(Equ 4-3)}$$

where quantum efficiency is the ratio of the radiative decay rate (k_{rad}) and nonradiative decay rate (k_{nr}). Note that the emitter quantum efficiency is related but not equivalent to the upconversion efficiency. The UCPL lifetime, which means the average time of excited states spend before relaxations to ground state can be described by equation,

$$\tau = 1/(k_{rad} + k_{nr}) \quad \text{(Equ 4-4)}$$

and it is the inverse of the sum of decay rates of all the decay pathways. Hence, we can get an alternative equation for quantum efficiency,

$$Q = k_{rad} \cdot \tau \quad \text{(Equ 4-5)}$$

Both radiative and nonradiative decay rate can be modified by the presence of the plasmonic surface such as the mesoporous Au film.[30] The plasmonic effect provides extra pathways for UC, alters the emission dynamics and the new UCPL lifetime (τ_0) can be obtained. By comparing steady-state UCPL intensity data and lifetime measurement data between mesoporous sample and reference sample, the enhanced UCPL intensity and decreased lifetime τ_0 at 656 nm indicate an increase of radiative decay rate k_{rad}.[31] On the other hand, the enhanced UCPL intensity but weak change of lifetime at 541 nm suggest negligible decay rate modifications. To understand the plasmonic effect on the pumping power density dependence, the green emission peaked at 541 nm and red emission at 656 nm from the reference sample (UCNPs deposited on clean glass) and the enhanced sample (same amount of UCNPs deposited on 52 nm mesoporous Au substrate) were measured under the same set of excitation power densities, respectively. As a nonlinear effect, the intensity of UCPL (S_{uc}) is simply a function increasing pumping power density (I_{pump}^{n})

$$S_{up} \propto I_{pump}^{n} \quad \text{(Equ 4-6)}$$

UCPL for both green and red emission are dominated by the energy transfer upconversion (ETU). For both green and red emissions, the luminescence intensity exhibited quadratic dependence (n=2) on the excitation power density at low power regime and exhibited linear dependence (n=1) at high power regime.[4,6] As a result, the exponent factor n is expected to decrease from 2 to 1 as I_{pump} is tuned from low power to high power. The population of the second excited level will grows large and S_{up} will saturate at extremely high I_{pump}. Upconversion is a non-linear process, which also means that the upconversion quantum yield of the UCNPs itself increases at stronger power densities.[32]

Table 4- 3 UCNPs exponential factor (n) fitted from the 541 nm and 656 nm UCPL emission intensity as a function of excitation power intensities, with respect to UCNPs deposited on 52 nm (12 hours dealloyed) mesoporous samples and UCNPs deposited on the reference sample (glass), respectively.

Wavelength/Sample	**541 nm**	**656 nm**
Reference Sample	1.70±0.02	1.88±0.03
Mesoporous Sample	1.70±0.02	1.82±0.05

In table 4-3, we can see that the exponential factor n of mesoporous Au enhanced sample equals the reference sample (Figure 4-13(a)), as calculated result shows $n_{Au} = n_{ref}$=1.70±0.02, where the power dependence of the log(I_{pump})-log(S_{uc}) are consistent for both substrates in the low pumping power limit (below 5.35 W/cm^2). Again, consistent with the negligible changed lifetime at green emission (541 nm), the unchanged exponential factor n further confirmed that the enhancement mechanism of UCPL at 541 nm was mainly due to excitation enhancement. While the exponential factors at 656 nm red emission calculated from reference sample is 1.88 ±0.03 and 1.82±0.05 from mesoporous enhanced sample, respectively (Figure 4-13(b)). The slightly reduced exponent factor agrees well with the slightly decreased

lifetime (39 μs), as well as the higher enhancement factor at red emission (656 nm) compared with that at green emission (541 nm). Alternatively, the UCPL enhancement at 656 nm channels suggest the contributions of both excitation enhancement and emission enhancement.

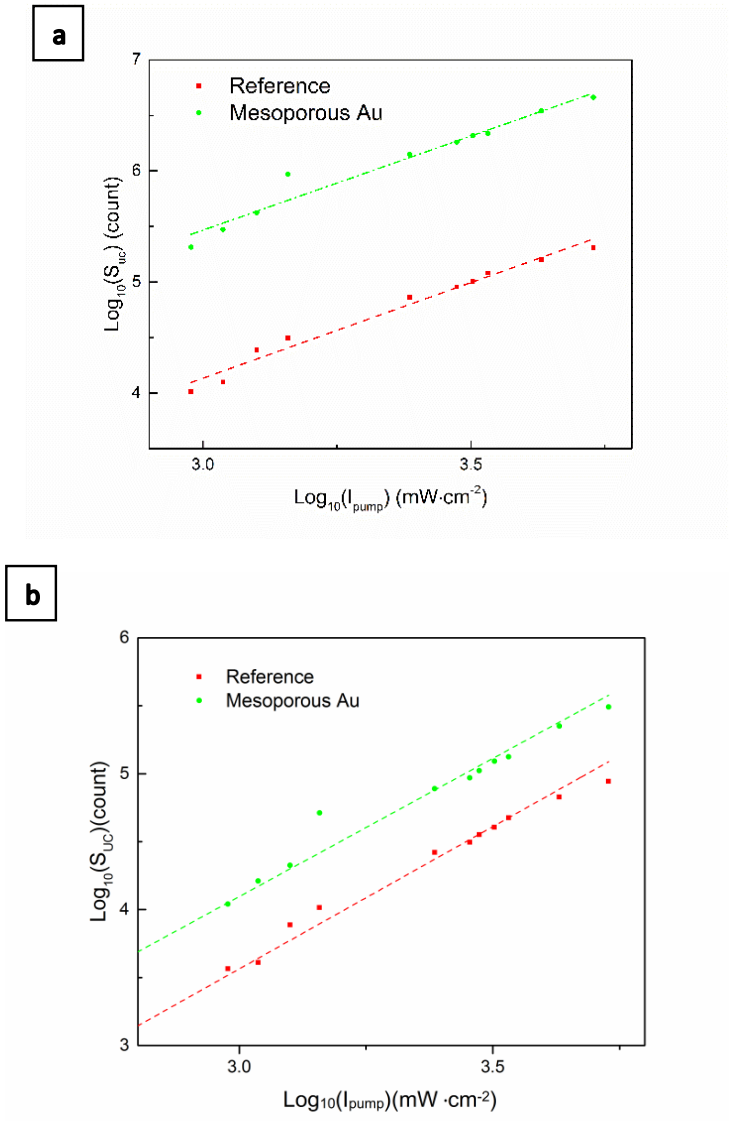

Table 4- 4 (a) Green (541 nm) luminescence intensity of UCNPs as a function of increasing pumping power density of the UCNPs deposited on the 52 nm mesoporous Au film sample (Green line) and UCNPs deposited on the reference sample-clean glass substrate (Red line), respectively. (b) Red (656 nm)

luminescence intensity of UCNPs as a function of increasing pumping power density of the UCNPs deposited on the 52 nm mesoporous Au film sample (Green line) and UCNPs deposited on the reference sample-clean glass substrate (Red line), respectively.

4.5 Conclusions

In summary, 3D mesoporous Au film fabricated by a dealloying process was prepared and optimized by tuning their pore sizes with respect to dealloying times. These films induced significant enhancement of UCPL of β-$NaYF_4$:Yb^{3+}, Er^{3+} co-doped nanocrystals, with significant enhancement (41-fold) over a large uniform area, with constant enhancement factor for low pumping power density. The UCPL enhancement measurements and the time-resolved UCPL study indicate that enhanced UCPL is dominated by the excitation enhancement at 541 nm, and a combination of excitation enhancement and emission enhancement at 656 nm. The high emission intensity enhancement, together with other fascinating advantages, such as low-cost, high throughput and reproducibility, make the plasmonic 3D mesoporous Au film platform an excellent candidate for realizing high efficiency of UCPL.

Despite significant enhancement (41-fold) was obtained by this 3D mesoporous Au film, due to some drawbacks of mesoporous substrates, such as their poor tunability of LSPR. In the next chapter, nanostructures with well-defined feature, periodic and large area nanostructure arrays will be investigated. To realize the practical applications of UCNPs, it is essential to investigate further of the plasmonic enhanced UCPL, via coupling UCNPs to plasmonic nanostructures to increase the quantum efficiency of inherent low quantum yield UCNPs.

Reference

1. Wang, Y.-L. *et al.* Tailoring Plasmonic Enhanced Upconversion in Single NaYF4:Yb3+/Er3+ Nanocrystals. *Scientific Reports* **5**, 10196, doi:10.1038/srep10196
2. Trupke, T., Green, M. A. & Würfel, P. Improving solar cell efficiencies by up-conversion of sub -band-gap light. *Journal of Applied Physics* **92**, 4117-4122, doi:doi:http://dx.doi.org/10.1063/1.1505677 (2002).
3. Verma, D., Saetre, T. O. & Midtgård, O.-M. in *Photovoltaic Specialists Conference (PVSC), 2012 38th IEEE.* 002608-002613 (IEEE).
4. Lu, D. *et al.* Plasmon Enhancement Mechanism for the Upconversion Processes in NaYF4:Yb3+,Er3+ Nanoparticles: Maxwell versus Förster. *ACS Nano* **8**, 7780-7792, doi:10.1021/nn5011254 (2014).
5. Chen, X. *et al.* Highly Efficient LiYF4: Yb3+, Er3+ Upconversion Single-Crystal under Solar Cell Spectrum Excitation and Photovoltaic Application. *ACS Applied Materials & Interfaces*, doi:10.1021/acsami.5b12528 (2016).
6. Zhang, W., Ding, F. & Chou, S. Y. Large Enhancement of Upconversion Luminescence of NaYF4:Yb3+/Er3+ Nanocrystal by 3D Plasmonic Nano-Antennas. *Advanced Materials* **24**, OP236-OP241, doi:10.1002/adma.201200220 (2012).
7. Xu, Z. *et al.* Harvesting lost photons: plasmon and upconversion enhanced broadband photocatalytic activity in core@ shell microspheres based on lanthanide-doped NaYF4, TiO2, and Au. *Advanced Functional Materials* **25**, 2950-2960 (2015).
8. Priyam, A., Idris, N. M. & Zhang, Y. Gold nanoshell coated NaYF4 nanoparticles for simultaneously enhanced upconversion fluorescence and darkfield imaging. *Journal of Materials Chemistry* **22**, 960-965, doi:10.1039/C1JM14040J (2012).

9. Saboktakin, M. *et al.* Metal-Enhanced Upconversion Luminescence Tunable through Metal Nanoparticle–Nanophosphor Separation. *ACS Nano* **6**, 8758-8766, doi:10.1021/nn302466r (2012).

10. Saboktakin, M. *et al.* Plasmonic Enhancement of Nanophosphor Upconversion Luminescence in Au Nanohole Arrays. *ACS Nano* **7**, 7186-7192, doi:10.1021/nn402598e (2013).

11. Wang, F., Wang, J. & Liu, X. Direct evidence of a surface quenching effect on size-dependent luminescence of upconversion nanoparticles. *Angewandte Chemie* **122**, 7618-7622 (2010).

12. Li, Z., Wang, L., Wang, Z., Liu, X. & Xiong, Y. Modification of NaYF4:Yb,Er@SiO2 Nanoparticles with Gold Nanocrystals for Tunable Green-to-Red Upconversion Emissions. *The Journal of Physical Chemistry C* **115**, 3291-3296, doi:10.1021/jp110603r (2011).

13. Li, C. *et al.* Electrochemical synthesis of mesoporous gold films toward mesospace-stimulated optical properties. *Nat Commun* **6**, doi:10.1038/ncomms7608 (2015).

14. Yi, Z. *et al.* Mesoporous gold sponges: electric charge-assisted seed mediated synthesis and application as surface-enhanced Raman scattering substrates. *Scientific Reports* **5**, 16137, doi:10.1038/srep16137

15. Noguez, C. Surface Plasmons on Metal Nanoparticles: The Influence of Shape and Physical Environment. *The Journal of Physical Chemistry C* **111**, 3806-3819, doi:10.1021/jp066539m (2007).

16. Ding, Y., Kim, Y. J. & Erlebacher, J. Nanoporous gold leaf:"Ancient technology"/advanced material. *Advanced Materials* **16**, 1897-1900 (2004).

17. Wang, X., Qi, Z., Zhao, C., Wang, W. & Zhang, Z. Influence of Alloy Composition and Dealloying Solution on the Formation and Microstructure of Monolithic Nanoporous Silver through Chemical

Dealloying of Al−Ag Alloys. *The Journal of Physical Chemistry C* **113**, 13139-13150, doi:10.1021/jp902490u (2009).

18. Dotzler, C. J. *et al.* In Situ Observation of Strain Development and Porosity Evolution in Nanoporous Gold Foils. *Advanced Functional Materials* **21**, 3938-3946, doi:10.1002/adfm.201100735 (2011).
19. Schofield, E. J., Ingham, B., Turnbull, A., Toney, M. F. & Ryan, M. P. Strain development in nanoporous metallic foils formed by dealloying. *Applied Physics Letters* **92**, 043118, doi:doi:http://dx.doi.org/10.1063/1.2838351 (2008).
20. Feng, A. L. *et al.* Distance-Dependent Plasmon-Enhanced Fluorescence of Upconversion Nanoparticles using Polyelectrolyte Multilayers as Tunable Spacers. *Scientific Reports* **5**, 7779, doi:10.1038/srep07779
21. Xu, W. *et al.* A novel strategy for improving upconversion luminescence of NaYF4:Yb, Er nanocrystals by coupling with hybrids of silver plasmon nanostructures and poly(methyl methacrylate) photonic crystals. *Nano Research* **6**, 795-807, doi:10.1007/s12274-013-0358-y (2013).
22. Wang, F., Deng, R. & Liu, X. Preparation of core-shell NaGdF4 nanoparticles doped with luminescent lanthanide ions to be used as upconversion-based probes. *Nature Protocols* **9**, 1634, doi:10.1038/nprot.2014.111 (2014).
23. Li, X., Wang, R., Zhang, F., & Zhao, D. Engineering homogeneous doping in single nanoparticle to enhance upconversion efficiency. *Nano Letters*, *14*(6), 3634 - 3639. doi: 10.1021/nl501366x (2014).
24. Hashimoto, Y., Seniutinas, G., Balčytis, A., Juodkazis, S. & Nishijima, Y. Au-Ag-Cu nano-alloys: tailoring of permittivity. *Scientific Reports* **6**, 25010, doi:10.1038/srep25010

25. Wahl, M., Rahn, H.-J., Gregor, I., Erdmann, R. & Enderlein, J. Dead-time optimized time-correlated photon counting instrument with synchronized, independent timing channels. *Review of Scientific Instruments* **78**, 033106, doi:doi:http://dx.doi.org/10.1063/1.2715948 (2007).

26. Chen, G. *et al.* Tip-Enhanced Upconversion Luminescence in Yb3+–Er3+ Codoped NaYF4 Nanocrystals. *The Journal of Physical Chemistry C* **119**, 22604-22610, doi:10.1021/acs.jpcc.5b04387 (2015).

27. Oskooi, A. F. AF Oskooi, D. Roundy, M. Ibanescu, P. Bermel, JD Joannopoulos, and SG Johnson, Comput. Phys. Commun. 181, 687 (2010). *Comput. Phys. Commun.* **181**, 687 (2010).

28. Centeno, A., Xie, F. & Alford, N. Predicting the fluorescent enhancement rate by gold and silver nanospheres using finite-difference time-domain analysis. *IET nanobiotechnology* **7**, 50-58 (2013).

29. Wu, D. M., García-Etxarri, A., Salleo, A. & Dionne, J. A. Plasmon-Enhanced Upconversion. *The Journal of Physical Chemistry Letters* **5**, 4020-4031, doi:10.1021/jz5019042 (2014).

30. Camposeo, A. *et al.* Metal-enhanced near-infrared fluorescence by micropatterned gold nanocages. *ACS nano* **9**, 10047-10054 (2015).

31. Abadeer, N. S., Brennan, M. R., Wilson, W. L. & Murphy, C. J. Distance and plasmon wavelength dependent fluorescence of molecules bound to silica-coated gold nanorods. *ACS nano* **8**, 8392-8406 (2014).

32. Chen, G., Qiu, H., Prasad, P. N. & Chen, X. Upconversion nanoparticles: design, nanochemistry, and applications in theranostics. *Chemical reviews* **114**, 5161-5214 (2014).

33. Oskooi, A. F. AF Oskooi, D. Roundy, M. Ibanescu, P. Bermel, JD Joannopoulos, and SG Johnson, Comput. Phys. Commun. 181, 687 (2010). *Comput. Phys. Commun.* **181**, 687 (2010).

34. Centeno, A., Xie, F. & Alford, N. Predicting the fluorescent enhancement rate by gold and silver nanospheres using finite-difference time-domain analysis. *IET nanobiotechnology* **7**, 50-58 (2013).

Chapter 5 Upconversion Nanoparticles $NaYF_4$ Enhanced by Plasmonic Nanostructures

5.1 Introduction

The control and manipulation of light is a classical research field and a fundamental topic for many scientific and technological advances. Currently, the key is focus on the near-field effects at nanoscale, which includes the light scattering by metal nanostructures. In chapter 4, we introduced a novel 3D mesoporous Au substrate, and studied its UCPL enhancement for upconversion nanoparticles. However, for $NaYF_4$ nanoparticles, previous reported enhancement factors were often limited. For example, 41 times in the case of mesoporous Au film in our previous work by mesoporous Au film substrate. There are several limitations that influence the enhancement effect: first, the spectral mismatch between the plasmon resonance and the excitation light. Second, the unoptimized design of the plasmonic substrate, and thirdly, the geometrical arrangement of the UCNPs and plasmonic substrate, in some situation quenching effect will be caused by the Au nanostructures. Besides pursuing significant enhancement factor, plasmonic substrates with large area and reproducible are also important. To tackle these issues, a novel nanosphere lithography technique was employed to fabricate plasmonic substrates, with large area and reproducibility. Nanoscale structures that have features below the resolution of optical diffraction limit can be made in the laboratory. Localized surface plasmon resonance (LSPR) is one unique property that can only be observed in nanoscale structure and have never been observed in bulk. The optical properties such as reflection and transmission deviate from the peculiar interaction of light with the change of materials and geometries. Significantly, the LSPR effect could also enhance the EM field in a specific area of the structure. LSPR is sensitive to the geometries of nanostructures and the neighboring materials. Three key geometry parameters are: size, shape, and the separation distance between the nanoparticles and nanostructures.[10] In designing such experiments, tuning of the LSPR frequency and control of the

distance between the metal and upconversion nanoparticles are two major issues. We focused on exploring the best plasmonic candidate by applying UCNPs@SiO_2 to a set of Au plasmonic nanostructures. A maximum 360 times UCPL enhancement was achieved by our plasmonic substrate, with the maximum absorption and emission bands of UCNPs overlapping with Au surface plasmon resonance. These results pave the way to understand the mechanisms of upconversion PL enhancement.

5.2 Experimental Methods

5.2.1 Fabrication the substrates of periodic polystyrene monolayer

In this chapter, a large area and low-cost technique, nanosphere lithography is NSL technique was applied based on the work of Xie et al.[1] Nanosphere lithography (NSL), also known as colloidal lithography,[2] is basically a patterning method using spherical nanoparticles such as polystyrene and silica as mask. Similar to other self-assembly methods, one major challenge in NSL technique is the formation of defects in fabricated samples. These defects include aggregation, voids between the monolayer areas, grains of monolayer, dislocation, etc. To improve the quality of nanoarrays, the reproducibility of nanosphere mask is important. The fabrication processes of plasmonic arrays substrate demands high standards criteria, to ensure repeatable good quality substrates and precise control over nanostructure geometrical parameters. In NSL process, the mask nanoparticles self-assembled onto clean substrates to form close-packed hexagonal pattern. This technique can be easily modified and combined with other nanofabrication techniques and can be done without any expensive equipment and chemicals. All reagents were of analytical grade. Ethanol absolute (VWR International, ≥99.7%), acetone (VWR International, ≥99.7%), isopropanol alcohol (VWR International, ≥99.5%), polystyrene (PS) suspension with a diameter of 300 nm, 500 nm, 620 nm, 800 nm (Bangs Laboratories Inc., USA.), and super premium glass microscope slides (VWR International) were used as supplied. In brief, monodisperse polystyrene (PS) nanoparticles

with a diameter of 500 nm (300 nm or 620 nm in other cases) were mixed with the same amount of ethanol separately. Approximately 9 to 12 μL of the mixed solution was spread homogeneously onto the surface of a clean silicon wafer (~50 mm ×50 mm), which had previously been exposed to UV-Ozone for 35 minutes. Afterwards, the silicon wafer covered by a single layer of polystyrene was then steadily and slowly immersed in a polypropylene vessel filled with 300 mL of DI-water, in order to allow the polystyrene nanoparticles forming an ordered monolayer on the air-water interface. To improve the uniformity of PS array, the water surface tension was modified by adding additional 3 μL of 2% sodium deodecyl sulfate solution. These processes were repeated 3 times in order to obtain a large are (4×4 cm^2) PS monolayer with highly ordered area. Finally, this PS monolayer was transferred to the cleaned glass substrate or Au surface (50 nm Au layer deposited on a cleaned glass substrate by a 'lift-off' technique. The type of PS monolayer deposited on substrates were obtained by repeating above procedures several times as needed. Afterwards, all types of plasmonic nanostructure substrates were prepared, three above-mentioned PS monolayer @glass substrates were treated by 0s - 30s of O_2 plasma etching.

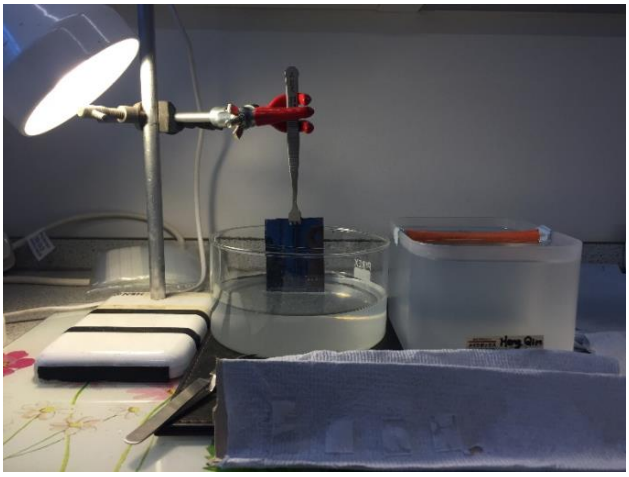

Figure 5- 1 Experimental set-up for transferring a polystyrene monolayer on the silicon transfer substrate.

5.2.2 Polystyrene Sphere Reduction by Oxygen Plasma

Nanosphere lithography has been conducted to obtain large area and highly reproducible PS monolayer mask. Initially, 2D hexagonal close pack arrays (Figure 5-2 (a)) are formed on a surface by self-assembly of these spherical polystyrene nanoparticles. It is important to have good control over the nanostructure geometries to produce repeatable plasmonic arrays. Oxygen plasma provide an easy way to modify the PS size, allows more plasmonic nanostructures can be produced. Then, metal can be deposited through the interstices of the nanoarrays. In addition, other shapes such as nanoholes can be fabricated by exposing the polystyrene nanoparticles to oxygen plasma.[3]

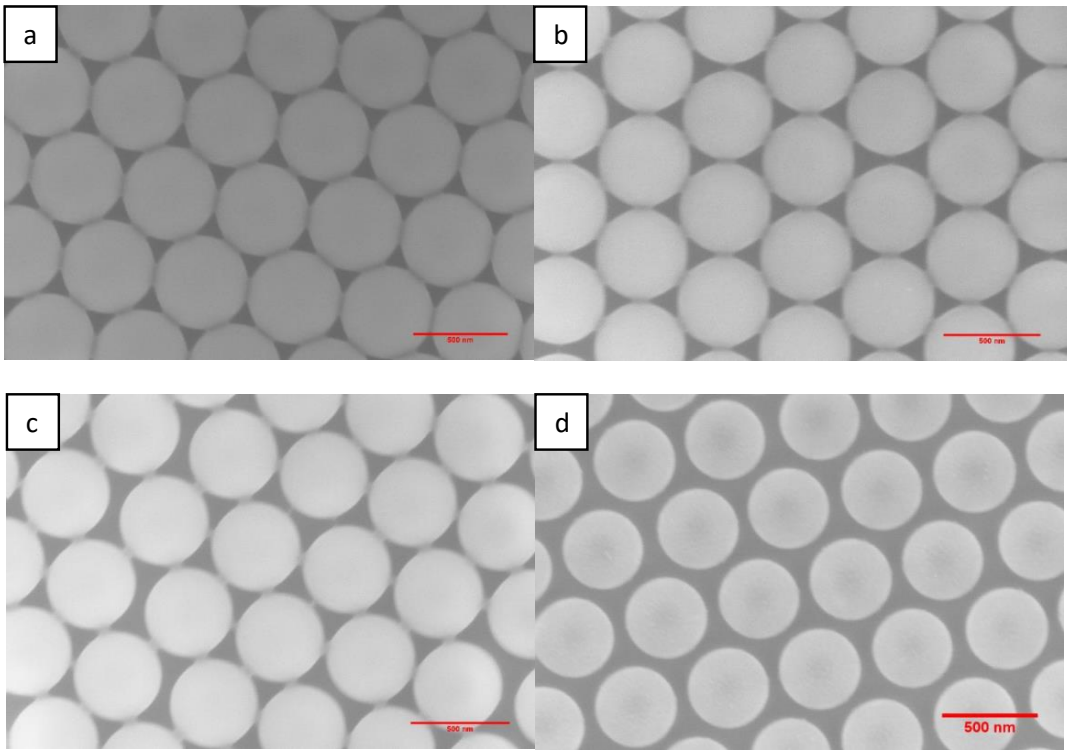

Figure 5- 2 SEM images of 500 nm polystyrene reduced by oxygen plasma time for 0s, 5s, 10s and 30s, respectively. These figures show the systematic reduction of the PS size as the exposure time of oxygen plasma increased.

The average size of polystyrenes and the distance between each polystyrene sphere can be precisely controlled. Specifically, exposure of polystyrene polymer to oxygen plasma could lead to the breakage of polymer backbone, side chain scissioning and depolymerization of polystyrene.[4,5] The center-to-center distance of PS is determined by initial PS size and remained unchanged after oxygen plasma process. The size reduction rate by oxygen plasma is a function of the exposure time, plasma power, accelerating voltage and pressure. Figure 5-2 (a-d) illustrate the PS size with respect to the exposure time of oxygen plasma for different initial PS sizes under 20sccm oxygen flow rate, 100 W plasma power and 200 V accelerating voltage in a Sentech Etchlab 200 system.

5.2.3 Metal deposition

In this project, full coverage, high uniformity and low roughness thin Au film was deposited through magnetron sputtering in a Mantis deposition system in Thin Film Lab of Imperial College London. It is a custom made PVD chamber for magnetron sputtering and thermal evaporation of metals. This system offers UHV (ultrahigh vacuum) performance for PVD researchers utilizing a conflat flange chamber. It allows true UHV to be achieved while allowing excellent chamber access through the large top-flange. Base ports are confocal as standard allowing a wider variety and number of deposition sources to be employed than with non-confocal arrangements. The stage is rotatable and is designed to allow heating up to 500 C or cool down by liquid nitrogen. After obtaining the high-quality PS nanoparticles array mask, the as-prepared substrates were transferred into the vacuum chamber, 50 nm Au were deposited on the PS monolayer by magnetron sputtering in the mantis deposition system (with 2 KeV HV voltage, 120 W filament power and about 1nm/min deposition rate). Afterwards, the PS mask along with residue Au was removed by an adhesive tape; then the substrates were dipped in ultrasonic bath for 1 min to clean residues. Finally, the dried substrates could be ready for scanning electron microscopy (SEM) characterization (Figure 5-3). To obtain sample with good quality, well-packed polystyrene is an essential requirement.

The mask quality can be easily observed after the deposition of metal. The maximum metal deposition thickness should be less than half of the PS diameter, otherwise the PS will be very hard to remove.

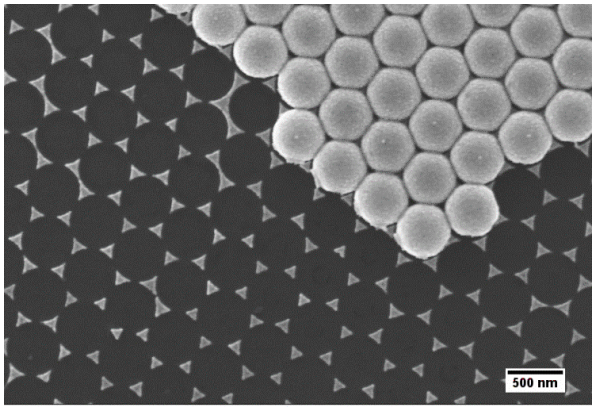

Figure 5- 3 shows the removing of PS500 nm mask sample by adhesive tape, which was deposited with 50 nm Au. It is clear that part of the substrate is still covered by polystyrene nanoparticles, while the rest of the image is Au nanotriangle array.

5.2.4 Experimental design for synthesis of $NaYF_4$ precursor

The prerequisite for obtaining $NaYF_4@SiO_2$ core-shell structure is to synthesize high-quality $NaYF_4$ core first. Similar to the $NaYF_4$ synthesis method in chapter 4, we applied a robust synthesis of lanthanide-doped $NaYF_4$ nanoparticles named co-precipitation method.[6] The $NaYF_4$ nanoparticles are prepared by co-precipitation of the lanthanide acetate salts with long-chain hydrocarbons (1-octadecene) and unsaturated fatty acids (oleic acid). The unsaturated fatty acid is used as the surface ligand to control particle growth and subsequently stabilize the resultant nanoparticles against agglomeration. In this synthesis process, the initial nucleation and following growth of the $NaYF_4$ nanoparticles are carried out in two steps, one at low 50 C and one at elevated 290 C, respectively. By tuning the composition of the lanthanide-oleate precursor, concentration of lanthanide ions can be determined accordingly. In detail, an inorganic source of lanthanide acetate salts is first transferred into a flask containing 1-octadecene and

oleic acid. The mixture is then heated to 150 C to obtain lanthanide-oleate coordination complexes. The nucleation and growth of the $NaYF_4$ nanocrystals are triggered by the injection of a methanol solution of NaOH and NH_4F. The combined use of NaOH and NH_4F enables a finer control over the reaction rate than using NaF alone. In addition, it can minimize corrosion of the glass flask. Since most of lanthanide reagents in the synthesis process are hydroscopic chemicals, which means they readily absorb water from their surrounding atmosphere, hydration of the lanthanide reagents must be avoided to guarantee the stoichiometry stability. Moreover, all chemicals are prepared in dilute stock solutions before the synthesis process, in order to precisely control the dosage. The final product of UCNPs have good photochemical stability, and they can work well under stringent conditions such as high temperature and low PH value.

5.2.5 SiO_2 coating of $NaYF_4$

Silica coating was applied to improve the water solubility of lanthanide-based UCNPs through modification of the Ln-UCNP surface. Besides, the separation distance of core UCNPs and Au nanostructure surface can be controlled by tuning the thickness of SiO_2 shell. A two-step reaction[7] is applied to get the core-shell nanostructure, in which the pre-synthesized core nanoparticles are used as the template for growth of the shell layer. Different to previous procedure, the pre-synthesized UCNPs are added to the solution before the injection of the $NaOH/NH_4F$ solution. The core particles play a role as foreign seeds that mediate epitaxial growth of the silica shell growth. Disperse Igepal CO-520 (0.2 ml) in cyclohexane (8.0 ml) by sonication in an Erlenmeyer flask. Add OA-capped Ln-UCNPs dispersed in cyclohexane (4.0 ml, 10.0 mg ml^{-1}) into the solution. The resulting mixture was stirred vigorously until the solution becomes transparent. Add ammonium hydroxide (29.4% wt/wt, 80 μL) into the mixture; stir the mixture vigorously to form a transparent microemulsion. Since ammonium hydroxide is toxic and corrosive, appropriate protection must be applied. Then add TEOS (40 μL) to the mixture，keep stirring

the mixture gently for 48 h at room temperature. Afterwards, precipitate the resulting nanocomposites by the addition of acetone (20 ml), and then collect the precipitates by centrifugation 10000 r.p.m. for 10 min. Then re-disperse the collected nanocomposites in ethanol and purify them by sonication and centrifugation. Finally, re-disperse the collected SiO_2-modifid Ln-UCNPs in ddH_2O to a concentration of 1.0 mg ml^{-1}, store the resulting samples at 4℃. Then we can proceed to the characterization of the SiO_2 modified Ln-UCNPs. Dilute the UCNPs@SiO_2 aqueous dispersion (1.0 mg ml^{-1}) to 0.1 mg ml^{-1} with water, and then deposit the sample onto a carbon-coated copper TEM grid. Dry the samples naturally at room temperature for 36 h. The sample can be characterized by JEOL JEM 2100 transmission electron microscope at an accelerating voltage of 200 kV.

5.3 Result and discussions

5.3.1 Properties of Au nanostructures

Nanosphere lithography is a versatile and low-cost technique to develop large area nanostructure based on hexagonal close packed arrangement. Two types of plasmonic nanostructures were produced in this section, nanotriangle arrays and nanohole arrays. These substrates were characterized by SEM Leo 15 to investigate the morphologies and geometrical properties. Nanotriangle array samples (Figure 5-1, a-c) are basic nanostructures to be fabricated by nanosphere lithography technique. Due to high curvature at the nanotriangle tips, the surrounding electric field will be much enhanced as a result of localized surface plasmonic resonance (LSPR).[8,9] These SEM demonstrated the tip to tip distance of Au nanotriangles are getting closer with the extension of oxygen plasma treatment time for polystyrenes. By selecting and combining different polystyrene sizes, different metal thickness, and various exposure time to oxygen plasma, these geometry parameters can be precisely tuned. These properties benefit for them to be applied in the field of UCPL enhancement.

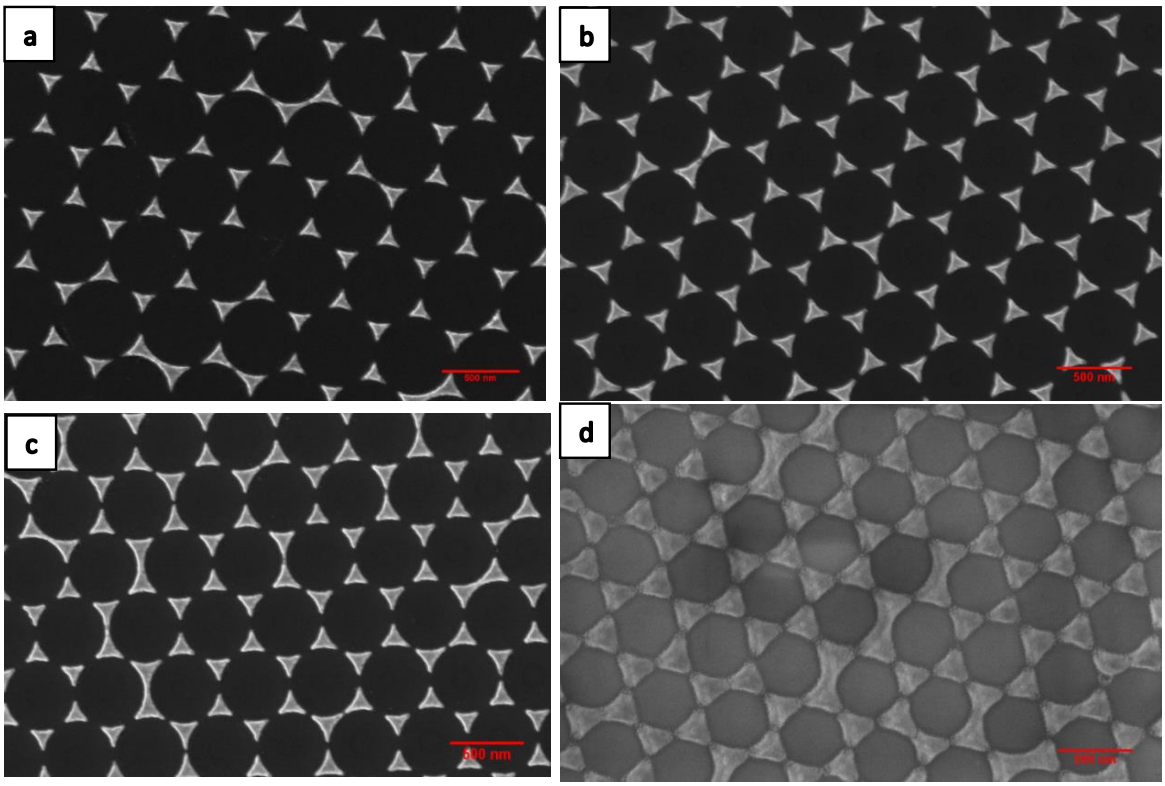

Figure 5- 4 (a-c) 500 nm polystyrene, treated by oxygen plasma (OxP) for 0s, 5s, 10s, with 50 nm thickness Au deposited on the silicon substrates. (d) 500 nm polystyrene treated by oxygen plasma (OxP) for 15s with 50 nm thickness Au deposited on the glass substrate.

As shown in Figure 5-4，closely spaced nanotriangular arrays has a long side length and a relatively shorter perpendicular bisector length. The difference between these two lengths is about 13%. The lateral dimensions of the nanotriangle are dependent on the size of polystyrene used. The tip-to-tip distance between the nanotriangles can be reduced by extending the duration time of oxygen plasma treatment. Since plasmonic resonance is sensitive to the geometry, the change of geometrical parameters can induce different plasmon resonance peaks. Nanoparticle structural parameters are listed in Table 5-1. To facilitate the comparison and differentiating samples in the figure, we adopt a labelling system in the following rule.

PS (size)-Oxygen plasma treatment time-thickness of the Au film (height). For instance, PS 500 nm-OxP 10s-50 nm describes nanotriangle arrays fabricated with 500 nm diameter polystyrene as mask and with 10s oxygen plasma treatment, and then deposited with 50 nm Au.

5.3.2 Optical properties

Optical characterizations have been performed to study the geometry dependent LSPR resonance. Materials, thickness, interparticle distance, lateral size were demonstrated to influence the plasmonic resonance position. UV-VIS spectroscopy Agilent Cary 5000 system was used to characterize the optical properties of the Au nanostructure samples with unpolarized light. The samples were placed in the UV-VIS spectrometer facing the incident light, while clean glass substrate was used to correct the baseline of the spectrometer. For these samples, same glass slides are used as substrates for all samples in this case.

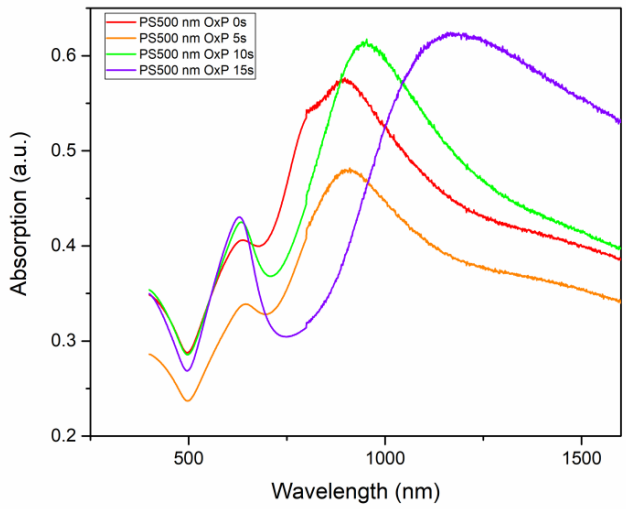

Figure 5- 5 Absorption spectra for Au 50 nm thickness nanotriangle array with different OxP time (0s, 5s, 10s, 15s). The d to s inter-band transitions of Au are around 650 nm and blue-shifted with longer OxP

time. The absorption peaks within 900 nm to 1200 nm can be attributed to the excitation of strongly localized surface plasmon (LSPR dipole),[11,12] these peaks red-shifted with longer OxP time.

Figure 5-5 shows the absorption spectra of nanotriangle array substrates fabricated with PS 500 nm treated by 0s, 5s, 10s and 15s, respectively. It is important to precisely control the shape of nanostructures in nanometers regime. Their LSPR peak positions according to geometrical parameters are summarized in table 5-1. These LSPR data can be regarded as reference for the selection of geometrical parameters in further applications. The plasmon peak widths are determined by damping/decay of the plasmon excitation, which is inversely related to the lifetime of plasmon excitation (if inhomogeneous broadening can be excluded).[13]

Table 5- 1 Nanoparticle structural parameters corresponding to the Near- and Mid-Infrared Excitation. s is the measured tip-to-tip distance, D is the size of the PS used, λ_{meas} is the measured extinction peak wavelength.

Sample	PS500-0s	PS500-5s	PS500-10s	PS500 15s
s (nm)	135±16	115±16	60±4	40±8
D (nm)	500	500	500	500
λ_{meas} (nm)	880	890	980	1100

The optical properties of plasmonic nanostructures is sensitive to the geometry. In the case of nanotriangle array, another key parameter is the tip to tip distance of the nanotriangle particles. It can be observed that the shift of extinction profile of Au nanotriangle samples as a function of different tip to tip distance. When the tips of nanotriangle get closer, the LSPR resonance changed accordingly as a result of coupling effect.[14] From the table above, PS nanospheres with 500 nm were chosen, each of them was then exposed to a short duration of oxygen plasma treatment and followed by deposition of 50 nm of Au, respectively.

After the removal of PS masks, closely packed nanotriangle arrays were formed. With longer oxygen plasma exposure duration, the tip to tip distance between the Au nanotriangles were reduced. The resonance peak also changed in response to the geometry modifications as a result of changed coupling between the adjacent nanotriangles. It has been well studied that the LSPR resonance is quite sensitive to the dielectric function of the materials. Governed by LSPR resonance condition $\epsilon_{i,1}(\lambda) = -\chi\epsilon_m$, the resonance peak of different metal with same geometry parameters ranges from UV, covers visible and up to NIR.[15] Since Au has relatively low $\epsilon_{i,1}(\lambda)$ value, the interband transition is around 650 nm and goes up to NIR-II region.

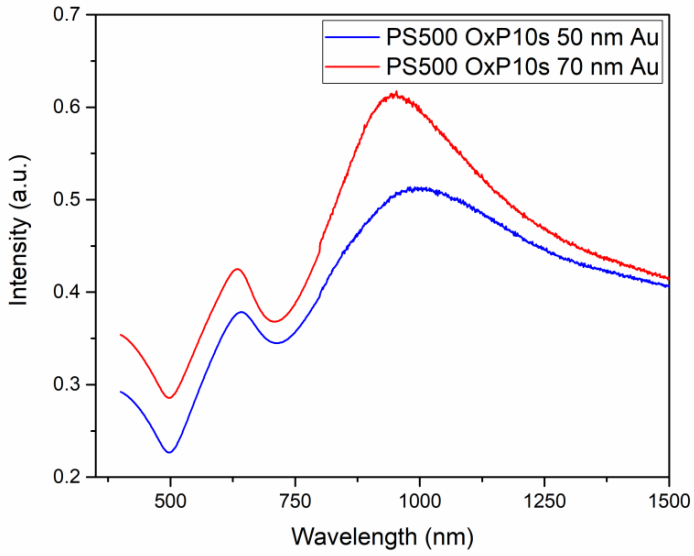

Figure 5- 6 Absorption spectra for Au nanotriangle array with 50 nm and 70 nm thickness, respectively.

From figure 5-6 and table 5-1, the LSPR resonance peaks demonstrated blue-shifting as the thickness of Au increased from 50 nm to 70 nm. This phenomenon is due to increased phase retardation.[16] When reading the plasmonic resonance spectra, it is necessary to distinguish the dipole resonance and other

modes, such as some secondary effects related to geometry defects. However, when conducting the optical measurements, the acquisition area for the sample covers around a spot size of 5 mm, which contains approximately 16 k nanotriangle array units. This large area makes it hard to distinguish the plasmonic resonance from the secondary effects characteristic peaks.

Table 5- 2 Plasmonic peak location for nanotriangular arrays of PS 500 nm etched by 10s oxygen plasma with 50 nm and 70 nm thickness, respectively.

Thickness	Metal	Dipole (nm)	Quadrupole (nm)
50 nm	Au	900	630
70 nm	Au	1000	640

Figure 5-7 (a) is the SEM image of Au nanohole arrays with thickness of 50 nm. Hexagonal nanohole array can be fabricated in the similar NSL technique as nanotriangle array. The major difference between nanohole arrays and nanotriangle arrays is that the PS size has been further reduced, until the tip to tip of nanotriangle nanoparticles touched each other. The reduction of 500 nm polystyrene by oxygen plasma for 0s, 5s, 10s, 30s are shown in Figure 5-2.

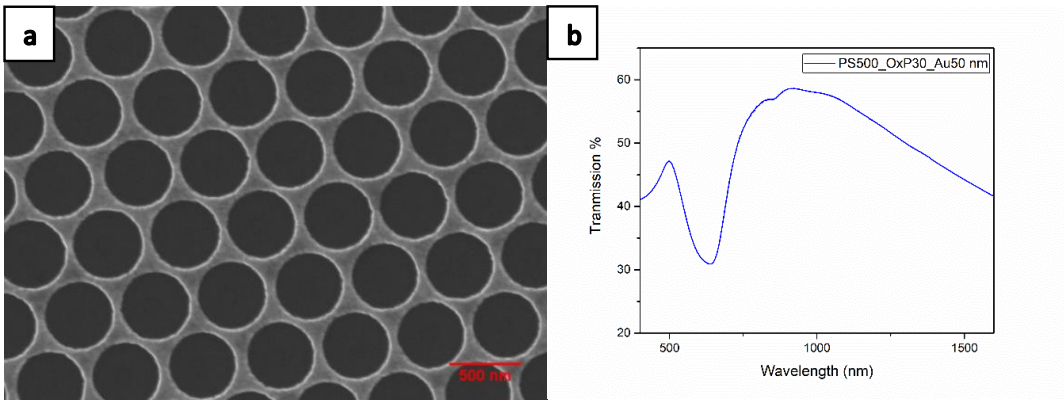

Figure 5- 7 (a) SEM image of Au nanohole arrays (OxP 30s) with Au thickness of 50 nm. (b)Transmission spectra for Au 50 nm thickness Nanohole Array with different OxP time for 30s. Note: The prolonged

oxygen plasma time modified the tip distance of the nanotriangle arrays, and the structure evolved to be nanohole array when oxygen plasma time reached 30s.

In nanohole arrays where the diameter of holes is small compared to the thickness of the metallic film, the plasmonic resonance can be best regarded as excitation of surface plasmon polaritons (SPPs) at the dielectric-metal interface by the incident electromagnetic wave.[17,18] Figure 5-7(b) shows the extraordinary optical transmission (EOT) that related to SPP mode of Au nanohole array substrates that fabricated via NSL approach. Similar to the optical properties of nanotriangle array samples, the transmission spectrum of nanohole arrays samples is also determined by the materials, and geometrical parameter such as metal thickness and nanohole diameter. In the case of Au sample, one minimum and one maximum peak are observed. The transmission peak at 500 nm is caused by the interband transition, while the transmission peak at 930 nm is due to the plasmonic resonance of the entire structure (the excitation of a surface plasmon polariton mode (SPP))[19,20] The SPPs are generated when the nearest neighbor distance in the case of short-range order particle ensembles matches the SPP wavelength. In the case of an ideal metal, the SPP only depends on the holes' nearest neighbor distance but not on the holes' size/geometry. The broad resonances measured in the figure can be attributed to damping by electron scattering from the Au grains in the sample.

5.3.3 UCPL enhancement by plasmonic effect

As discussed in chapter 3, rare earth-doped upconversion processes are realized by using continuous-wave (CW) lasers, excited in the NIR range (usually 980 nm), and with a tunable emission across the UV visible and NIR in accordance with the selection of doping lanthanide ions. Lanthanide-doped upconversion nanocrystals possess outstanding chemical and optical properties, e.g. large effective Stokes shift, sharp emission bands, high resistance to photobleaching and photochemical degradation.[21]

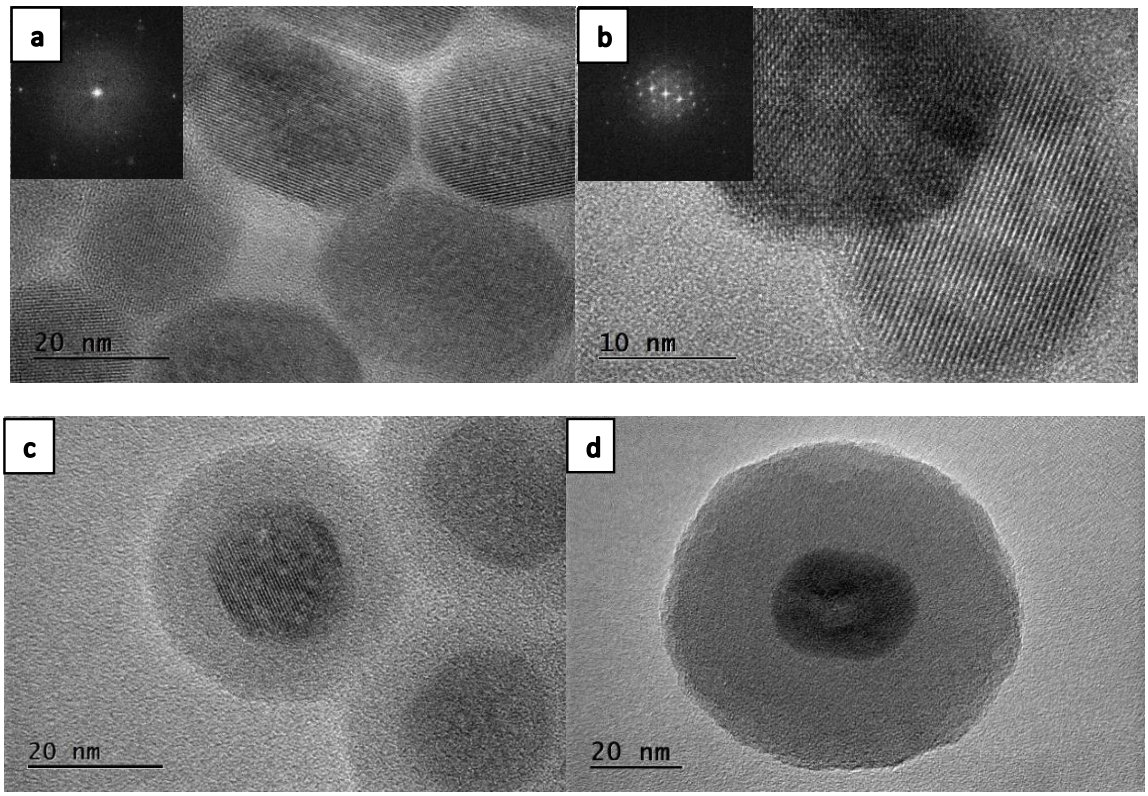

Figure 5- 8 TEM images of nanoparticles figure 5-8 (a), and $NaYF_4/SiO_2$ core shell with 2 nm (figure 5-8 (b)), 10 nm (figure 5-8 (c)), 23 nm (figure 5-8 (d)) silica shells, respectively.

We have demonstrated that different doping concentration of lanthanide ions can be used to fine tune the $NaYF_4$ nanoparticles, modifying the ion-ion interaction, and as a result, have a good control over the characteristics of optical emissions. These unique properties allow lanthanide-doped upconversion nanoparticles to be very useful in solar energy conversion and photodynamic therapy.[22,23] However, the practical applications of upconversion nanoparticles are still hindered by the poor upconversion quantum efficiency. In the following part, the upconversion photoluminescence (UCPL) enhancement by various Au nanostructure substrates are explored. Au substrates with different geometries were applied to UCNPs@SiO_2. We first demonstrate the TEM images of UCNPs@ SiO_2 with different SiO_2 thicknesses,

followed by the element mapping of UCNPs@SiO_2. The UCNPs used in the experiments are spherical in shape and monodisperse in size.

In this study, hexagonal phase β-$NaYF_4$:20% Yb^{3+}, 2% Er^{3+} nanoparticles used were same to Chapter 4. As shown in the transmission electron micrograph (TEM) in Figure 5-8(a), the nanoparticles were hexagonal in shape and with mean vertical length of 36.1 nm (standard deviation of σ = 4.06 nm, for n=100 nanoparticles), with a lateral length of 25.5 nm (standard deviation of σ = 1.4 nm, for n=100 nanoparticles). However, we further coated the surface of UCNPs by silica shells with different thicknesses, 2 nm, 10 nm and 23 nm, respectively. This varying thickness determines the distance between the UCNPs and Au nanostructures, which can influence the effect of plasmonic enhancement.

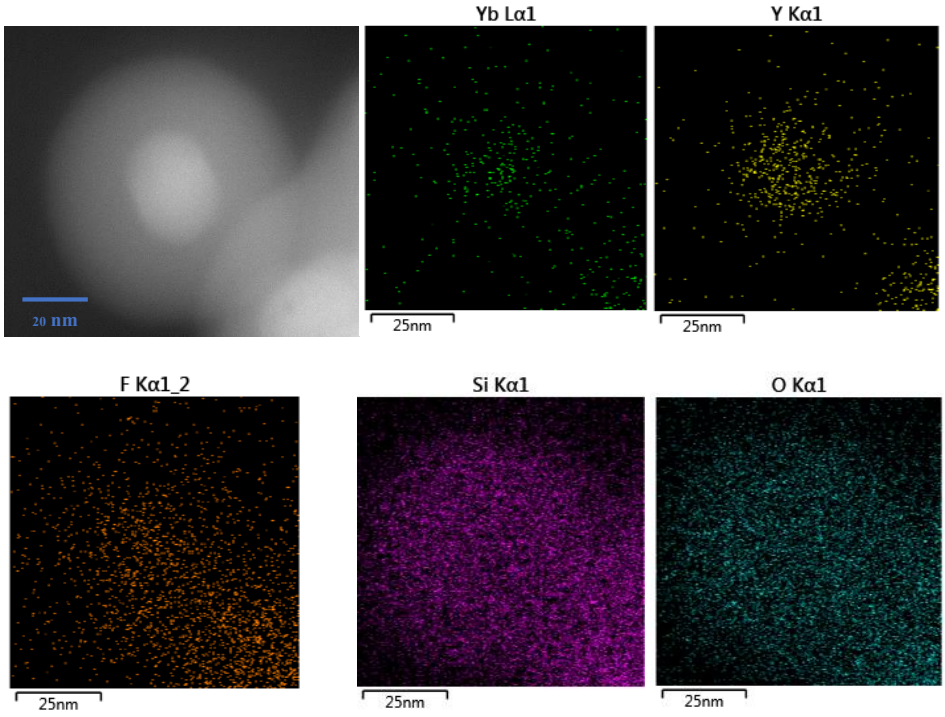

Figure 5- 9 HRTEM images of 320 C Co-precipitation method synthesized UCNPs Core $NaYF_4$:Yb^{3+}, Er^{3+} and the element mapping of Yb, Y, F, Si and O respectively.

We further characterized UCNP@SiO_2 by element mapping technique. The HRTEM shows that the SiO_2 shell is about 20 nm in thickness. And the element mapping demonstrated the existence of Yb, Y, F, Si and O elements in the $NaYF_4$@SiO_2 core-shell nanoparticles. The distribution of Si and O elements demonstrate that this UCNP was well coated by SiO_2. The distribution of Yb, Y and F elements indicate the core is $NaYF_4$ doped with Yb^{3+} ions. The missing of Er element map was due to the low concentration of Er and the sensitivity of the detector. Next, we modified the surface property of $NaYF_4$@SiO_2 to improve the distribution of $NaYF_4$@SiO_2 on Au substrates. To optimize the plasmonic enhancement effect, the control of surface distribution of UCNPs@ SiO_2 on the Au nanostructures are also important factors. We modify the $NaYF_4$@SiO_2 by ligand exchange method with MPTMS to make $NaYF_4$@SiO_2 uniformly attached to the surface of Au nanotriangles. The degree of surface coverage of Au substrate mainly depends on the effectiveness of MPTMS and on the concentration of $NaYF_4$@SiO_2 used for drop-casting. The concentration of the solution is selected to guarantee there are suitable quantity UCNPs@SiO_2 nanoparticles to form a sub-monolayer on the surface of plasmonic substrate. Before drop casting the $NaYF_4$@SiO_2, we sonicated the suspension of $NaYF_4$@SiO_2 in DI water to avoid clustering or agglomeration. It is also important to consider distribution and number density of UCNPs@SiO_2 on reference sample. Since the surface properties of bare glass and Au are different, even when depositing same amount of UCNPs@SiO_2 solution, the number of UCNPs@SiO_2 nanoparticles attached on different type of surface are quite different. This difference is required to be corrected by calculating the number density from SEM images. Figure 5-10 (a) and (b) show the SEM images of MPTMS modified UCNPS@10nm SiO_2 of different amount attached on Au nanotriangle arrays.

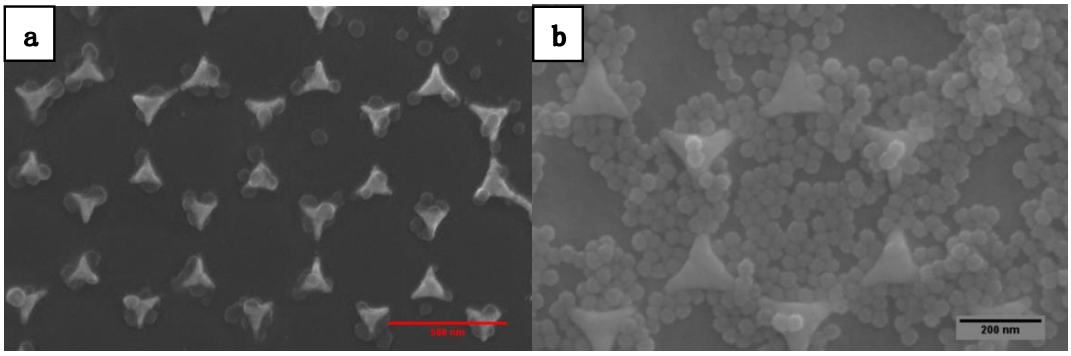

Figure 5- 10 UCNPS@10nm SiO_2 attached on Au nanotriangle array fabricated by polystyrene size 500 nm oxygen plasma time for 0s, with 50nm thickness Au deposited on the substrates. Figure 5-10 (a) is substrate deposited with 3 mmol/mL concentration of UCNPS@10nm SiO_2, while Figure 5-10 (b) is deposited with 5 times amount of UCNPS@10nm SiO_2 on substrate with same area. The difference between two figures demonstrated that the coverage of plasmonic substrates can be controlled by tuning the concentration and quantity of UCNPS@10nm SiO_2 solution.

For the purpose of making quantitative comparison, the UCPL enhancement is corrected to the same number of UCNPs@SiO_2 in a certain area of the plasmonic substrate and clean glass, respectively. Figure 5-10(a) was adopted as the UCNPs@SiO_2 distribution standard for the PL measurement. Accordingly, 0.05 mL of 3 mmol/mL of UCNPS@10nm SiO_2 was used to deposit on each sample. It can be estimated that the number of UCNP@SiO_2 attached on each triangle nanostructure is about 3 to 5. Meanwhile, we deposited exactly the same quantity of UCNPS@10nm SiO_2 on benchmark sample (clean silicon substrate) in order to make reasonable comparisons.

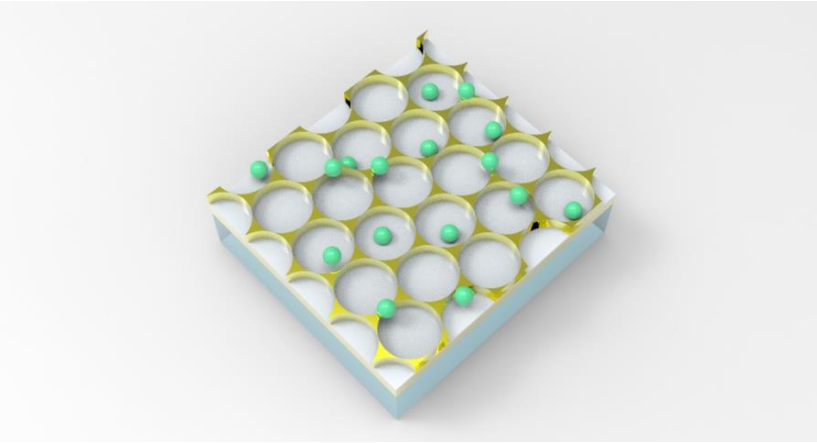

Figure 5- 11 3D schematic diagram shows the $NaYF_4$@SiO_2 deposited on flat Au/10nm SiO_2 layer/Au nanotriangle array substrate.

Figure 5-11 is the 3D schematic diagram of the plasmon-enhanced upconversion structure in this work. The structure was composed of five major components: (i) silicon substrate on the bottom, (ii) 50 nm flat gold (Au) film, (iii) 10 nm silica (SiO_2) spacer layer, and (iv) Au nanotriangle/nanohole array (v) β-$NaYF_4$:Yb^{3+}, Er^{3+} UCNPs sub-monolayer (green balls). Silicon substrate was used to support the whole system. The 10 nm silica spacer layer was used to separate the flat Au and Au nanostructure array, in order to maximize the coupling effect between these two structures. The plasmon resonance of Au nanostructures can be modified by changing the geometrical parameters.

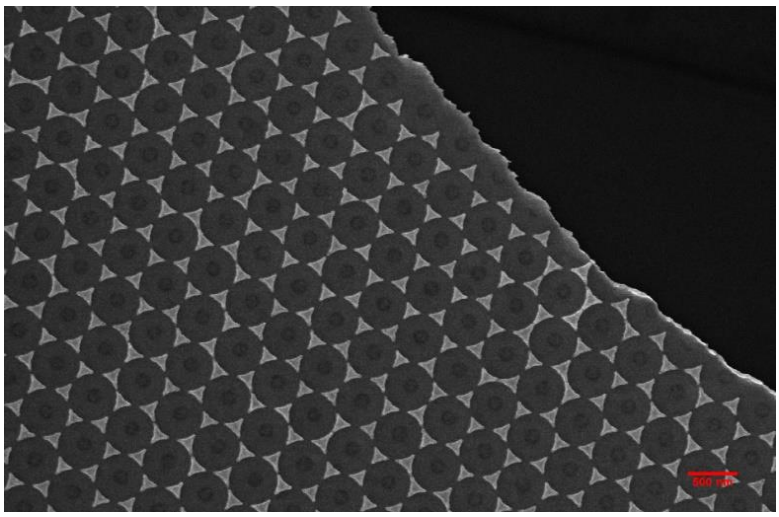

Figure 5- 12 SEM image of flat Au 50 nm/10nm SiO_2 spacer layer/PS500 nm-OxP 10s/Au nanotriangle array substrate. Au nanotriangle array fabricated by polystyrene size 500 nm, with oxygen plasma for 10s, with 50nm thickness Au deposited on SiO_2 as wafer with 10 nm between Au nanotriangle disk arrays and flat Au layer with thickness of 50 nm directly.

Figure 5-12 demonstrates the SEM image of flat Au 50 nm/10nm SiO_2 spacer layer/PS500 nm-OxP 10s/ Au nanotriangle array substrate, which also shows the edge of 50 nm flat Au. This structure was constructed according to schematic diagram presented in Figure 5-11, with a 50 nm Au layer underneath the Au nanotriangles and a 10 nm SiO_2 spacer layer in the middle of flat Au and Au nanostructure arrays. This 3D design aims to couple the LSPR mode and SPP mode, to achieve an enhancement effect that could not be obtained by each plasmonic mode alone. Similar to figure 5-10 (a), the $NaYF_4$@SiO_2 nanoparticles can be deposited near the tips of nanotriangle arrays, in order to realize higher enhancement factors. The PL emissions are measured by a Fluorolog system designed by Horiba Jobin Yvon, under the same excitation condition. We excited the nanocrystals at a power density of 4.13 W/cm^2. A minimum excitation power density of 1 W/cm^2 is suggested for the anticipated results below to be observed. The

sample holder allows a tunable angle of excitation on the flat substrate. To obtain consistency and comparable results, the angle of acquisitions was set to 45° in general cases.

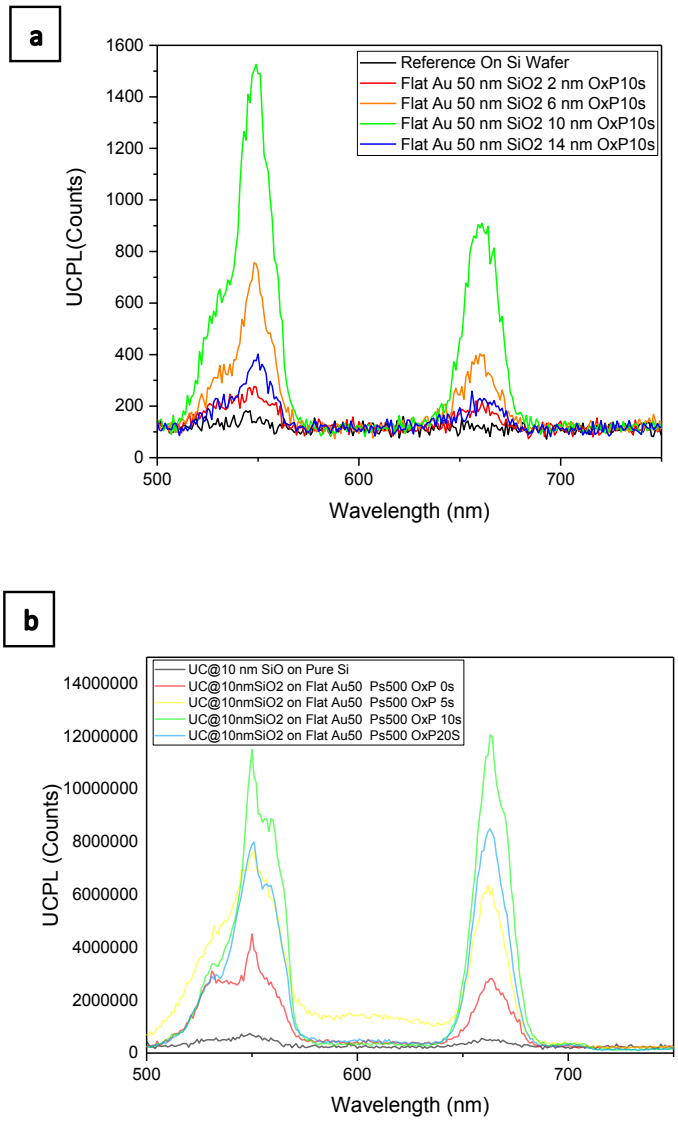

Figure 5- 13 (a) Enhancement factors exhibited as a function of different values (2nm, 6nm, 10nm, 14nm) of the spacing distance (the silica shell thicknesses of $NaYF_4$@SiO_2) deposited on flat Au/10nm SiO_2 layer/Au nanotriangle array, 500 nm polystyrene etched by oxygen plasma for 10s substrates. UCPL emissions demonstrated peaks around 541 nm and 656 nm, respectively. (b) Enhancement factors for

$NaYF_4$@10 nm SiO_2 deposited on flat Au/10 nm SiO_2 spacer/nanotriangle array, 500 nm polystyrene etched by different oxygen plasma etching time (0s, 5s, 10s, 20s), respectively.

To explore spacer distance dependent of plasmon-enhanced UCPL, a set of UCPL measurements by tuning the SiO_2 shell thickness of UCNPs@SiO_2 were conducted. We systematically modified the distance by synthesizing $NaYF_4$@SiO_2 with different thickness of silica layer, with 2 nm, 6nm, 10 nm and 20 nm (Figure 5-8), respectively. Experimental results (Figure 5-13(a)) confirmed that the UCPL reaches a maximum at 10 nm spacing distance. These $NaYF_4$@SiO_2 samples allows us to investigate the different regimes of interaction between Au substrate and $NaYF_4$ nanoparticles. The coupling between the UCNPs and Au changed as a function of spacing distance. Introduction of silica spacer layers of different thicknesses tested the optimal spacing to achieve the best metal induced enhancement. It has been proved that if UCNPs and Au are too closed to each other, quench effect will be dominated.[28,29] However, if UCNPs were placed at a certain distance from the plasmonic surface, energy transfer into the plasmon would be remarkably reduced but the electromagnetic field strength can still be great enough to enhance PL emission.[30,31] According to the result of Figure 13(a), samples with 10 nm silica spacer layers between 50 nm flat Au layer and 50 nm Au nanotriangle array layer were chosen in further comparisons.

To understand the mechanisms of spectral overlap effect, plasmonic substrates with various extinction profiles have been fabricated to be conjugated with same UCNPs@SiO_2. Figure 5-13 (b) shows UCPL measurements for samples with different duration of oxygen plasma treatment. The best enhancement factor can be seen at emission of 541 nm, up to about 360 times was achieved by $NaYF_4$@10 nm SiO_2 by flat Au 50 nm/10nm SiO_2 spacer layer/PS500 nm-OxP 10s/Au nanotriangle array substrate, compared to the emission from the reference sample (UCNPs deposited on clean glass). $NaYF_4$@10 nm SiO_2 deposited

on this substrate gives the best enhancement effect. However, with oxygen plasma treatments shorter or longer than 10s, much weaker UCPL enhancement factors were achieved.

Plasmon-enhanced UCPL is due to very different coupling mechanisms between the energy levels of the lanthanide ions (Yb, Er) and the surface plasmonic resonance modes of Au. The advances in control of optical energy in subwavelength nanostructures provides great opportunities for the improvement of upconversion photoluminescence. Especially, the coupling effect between localized surface plasmons generated by closely separated Au nanoparticles results in electromagnetic hot spots.[24.25] For example, periodic high electric spot formed near the surface of nanotriangle array substrate, which could be felt by the attached upconversion nanoparticles. These plasmonic nanostructures are ideal candidates to generate enhanced local electromagnetic field, especially at the locations of tips and corners.[26,27] Close proximity of Au nanostructures to UCNPs can cause UCPL enhancement by influencing both absorption in the near-infrared (980 nm) and emission in the visible range. As demonstrated in former part, the LSPR peak is highly rely on the geometrical parameters of the nanostructures. Since the LSPR band of Au nanotriangle/nanohole substrates are easily tuned from visible range to NIR range, they are good choices for studies of SPR/UCPL with different emission and absorption spectral overlap. Extinction spectra of a set of nanotriangle arrays substrates were presented in former section (Figure 5-5). However, in the case of substrates using 50 nm flat Au as the bottom layer, UV-Vis measurement cannot obtain the extinction spectra. FDTD method will be adopted to estimate the reflection, transmission and absorption spectra for flat Au 50 nm/10nm SiO_2 spacer layer/Au nanotriangle array substrates.

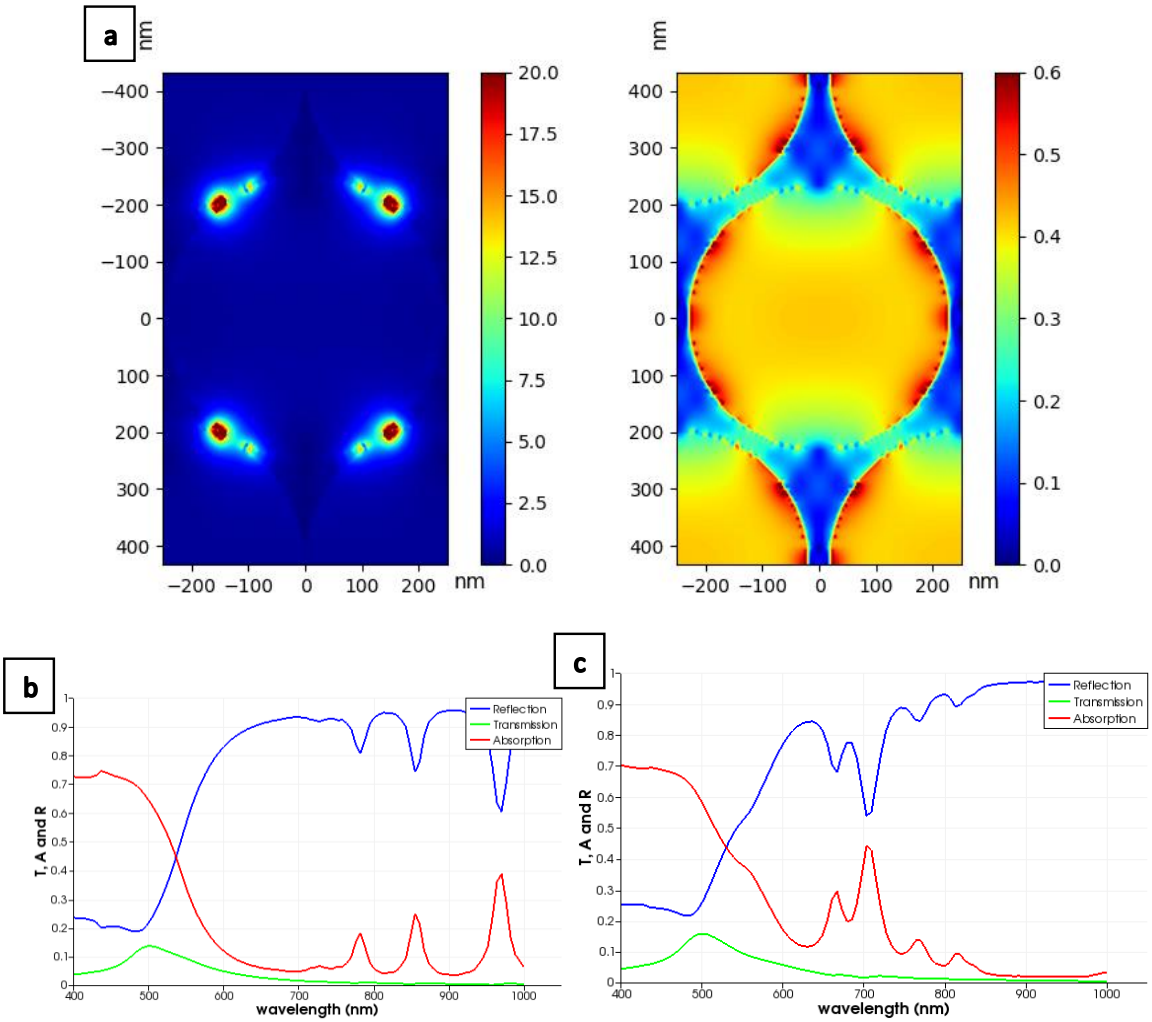

Figure 5- 14 (a) Electromagnetic field mapping of flat Au 50 nm/10nm SiO_2 spacer layer/Au nanotriangle array (OxP 10s) substrate and flat Au 50 nm/10nm SiO_2 spacer layer/Au nanohole array (OxP 30s) simulated by FDTD method. (b) The calculated reflection, transmission and absorption spectra for flat Au 50 nm/10nm SiO_2 spacer layer/Au nanotriangle array (OxP 10s) substrate. (c) The calculated reflection, transmission and absorption spectra for flat Au 50 nm/10nm SiO_2 spacer layer/Au nanohole array (OxP 30s).

To understand the complex EM field of these plasmonic nanostructures, simulations were performed with collaboration with Q. Jiang from Xie's group. The background absorption of the flat Au layer makes it difficult to measure the positions of surface plasmon resonance experimentally. However, the FDTD simulation demonstrated that these two structures exhibit very strong plasmonic resonance and significant electric field enhancement. The local electric field enhancement created by nanotriangle/nanohole deposited on flat Au were simulated. A 3-dimensional model was developed based on the SEM measurements. The electric field intensity was solved with a finite-difference time-domain (FDTD) method, with periodic boundary conditions in the lateral direction, and a plane wave normal to the substrates as the excitation source. As shown in Figure 5-14 (a), the electric field is strongly localized and the enhanced in the nanotriangles-backplane gaps due to the strong vertical coupling between them. The Au nanotriangles and Au backbone confine the light both vertically and laterally. The formed nanogaps at the edges between nanotriangles and flat Au and the gaps between the tips of two nanotriangles can collect and concentrate the light from external large space into the cavity, and hence create an extremely strong electric field with the small areas. Au nanohole/nanotriangle arrays deposited on flat Au substrates explored the combination of the LSPR and SPP modes to provide a greater UCPL enhancement. The significant UCPL enhancement origins from the strong resonant coupling of the Au nanogaps.

This localized field enhancement has demonstrated remarkable potential to increase the UCPL efficiency. Theoretically, if plasmonic bands demonstrate significant spectral overlap with the absorption/emission bands of UCNPs, a large resonant enhancement of UCPL is desired. Absorption enhancement is defined as the ratio of the absorption efficiency of the UCNPs in proximity to metal nanostructures to the absorption efficiency. The absorption enhancement is proportional to the square of the EM field enhancement. The emission enhancement (Purcell effect) exists since UCNPs and Au substrate are

resonant with the UCNPs' emissions and the Au change the local photon density of states. Basically, there are 3 different situations. First, excitation overlapping, which means the extinction peak matches the absorption band of UCNPs (absorption enhancement). Secondly, excitation and emission overlapping, in which case the extinction peaks match the absorption band and emission band of UCNPs simultaneously (absorption enhancement and emission enhancement). Thirdly, it is a case that neither the excitation band nor the emission band of UCNPs overlap with the extinction peak of plasmonic substrate. It is clear that the calculated reflection, transmission and absorption spectra for flat Au 50 nm/10nm SiO_2 spacer layer/Au nanotriangle array (OxP 10s) substrate exhibits a 980 nm absorption, which can provide the absorption overlap with $NaYF_4$:Yb^{3+}, Er^{3+} (Figure 5-14(b)). While Figure 5-14(c) shows that absorption spectra for flat Au 50 nm/10nm SiO_2 spacer layer/Au nanohole array does not match the 980 nm absorption of $NaYF_4$:Yb^{3+}, Er^{3+}. This could be one of the major reasons that flat Au 50 nm/10nm SiO_2 spacer layer/Au nanotriangle array (OxP 10s) substrate generated much higher enhancement effect. Considering the UCPL enhancement factors, these results demonstrated that the spectral overlap between SPR bands and emission/excitation of UCNPs are significant for UCPL enhancement factor. If we could manage to perform the lifetime measurements on the samples with both absorption and emissions spectral overlap, a decrease in decay times may be observed due to a metal-induced Purcell effect. However, due to limited amount of UCNPs@SiO_2 deposited on Au substrates and the moderate intensity of our pulsed laser, the weak emission signals were beyond the detection capability of our photodiode in the lab. Moreover, the SiO_2 shells have an obvious effect of block the photoluminescence of UCNPs. Therefore, lifetime measurements were not conducted in this experiment.

5.4 Conclusions

Nanolithography approach was applied to fabricate periodic Au nanostructure samples. We have systematically investigated the properties of Au nanotriangle array and nanohole array as a novel class of

plasmon-enhanced substrates for UCPL. Enhancement factors as a function of Au nanostructure and UCNP surface distance were measured, a maximum 360 times UCPL enhancement was achieved. These results suggest that Au nanohole/nanotriangle arrays on flat Au substrates are excellent candidates for UCPL enhancement. The novel and simple self-assembly, nanolithography and gold evaporation method for fabrication of nanotriangle array samples allows promising applications, include solar light harvesting, development of new photonic systems and so forth.

The work thus far has achieved great enhancement factor of rare-earth doped upconversion nanoparticles by the 3D Au nanostructures. Given these good experimental results, more valuable explorations could be there for practical applications in the solar energy field. There are two considerations to make further improvement: 1. Use Au nanostructure array to enhance upconversion nanomaterials with intrinsic higher upconversion efficiencies than rare-earth based upconversion nanoparticles, such as triplet-triplet annihilation upconversion nanoparticles (TTA-UCNPs). 2. To combine the advantages of plasmonic and upconversion mechanisms for the enhancement of photocatalytic performance of traditional semiconductor. In the next chapter, we will move on to study one practical application of this type of plasmonic substrate.

Reference

1. Pang, J. et al. Gold nanodisc arrays as near infrared metal-enhanced fluorescence platforms with tuneable enhancement factors. *Journal of Materials Chemistry C* 5, 917-925 (2017).
2. Xie, F. et al. Nanoscale control of Ag nanostructures for plasmonic fluorescence enhancement of near-infrared dyes. *Nano Research* 6, 496-510 (2013).
3. Masson, J.-F., Murray-Méthot, M.-P. & Live, L. S. Nanohole arrays in chemical analysis: manufacturing methods and applications. *Analyst* 135, 1483-1489 (2010).
4. Vogel, N., Goerres, S., Landfester, K. & Weiss, C. K. A Convenient Method to Produce Close-and Non-close-Packed Monolayers using Direct Assembly at the Air–Water Interface and Subsequent Plasma-Induced Size Reduction. *Macromolecular Chemistry and Physics* 212, 1719-1734 (2011).
5. Ting, Y.-H. et al. Surface roughening of polystyrene and poly (methyl methacrylate) in Ar/O2 plasma etching. *Polymers* 2, 649-663 (2010).
6. Wang, F., Deng, R. & Liu, X. Preparation of core-shell NaGdF 4 nanoparticles doped with luminescent lanthanide ions to be used as upconversion-based probes. *Nature protocols* 9, 1634 (2014).
7. Gnanasammandhan, M. K., Idris, N. M., Bansal, A., Huang, K. & Zhang, Y. Near-IR photoactivation using mesoporous silica–coated NaYF4:Yb,Er/Tm upconversion nanoparticles. *Nature Protocols* 11, 688, doi:10.1038/nprot.2016.035 (2016).
8. Mayer, K. M. & Hafner, J. H. Localized surface plasmon resonance sensors. *Chemical reviews* 111, 3828-3857 (2011).
9. Petryayeva, E. & Krull, U. J. Localized surface plasmon resonance: nanostructures, bioassays and biosensing—a review. *Analytica chimica acta* 706, 8-24 (2011).

10. Liz-Marzán, L. M. Tailoring surface plasmons through the morphology and assembly of metal nanoparticles. *Langmuir* 22, 32-41 (2006).
11. Farcau, C., Giloan, M., Vinteler, E. & Astilean, S. Understanding plasmon resonances of metal-coated colloidal crystal monolayers. *Applied Physics B* 106, 849-856 (2012).
12. Sugawa, K. et al. Metal-Enhanced Fluorescence Platforms Based on Plasmonic Ordered Copper Arrays: Wavelength Dependence of Quenching and Enhancement Effects. *ACS Nano* 7, 9997-10010, doi:10.1021/nn403925d (2013).
13. Schwind, M., Kasemo, B. & Zorić, I. Localized and Propagating Plasmons in Metal Films with Nanoholes. *Nano Letters* 13, 1743-1750, doi:10.1021/nl400328x (2013).
14. Xie, F. et al. Nanoscale control of Ag nanostructures for plasmonic fluorescence enhancement of near-infrared dyes. *Nano Research* 6, 496-510 (2013).
15. Fan, X., Zheng, W. & Singh, D. J. Light scattering and surface plasmons on small spherical particles. *Light: Science &Amp; Applications* 3, e179, doi:10.1038/lsa.2014.60 (2014).
16. Shuford, K. L., Ratner, M. A. & Schatz, G. C. Multipolar excitation in triangular nanoprisms. *The Journal of chemical physics* 123, 114713 (2005).
17. Biswas, R., Neginhal, S., Ding, C., Puscasu, I. & Johnson, E. *Mechanisms underlying extraordinary transmission enhancement in subwavelength hole arrays.* JOSA B 24, 2589-2596 (2007).
18. Bonod, N., Enoch, S., Li, L., Popov, E. & Nevière, M. Resonant optical transmission through thin metallic films with and without holes. *Opt. Express* 11, 482-490 (2003).
19. Sannomiya, T., Scholder, O., Jefimovs, K., Hafner, C. & Dahlin, A. B. Investigation of plasmon resonances in metal films with nanohole arrays for biosensing applications. *Small* 7, 1653-1663 (2011).

20. Homola, J. Surface plasmon resonance sensors for detection of chemical and biological species. *Chemical reviews* 108, 462-493 (2008).

21. Haase, M. & Schäfer, H. Upconverting nanoparticles. *Angewandte Chemie International Edition* 50, 5808-5829 (2011).

22. Li, P. et al. Lanthanide-doped upconversion nanoparticles complexed with nano-oxide graphene used for upconversion fluorescence imaging and photothermal therapy. *Biomaterials Science* 6, 877-884, doi:10.1039/C7BM01113J (2018).

23. Wen, S. et al. Advances in highly doped upconversion nanoparticles. *Nature Communications* 9, 2415, doi:10.1038/s41467-018-04813-5 (2018).

24. Huang, Y. et al. Hybridized plasmon modes and near-field enhancement of metallic nanoparticle-dimer on a mirror. *Scientific Reports* 6, 30011, doi:10.1038/srep30011

25. Seo, S., Chang, T.-W. & Liu, G. L. 3D Plasmon Coupling Assisted Sers on Nanoparticle-Nanocup Array Hybrids. *Scientific Reports* 8, 3002, doi:10.1038/s41598-018-19256-7 (2018).

26. Das, R. & Soni, R. K. Synthesis and surface-enhanced Raman scattering of indium nanotriangles and nanowires. *RSC Advances* 7, 32255-32263, doi:10.1039/C7RA03317F (2017).

27. Tian, L., Gandra, N. & Singamaneni, S. Monitoring Controlled Release of Payload from Gold Nanocages Using Surface Enhanced Raman Scattering. *ACS Nano* 7, 4252-4260, doi:10.1021/nn400728t (2013).

28. Wu, Q. et al. Universal Multifunctional Nanoplatform Based on Target-Induced in Situ Promoting Au Seeds Growth to Quench Fluorescence of Upconversion Nanoparticles. *ACS Sensors* 2, 1805-1813, doi:10.1021/acssensors.7b00616 (2017).

29. Feng, A. L. et al. Selective enhancement of red emission from upconversion nanoparticles via surface plasmon-coupled emission. *RSC Advances* 5, 76825-76835 (2015).

30. Abadeer, N. S., Brennan, M. R., Wilson, W. L. & Murphy, C. J. Distance and plasmon wavelength dependent fluorescence of molecules bound to silica-coated gold nanorods. *ACS nano* 8, 8392-8406 (2014).

31. Gandra, N. et al. Probing Distance-Dependent Plasmon-Enhanced Near-Infrared Fluorescence Using Polyelectrolyte Multilayers as Dielectric Spacers. *Angewandte Chemie* 126, 885-889 (2014).

Chapter 6 Plasmonic Enhanced Triplet-Triplet Annihilation Upconversion for Broadband Photocatalysis

6.1 Introduction

Solar-energy driven semiconductor photocatalysts have received considerable attention in the field of environmental protection[1,2] due to their potential for the photodegradation of organic pollution.[3,4] A significant challenge of current research is to realize broadband solar energy harvesting, which is inherently limited by the semiconductor band gap. Upconversion nanomaterials, which convert low-energy photons into high-energy ones, offer versatile absorptions to efficiently harvest the visible region and even the infrared region of sunlight.[5,6] Lanthanide-doped nanoparticles have been demonstrated with potential to enhance the performance of solar cells and photocatalytic systems through photon upconversion. However, their practical use is currently hindered due to inherently low upconversion quantum yield, and the requirement for high-intensity excitation (10 to$10^4\ W/cm^2$).[7,8,9]

Compared to rare-earth based upconversion, the Triplet-Triplet annihilation process has a much stronger absorption coefficient of sensitizer ($\sim 10^{-17} cm^2$), which is capable of operating efficiently with incoherent and low-power radiation (1- 10 mW/cm^2) such as sunlight.[10,11] Further, by combining various types of sensitizers and activators, the wavelength ranges of excitation and emission of TTA-UC can be precisely tuned, thus favoring the requirements of upconversion-assisted photocatalytic systems. Although TTA-UCNPs already have higher quantum yield (2.1%-30%) compared to rare-earth based nanoparticles,[12,13,14] it is desirable to further improve the upconversion quantum yield for sunlight-powered applications.

A possible approach to realize a more efficient upconversion process and high efficiency photocatalytic activity is by integrating a plasmonic metal nanostructure with TTA-UC nanoparticles and the

semiconductors. The electromagnetic field enhancement at the metal/dielectric interface, enables higher efficiency upconversion. In parallel, to further boost this upconversion quantum yield, metallic nanostructures have also been recognized as photosensitizers when in contact with wide bandgap semiconductors by enabling energetic hot electron transfer into the semiconductors.[15,16,17] Therefore, one can expect an advanced architecture of plasmonic nanopattern metal to simultaneously realize an upconversion photoluminescence enhancement, and act as an efficient photosensitizer.

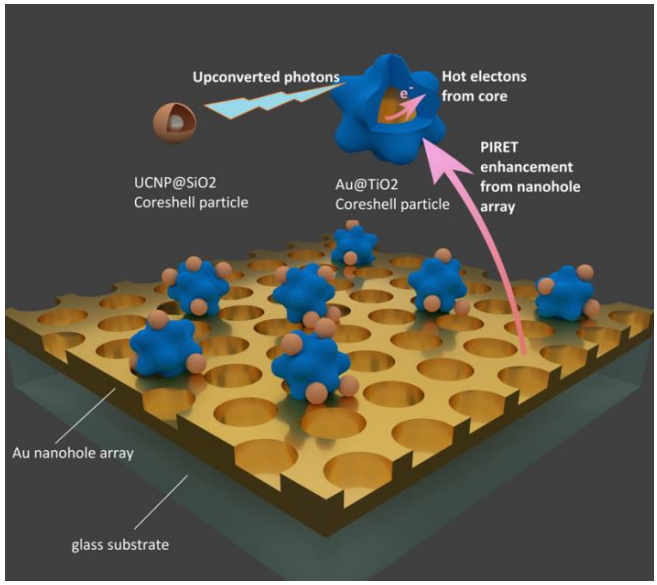

Figure 6- 1 A recyclable Au nanohole film/TTA-UCNPs/Au@TiO_2 coupled architecture as presented in three-dimension (3D).

In this work we have developed a novel Au nanohole film/TTA-UCNPs/Au@TiO_2 coupled architecture for high efficiency photocatalysis activity enhancement. The system is depicted in Figure 6-1, which was operated in an oxygen-rich aqueous phase and excited by an AM 1.5G solar simulator. There are three key components in this structure: Au nanohole film bottom layer, TTA-UCNPs and Au@TiO_2 nanoparticles on the top layer. The long-range ordered Au nanohole array film excites surface plasmon polariton (SPP) modes which enhance the TiO_2 semiconductor and the UCNPs through the plasmon-induced resonance

energy transfer (PIRET). The photoluminescence of TTA-UC was enhanced 15-fold by an optimized Au nanohole array substrate. An enhanced photocatalytic rate, 5 times faster than the benchmark Au@TiO_2 sample, was achieved using the Au nanohole film/TTA-UCNPs/Au@TiO_2 coupled sample. The results obtained pave the way for a more rational design of plasmon-enhanced upconversion nanostructure in the search for a high-performance photocatalytic system operating under natural sunlight illuminations.

6.2 Materials and Methods

6.2.1 UCNPs TTA@SiO_2 Step-by-Step Synthesis Process

TTA@SiO_2 in figure 6-2 (a) was synthesized following the protocol provided by Liu et al.[18] First, 2.0 g of Pluronic F127, 0.5 mg (7.8x10-7 mol) of 2, 3, 7, 8, 12, 13, 17, 18-octaethylporphyrin palladium ($C_{36}H_{46}N4_{Pd}$) and 10 mg ($3.0x10^{-5}$ mol) of 9, 10-diphenylanthracene ($C_{26}H_{18}$) were prepared and transferred into a 100-mL three-neck round-bottomed flask.

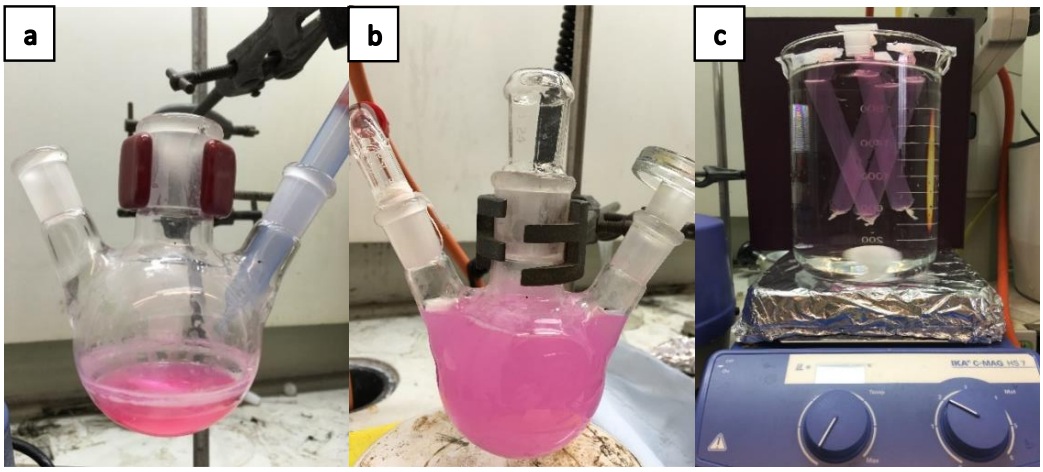

Figure 6- 2 Photographs of the experimental setup and condition for TTA@SiO_2 synthesis. (a) the first mixture of the precursor before drying; (b) powder obtained from drying process was dissolved in HCl; (c) dialysis tubing process with a handler and a magnetic stirrer.

These precursors were dissolved in the organic solvent mixture of toluene and dichloromethane, 15 ml and 5 ml, respectively and started stirring. When the powder was completely dissolved and the color of the solution changed to lavender as depicted in figure 6.2 (a), the solution was left to dry out in a mild nitrogen flow for 24h to be exchanged into water-based solution.

To ensure there was no solvent residues left after drying, a vacuum pump was used to provide a reduced pressure environment to the flask at 40 C. Then the solid product was dissolved in 100 mL of HCl (0.85 mol/L^{-1}) and stirred using a magnetic stirrer for 10 minutes. When the powdery product was once dissolved as depicted in figure 6.2 (b), 2 mL of TEOS was added into the solution and kept stirred for 6 hours at room temperature. Subsequently, 450 µL of 2.1 mmol DEDMS was added for another 48 hours stirring. Then the solution was transferred into dialysis tubes for nanoparticle synthesis (the amount of the tube was various according to the size of the tube). The dialysis tubes were then tightly sealed and hanged inside 2-liter beaker glass previously filled with DI water of approximately 1.8 liter. A large magnetic stirrer was later on chosen to stir DI water inside the beaker. The experimental setup is depicted in Figure 6.2 (c). To remove large particulate of organic component and to obtain sufficiently uniform particle geometry, this synthesis process took 2 days (48 hours) to complete, DI water was replaced 4 times within every 24 hours. The product was verified without impurities and ready for further use. The solution can be stored in the refrigerator under 4 ^{o}C within a week.

6.2.2 Fabrication of 4×4 $\boldsymbol{cm^2}$ substrates of periodic Au nanostructure array

The colloidal lithography method[21,45] was used to prepare large-area polystyrene monolayers. In brief, monodisperse polystyrene (PS) nanoparticles with a diameter of 500 nm were mixed with the same amount of ethanol. Approximately 9 to 12 μL of the mixed solution was spread homogeneously onto the surface

of a clean silicon wafer (~50 mm ×50 mm), which had previously been exposed to UV-Ozone for 35 minutes. Afterwards, the silicon wafer covered by a single layer of polystyrene was then steadily and slowly immersed in a polypropylene vessel filled with 300 mL of Milli-Q water, allowing the polystyrene nanoparticles forming an ordered monolayer on the air-water interface. To improve the uniformity of PS array, the water surface tension was modified by adding 3 μL of 2% sodium deodecyl sulfate solution. This procedure was repeated 3 times in order to obtain a 4×4 cm^2 of PS monolayer with highly ordered lattice. Finally, this PS monolayer was transferred to the Au surface (50 nm Au layer deposited on a cleaned glass substrate (4×4 cm^2)) by a 'lift-off' technique. This type of PS monolayer at Au surface on glass substrates were obtained by repeating the above-mentioned procedures several times as needed. Afterwards, three types of plasmonic nanostructure substrates were prepared, three above-mentioned PS monolayer@Au surface@glass substrates were treated by 0s, 10s, 25s O_2 plasma etching, respectively. Subsequently, the as-prepared substrates were transferred into the vacuum chamber of the Mantis e-beam evaporation system, for Au deposition with a monitored thickness of 50 nm. Finally, the PS nanoparticles array mask were gently peeled off by tape, and the surface of the treated substrates were ready for scanning electron microscopy (SEM) characterization.

6.2.3 Synthesis of Core-Shell Au@TiO_2 nanoparticles

Typically, the synthesis of Au@TiO_2 nanoparticles is carried out in line with the literature.[28] Minor modifications are listed here: 3 mL of 0.01 M $HAuCl_4$ solution (Sigma-Aldrich, UK) was added into 4.5 mL of 0.01 M sodium citrate solution (Sigma-Aldrich, UK). The mixed solution was then stirred vigorously for 5 minutes. Afterwards, 2 mL of 0.01 M ascorbic acid solution was added into the mixture dropwise with stirring continuously for 10 minutes. During this process, the color of the solution turned from orchid to reddish brown due to the localized plasmon resonance shift. Then, 4.5 mL 0.04 M TiF_4

solution was added into the reddish-brown mixture. Subsequently, 70 mL deionized water was used to dilute the mixture. All the solution was transferred into a 100 mL Teflon-lined stainless autoclave. The hydrothermal reaction took place in an oven kept at 180 C for 48 hours. Finally, the as-synthesized product was cooled to room temperature, washed and centrifuged by ethanol at 5400 rpm and 15 minutes for 3 times. The washed sample was dried in an oven at 70 C and was weighed for further use.

6.3 Results and Discussion

6.3.1. Properties of TTA-UCNPs

TTA-UC nanoparticles obtained by a direct micelle assisted approach were characterized.[18] Figure 6-3 (a) presents a typical TEM image of TTA-UCNPs, confirming that the TTA-UCNPs are spherical and monodispersed, with a diameter of 10±1.5 nm. Figure 6-3 (b) shows the UV-visible absorption spectrum of dispersed TTA-UCNPs dissolved in DI-water, showing an absorption band between 530 nm and 550 nm. Figure 6-3 (b) has pronounced characteristic peak pairs of 390 nm, and 515 nm and 546 nm indicate the presence of Palladium octaethylporphyrin (PdOEP, excitation 500-550 nm) and 9, 10-diphenylanthracene (DPA, emission 400-500 nm) in the silica shell.[19] PdOEP and DPA were selected as the sensitizer and annihilator, respectively. Polyethyleneglycol F127 was employed to load PdOEP and DPA into the SiO_2 microcapsule.

The Jablonski diagram (Figure 6-3(c)) shows five possible steps of TTA-UC[20]: (1) Low energy photon absorption, (2) Intersystem crossing (ISC), a sensitizer first absorbs a low energy photon and rapidly populates its first triplet excited state after ISC from the singlet state. (3) The triplet energy is then transferred to an annihilator species through triplet-triplet energy transfer (TTET), generating one triplet excited annihilator molecule. (4) Triplet-triplet annihilation and (5) High energy photon emission. Processes (4) and (5) shows that when two triplet excited annihilator molecules meet, triplet-triplet

annihilation process occurs to form a singlet excited annihilator, which can deactivate to its ground state by emitting a high energy photon. The emission profile of these nanoparticles was determined with excitations from 500 nm to 580 nm, where anti-Stokes (390 nm to 490 nm, Figure 6-3 (d)) and Stokes (640 nm to 710 nm, Figure 6-3 (e)) emissions are observed. In Figure 6-3 (d), the upconversion emission intensity forms a plateau (emission wavelength 425-437 nm) when excited by 515-530 nm light. The emission intensities decline gradually when the excitation wavelengths approaching the boundaries of the absorption range of PdOEP (500-550 nm). This result demonstrates that the TTA-UC system is capable of converting photons in the range 515 to 530 nm. The strong intensity of the upconversion emissions also indicate that these TTA-UCNPs operate effectively under low-intensity excitation, in an oxygen-rich aqueous phase condition. These properties can be utilized in sub-bandgap harvesting for the enhancement of photocatalysis activity of semiconductors.

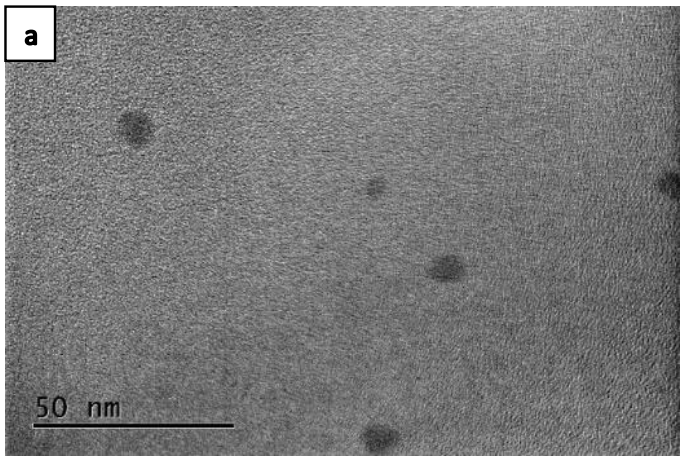
a
50 nm

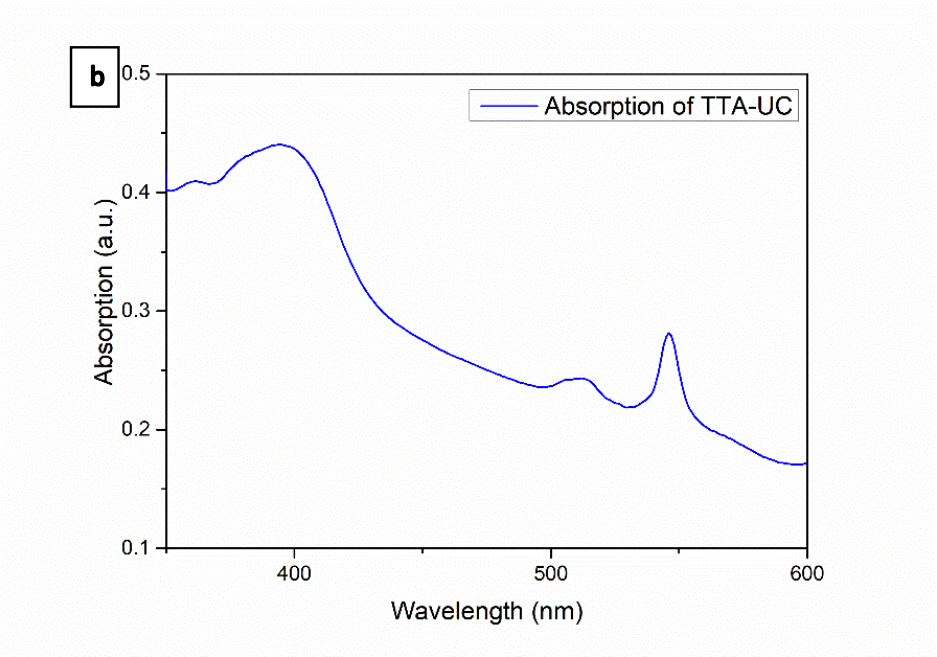
b
Absorption of TTA-UC
Absorption (a.u.)
0.1
0.2
0.3
0.4
0.5
400
500
600
Wavelength (nm)

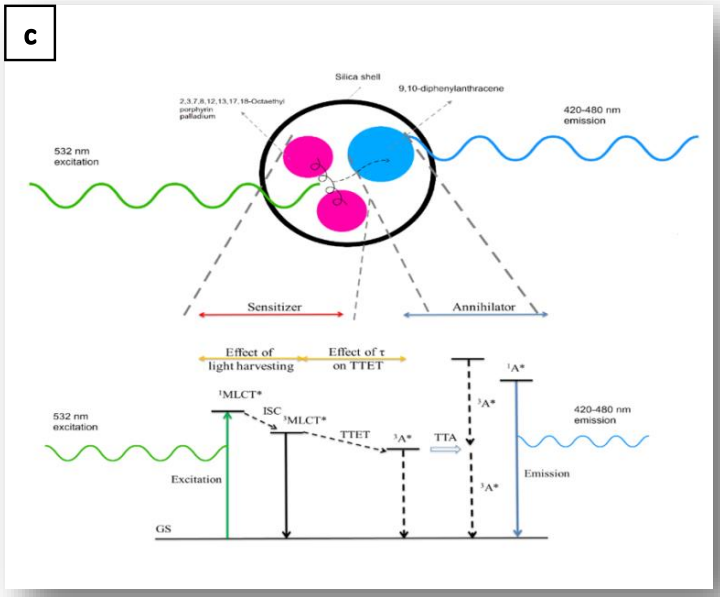
c
Silica shell
9,10-diphenylanthracene
2,3,7,8,12,13,17,18-Octaethyl porphyrin palladium
420-480 nm emission
532 nm excitation
Sensitizer
Annihilator
Effect of light harvesting
Effect of τ on TTET
^{1}MLCT*
ISC
^{3}MLCT*
TTET
^{3}A*
TTA
^{1}A*
532 nm excitation
420-480 nm emission
Excitation
Emission
GS

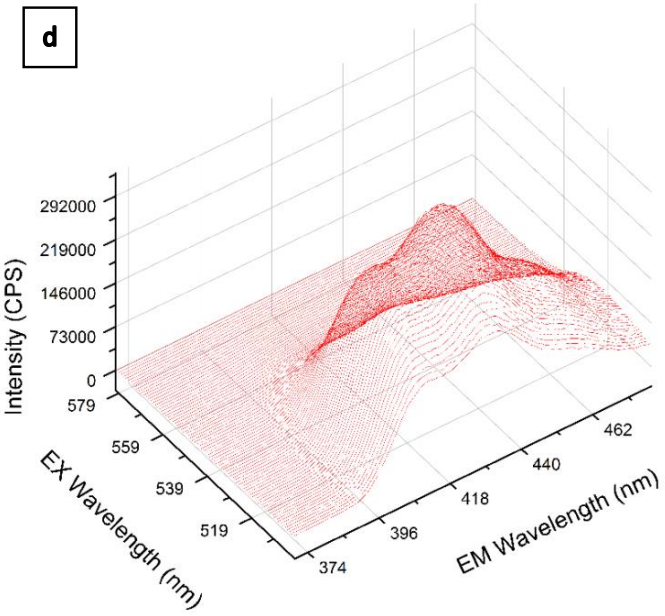
d
Intensity (CPS)
292000
219000
146000
73000
0
579
559
539
519
EX Wavelength (nm)
374
396
418
440
462
EM Wavelength (nm)

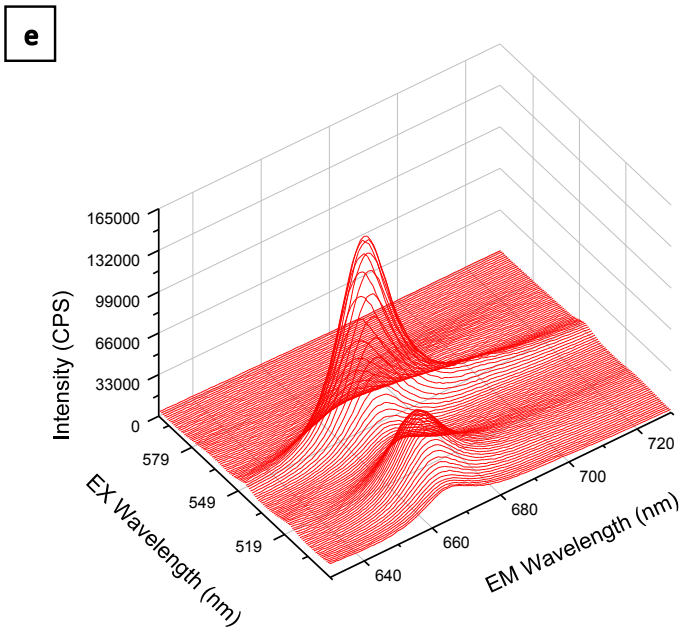

Figure 6- 3 (a-c) Material properties of TTA-Upconversion nanoparticles. (a) TEM image of TTA-UCNPs. (b) UV-Visible measurement of the absorbance spectra of TTA-UCNPs in aqueous solution. (c) Schematic diagram of the inside part of the of TTA-UCNPs@SiO_2 core/shell nanoparticles and energy transfer processes of TTA-UC.[46] (d) Anti-stokes emission (EM wavelength) diagram of TTA-UCNP as a function of different excitations (EX wavelengths, 500 nm-580 nm). (e) Stokes (EM wavelength) diagram of TTA-UCNP as a function of different excitations (EX wavelengths, 500 nm-580 nm). The UC photoluminescence from the TTA-UCNPs dissolved in DI-water was collected under 150 W Xenon solar simulator (Newport 94021A) illumination with AM 1.5G filter for a range of 10~100 mW/cm^2.

6.3.2 Au nanostructure arrays and TTA-UCPL enhancement

UC emission intensities and lifetimes of the upconversion process are significant indicators of optical characteristics in designing TTA-UC enhanced photocatalysis. The TTA-UC processes influenced by plasmonic effect of gold nanostructure arrays are investigated. For the enhancement of TTA-UC processes,

it is desirable to assemble a precisely controlled, close-packed and large area gold nanostructure array with tunable optical properties. Plasmonic nanotriangle and nanohole array substrates ($4\times 4\ cm^2$) were fabricated by nanosphere lithography (NSL).[21] Figure 6-4 (a-d) present the SEM images of gold nanotriangle and nanohole arrays developed via this approach. The structural evolution gradually from nanotriangle to nanohole array benefits from the precise control of the duration time of O_2 plasma treatment of the polystyrene masks. (As shown in Chapter 5, Experimental section)

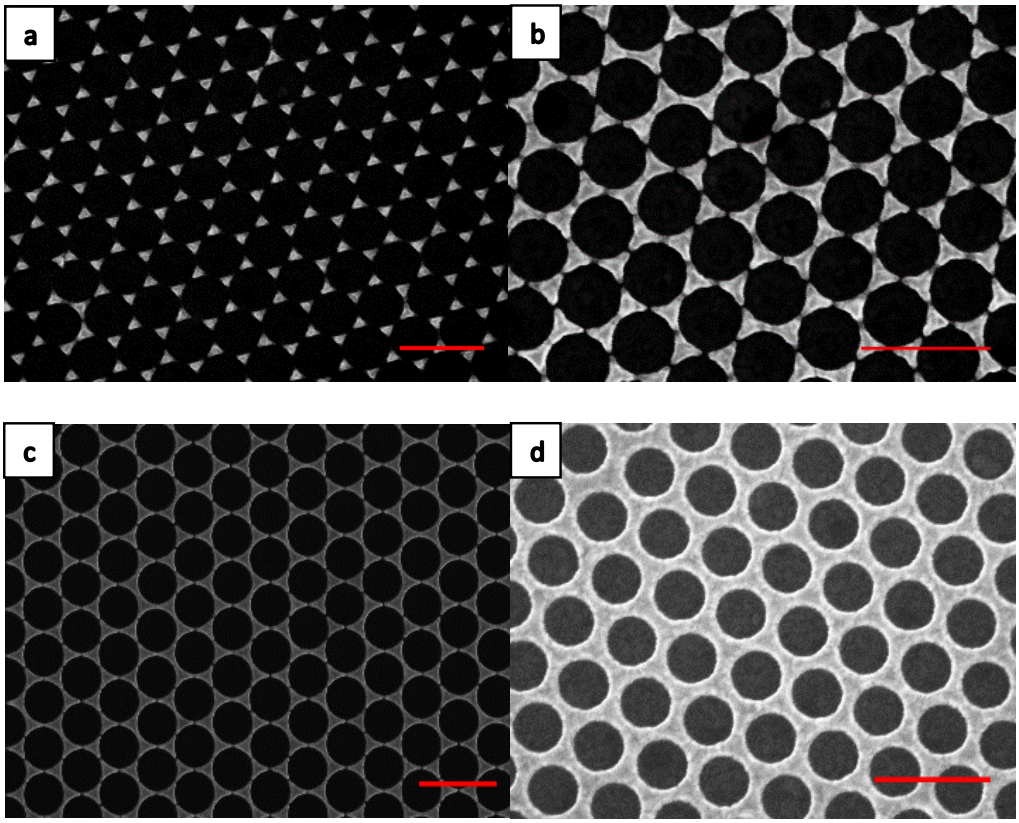

Figure 6- 4 (a-d) Scanning electron microscopy (SEM) images of Au nanohole array on Au film fabricated through nanosphere lithography using 280 nm polystyrene. The duration of Oxygen plasma treatments were (a)-0s, (b)-12s, (c)-20s, (d)-25s, respectively. The scale bar in these figures are 500 nm, respectively.

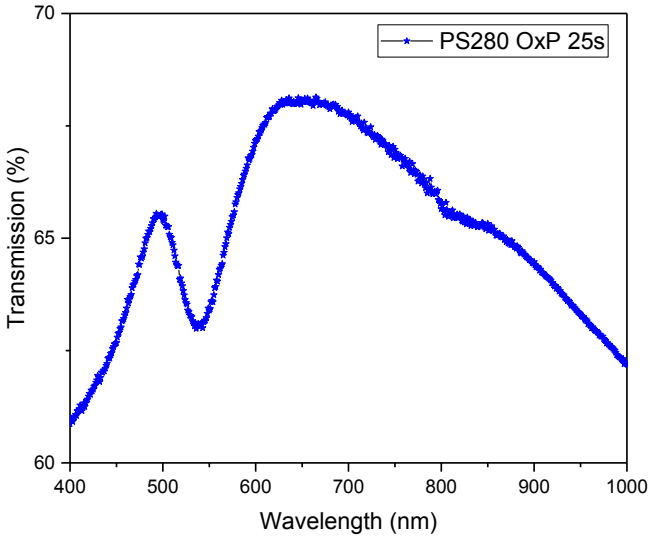

Figure 6- 5 Transmission spectra for PS280 nm polystyrene treated by oxygen plasma for 25s nanohole array deposited on transparent glass substrate sample.

We measured the enhancement of photoluminescence spectroscopy with and without the optimized plasmonic substrate. TTA-UC nanoparticles are conjugated to Au nanohole array films with different geometrical parameters, compared to their counterpart with TTA-UC nanoparticles deposited on flat Au substrate sample. Optimization of the Au nanostructures leads to a maximum 15 times increase in the photoluminescence intensity compared with control samples without plasmonic component (Figure 6-6 a). The UV-Visible transmission spectra (Figure 6-5) was characterized by Cary 5000 spectrophotometer. The excitation of SPP mode in Au nanostructure arrays which is directly related to the pitch size of the nanoholes and the excitation of LSPR mode which connects to the nanoscale morphology both lead to a highly localized electromagnetic near field on the nanoscale, thus giving us a significant wavelength–tunable enhancement during the light-matter interaction process. When excited by light resonant with the

SPP mode, the Au nanostructure arrays are involved in the energy transferring process by exciting the carriers in the semiconductor non-radiatively. When the incident light resonances with the LSPR mode, the Au nanostructure arrays generate substantial near-field enhancements near the surface of the thin plasmonic film, leading to increased levels of light absorption by the PdOEP.[22,26] The DPA:PtOEP system can generate higher density of excited triplet states as a result of near-field enhancement under the same excitation intensity, and therefore a corresponding increased photoluminescence intensity. By varying the geometrical parameters of the Au nanostructures, the scaling the peak positions of the plasmon resonances was modified as a function of the geometries. In order to maximize either of these plasmonic enhancement effects to be active, the spectral overlap between surface plasmon resonance of the substrate and the absorption/emissions spectral of UCNPs have been demonstrated as the key to boost the upconversion efficiency.[23,24] The nanohole array that deposited on transparent glass and treated by oxygen plasma for 25s exhibits a strong plasmon resonance band centered at 530 nm, which matches the absorption band of the TTA-UCNPs (Figure 6-3 (b)). Therefore, the nanohole array film could give rise to the near-field enhancements at the right wavelengths required by TTA-UC.

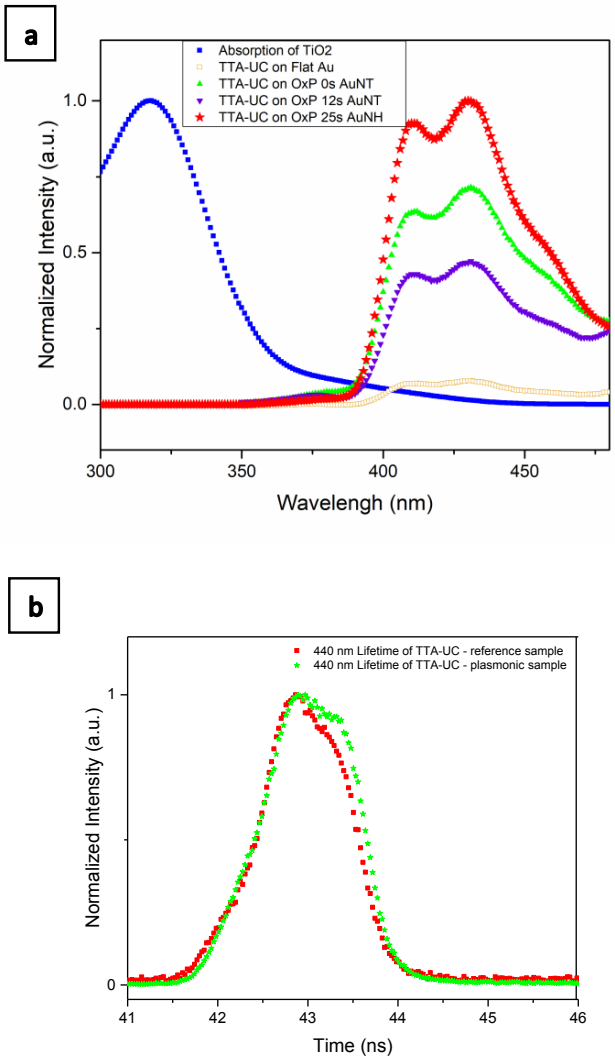

Figure 6- 6 (a) TTA-UC luminescence of TTA-UC reference sample and plasmon-enhanced luminescence of same amount of TTA-UC sample with the absorption spectra of Au@TiO_2 DI-water solution. The plasmonic substrates were treat by 0s, 12s, 25s Oxygen Plasma, respectively. (b) Time-correlated single photon counting measurement of time-evolution of TTA-UC as the reference and TTA-UC deposited on 25s oxygen plasma treated Au nanohole array substrate at 440 nm. The excitation for the measurement of time-evolution is by 532 nm nanosecond pulsed laser, with 0.027 ns per channel and with a 14nm bandpass.

Then, time-evolution of TTA-UC decay curves were measured by time-correlated single-photon counting approach. Figure 6-6 (b) signify the normalized intensity decay curves of upconversion emission at 440 nm. The temporal evolution of the TTA-UC emission as a function of time can be fitted by a single-exponential decay function[25]:

$$I(t)= I_1 \exp(-t/\boldsymbol{\tau_D}) \qquad \text{(Equ 6-1)}$$

where I(t) represent the photoluminescence intensity at a specific time point corresponding to the on and off processes of the pulsed laser. $\boldsymbol{\tau_D}$ is decay lifetime of the UCPL. It is clear that the decay time of the UCPL of TTA-UC deposited on Au nanohole array substrate is longer than that deposited on flat Au film substrate (reference sample). In addition to the absorption enhancement, the change of radiative decay rate of excited state of emitter can also contribute to the increased photoluminescence. A longer decay time implies that the triplet sensitizer exhibits longer lifetime, which in turn would enhance energy transfer processes between the triplets of sensitizer and acceptor (TTET). Given this observation, longer PdOEP excited state lifetime would be expected to deplete the reservoir of excited triplet states slower, and thus leading to an increased TTA efficiency.[22,27] This result indicates that UCPL enhancement can also be attributed to the radiative mechanism, which has been demonstrated in previous Au nanoparticles/TTA-UC lifetime measurement.[25] To this stage, we have successfully applied the Au nanostructures film to substantially enhance the TTA-UC photoluminescence. The minor spectra overlap between the absorption of Au@TiO_2 and upconversion photoluminescence of TTA-UCNPs indicates the availability of radiative energy transfer from TTA-UCNPs to Au@TiO_2. This could be attributed to one of the mechanisms for the photocatalytic activity enhancement in the next section. These results suggest that plasmon-enhanced TTA-UCPL can be utilized as a very promising component in thin film devices upon sunlight illumination.

6.3.3 Enhancement of Au@TiO_2 photocatalytic activity

Next, we examined the Au nanostructure/TTA-UCNPs/Au@TiO_2 coupled system for the photodegradation of methyl orange (MO). Core-shell Au@TiO_2 nanoparticles with truncated wedge-shaped morphology was selected as the benchmark sample, because it has been proved to be a good performance candidate upon ultraviolet or visible light irradiation.[28] Besides, Au@TiO_2 nanoparticles can be synthesized with a simple and flexible hydrothermal route at relatively large scale.

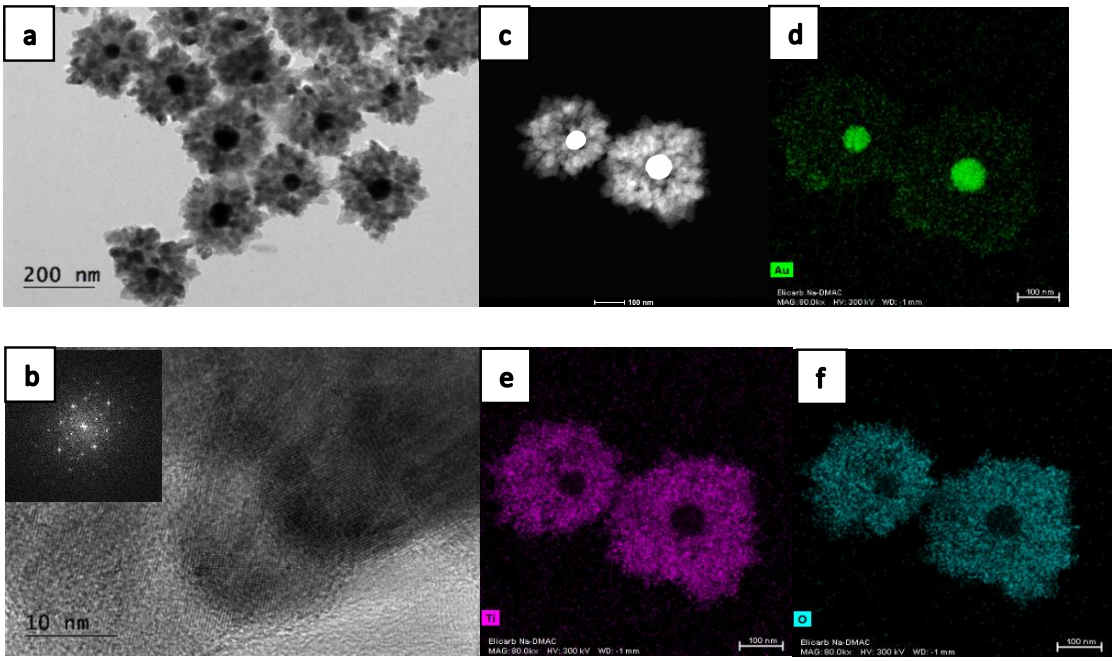

Figure 6- 7(a) TEM images of the core-shell structure Au@TiO_2 nanoparticles. (b) HR-TEM images of the core-shell structure Au@TiO_2 nanoparticles. The inset in part (b) is the corresponding FFT patterns. (c-f) STEM image of the core-shell structure Au@TiO_2 nanoparticles and elemental mapping of Au, Ti, O element, respectively.

Figure 6-7 (a) shows the TEM images of core-shell Au@TiO_2 nanoparticles with about 35 nm Au cores and about 100 nm radial wedge-shaped TiO_2 layers. HR-TEM (Figure 6-7 (b)) and the inset FFT pattern indicate high-quality crystallinity of the Au@TiO_2 nanoparticles. The FFT pattern shows a diffuse diffraction circle, which can be attributed to (101) planes and anisotropic diffraction of (004) planes, respectively. Figure 6-7 (c-f) demonstrate STEM image of the core-shell structure Au@TiO_2 nanoparticles and elemental mapping of Au, Ti, O element, respectively. The elements distribution of Au@TiO_2 can be clearly obtained from these figures.

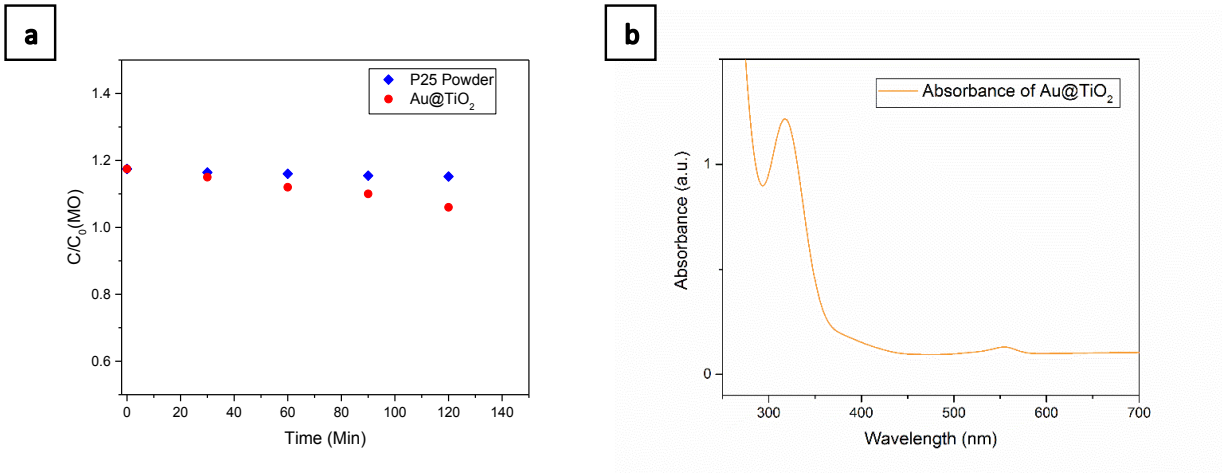

Figure 6- 8 (a) Photodegradation of MO by 20 mg P25 as reference and 20 mg Au@TiO_2 in aqueous phase, with a reaction of 120 minutes, under irradiation of 532 nm laser, respectively. (b) UV-Visible measurement of the absorbance spectra of Au@TiO_2 nanoparticles in aqueous solution.

Our result (Figure 6-8(a)) confirmed that after illuminated by 532 nm laser, Au@TiO_2 nanoparticles showed a noticeable photocatalytic activity under 532 nm ($\pm$5 nm bandwidth) laser illumination, while the benchmark commercial Degussa P25-Titanium Dioxide Nanopowder (TiO_2, Degussa, Rutile:Anatase/ 85:15, 99.9%, 20nm) remained inactive for up to 6 hours reaction. This is because Degussa P25 cannot generate reactive species when excited by light with wavelength longer than 387 nm (3.2 eV). However,

owing to the surface plasmon resonance (SPR) effect of Au cores, Au@TiO_2 nanoparticles exhibit an absorption band around 550 nm (Figure 6-8(b)). The hetero-interface between Au core and TiO_2 shell shows good continuity and leads to the modification of electronic state of Au and TiO_2.[29] In addition to enable the visible light absorption TiO_2, Au cores are able to trap electrons, improve the lifetimes of electron-hole pairs. The high Fermi level of the Au can efficiently separate electron-hole pairs of TiO_2, thus improving the interfacial charge-transfer process.[30] Subsequently, the photocatalytic activity of Au@TiO_2 nanoparticles mixed with TTA-UCNPs were measured. Under simulated solar irradiation, Au@TiO_2 with the assistance of TTA-UC nanoparticles demonstrated about 1.63 times faster MO degradation rate than Au@TiO_2 benchmark (Figure 6-9 (a)). This enhanced photocatalytic activity indicates the existence of radiative transfer between TTA-UCNPs and Au@TiO_2 nanoparticles. The neighboring TTA-UCNPs were demonstrated to provide an extra pathway for Au@TiO_2 to harness visible range light. This pathway should be attributed to the radiative energy transfer between TTA-UCNPs and Au@TiO_2, where the upconverted photons reach the band edge of Au@TiO_2.

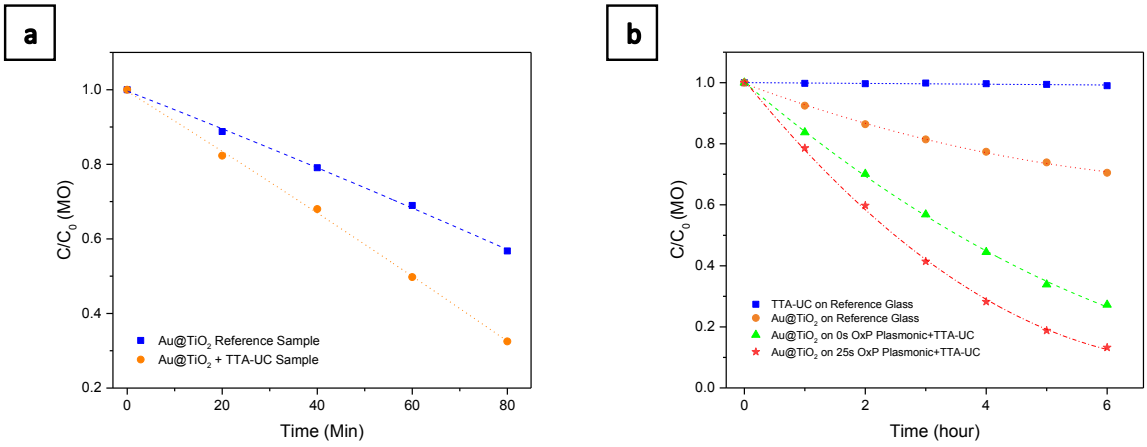

Figure 6- 9 (a) Photodegradation of MO by 100 mg Au@TiO_2 as reference and 100 mg Au@TiO_2 with the assistance of TTA-UCNPs in aqueous phase, with a reaction of 80 minutes, under irradiation of simulated sunlight A.M 1.5G, respectively. (b) Photodegradation of MO by 2mg Au@TiO_2 as reference

and 2 mg Au@TiO_2 with the assistance of TTA-UCNPs and Au nanohole array film substrates, with a reaction time of 6 hours under irradiation of simulated sunlight A.M 1.5G, respectively.

To investigate the Au nanostructure film/TTA-UCNPs/Au@TiO_2 substrates for the photocatalytic activity enhancement, we measured the photodegradation rate of MO by a set of samples as shown in Figure 6-9 (b). Based on the experimental results, it is demonstrated that our substrates realized a hybrid structure, achieving broadband photocatalyst by taking advantage of both plasmonic and TTA-UC effects. Specifically, the hybrid structure is composed of visible-absorbing plasmonic Au nanohole arrays, TTA-UC nanoparticles (TTA-UCNPs) and catalytically active Au@TiO_2 nanoparticles. Overall, significant 5 times enhancement was achieved by the hybrid structure compared with benchmark Au@TiO_2 nanoparticles deposited on glass. It confirms that Au nanohole array sample (treated by 25s oxygen plasma) was the best candidate. The mechanism in which the plasmonic sensitization of noble metal facilitates the selective formation of electron-hole pairs in the near-surface region of the neighboring semiconductor has been widely accepted.[31,32] According to previous studies, three mechanisms allow plasmonic sensitization to occur: direct electron transfer (DET), plasmon-induced resonant energy transfer (PIRET) and increased light scattering.[33,34] However, the detailed enhancement depends on optical features and geometrical relationships. PIRET process is a result of nonradiative dipole-dipole coupling between the plasmon of the Au and the electron/hole pairs in the TiO_2, and thus with enhanced exciton generation rate.[35,36,37] This mechanism can enhance the photocatalytic activity even with the existence of insulating barrier between Au and TiO_2.

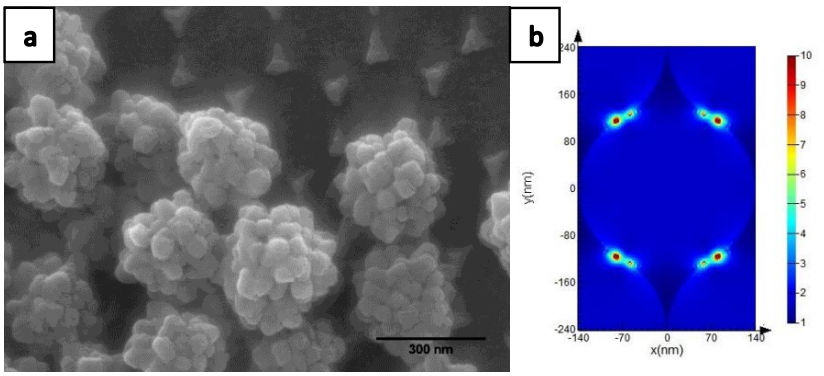

Figure 6- 10 (a) Scanning electron microscopy (SEM) images of Au@TiO_2 nanoparticles deposited on the Au nanotriangle array film, PS were not treated by Oxygen Plasma. (b) The E^2-field mapping graphs of corresponding Au nanotriangle array film at 532 nm wavelength.

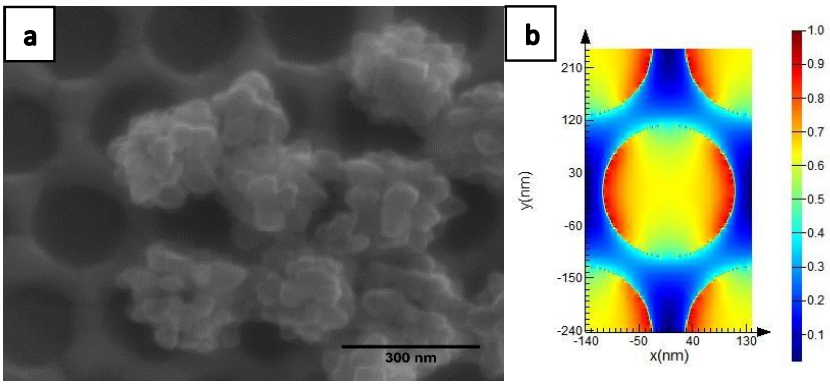

Figure 6- 11 (a) Scanning electron microscopy (SEM) images of Au@TiO_2 nanoparticles deposited on the Au nanohole array film, PS were treated by 25s Oxygen Plasma. (b) The E^2-field mapping graphs of corresponding Au nanohole array film at 532 nm wavelength.

For Au nanohole arrays, the SPP mode is able to provide an enhanced localized field with a much larger effective area and higher intensity which determines that PIRET mechanism should be the dominant effect in this case. By contrast, the direct electron transfer (DET) from the LSPR mode only requires an intimate contact between the Au and TiO_2, where a proper band alignment and electronic coupling established at

the interface of Au and TiO_2 components while its enhancement effect is actually much weaker compared to SPP mode due to its limited effective area.[35,38] In the DET case, ‘‘hot’’ electrons generated by plasmonic effect of Au nanostructures surface can directly jump over the interfacial Schottky barrier between Au and TiO_2. Alternatively, photonic enhancement can also enhance the solar energy collection of semiconductors. When surface plasmon resonance (SPR) energy is larger or equal to the bandgap energy of a semiconductor, the strong scattering of the nanohole array substrate may enhance the light absorption of Au@TiO_2. Within the large patterned plasmonic nanostructure, the incident light can be efficiently scattered multiple times, increasing the optical path length and light absorption for the neighboring semiconductor.[39,40]

To further study the SPP and LSPR resonance of Au nanostructure arrays, finite difference time domain (FDTD) method was used to calculate the electromagnetic field distribution around the light-illuminated plasmonic nanostructure. The E^2-field mapping graphs and transmission-reflection spectra for nanohole arrays is calculated through (FDTD) method. In the model, the gold nanohole arrays are defined by their thickness, pitch size and hole diameter. In this case, Au nanohole array is deposited on 50 nm Au layer. A board band plane wave source which is parallel to the film in x-y plane with a minimum wavelength of 400 nm and a maximum wavelength of 1000 nm is applied. It is demonstrated in the E^2-field mapping that dramatic enhancement of the electromagnetic field around the edges of Au nanohole arrays, where exist abundant “hot spots”.[40] The plasmonic hot spots generated by the Au nanohole array indicates an enhanced localized field which can increase the efficiency of the energy transferring process. EM field enhancement can also lead to a more effective injection of hot electrons from Au to the conduction band of TiO_2, thus favoring the creation of radical species that decompose the MO.[41,42] The superior photocatalytic activity achieved here should be mainly attributed to the localized electric field

improvement of the neighboring TiO_2 by the SPR effect of the Au, and especially, the hot spot resulting from the coupling effect of the opposite Au nanoparticles can magnify the localized electric fields significantly due to this favorable Au film/TiO_2/Au core nanostructure.[43] The EM field distribution figures shows that the EM field is sensitive to the size and shape of gold nanoparticles.[44] For the control sample nanotriangle array substrate, although the incident light can be much stronger absorbed at the tips of two Au nanotriangles, collected energy cannot be efficiently transferred due to weak coupling between the Au and semiconductor. Compared to nanotriangles, the nanohole arrays are able to utilize the SPP mode due to its periodic continuous nanostructure which gives extra PIRET enhancement effect. Variations in geometrical features of Au nanostructures can influence the EM field distributions and the coupling effect with semiconductors, thus leading to remarkable enhancement of photocatalytic performance of Au@TiO_2.

6.4 Conclusions

In summary, a novel plasmonic nanostructure substrate conjugated with TTA-UC nanoparticles was developed for enhanced Au@TiO_2 photocatalysis efficiency. We show that PIRET mechanism from plasmonic SPP mode and DET mechanism from LSPR mode are mainly responsible for the observed efficiency enhancement of Au@TiO_2. This is the first demonstration of plasmon-enhanced TTA-UC photoluminescence for the improvement of photocatalytic degradation of MO with visible and AM 1.5G irradiation. In comparison with control samples, our device showed the highest photocatalytic degradation rate, which was 5 times faster than that of Au@TiO_2. These results highlight that both green-to-blue TTA-UCNPs and plasmonic effect of noble metals are promising routes to enhance the visible light sensitivity under natural light environment. The coupling and synergistic effect of these two technologies are promising approach for practical applications.

Reference

1. Hoffmann, M. R., Martin, S. T., Choi, W. & Bahnemann, D. W. Environmental Applications of Semiconductor Photocatalysis. *Chemical Reviews* **95**, 69-96, doi:10.1021/cr00033a004 (1995).
2. Wang, H. *et al.* Semiconductor heterojunction photocatalysts: design, construction, and photocatalytic performances. *Chemical Society Reviews* **43**, 5234-5244, doi:10.1039/C4CS00126E (2014).
3. Zhang, H., Lv, X., Li, Y., Wang, Y. & Li, J. P25-Graphene Composite as a High Performance Photocatalyst. *ACS Nano* **4**, 380-386, doi:10.1021/nn901221k (2010).
4. Zou, Z., Ye, J., Sayama, K. & Arakawa, H. Direct splitting of water under visible light irradiation with an oxide semiconductor photocatalyst. *Nature* **414**, 625, doi:10.1038/414625a (2001).
5. Wu, X. *et al.* Upconversion Nanoparticles: A Versatile Solution to Multiscale Biological Imaging. *Bioconjugate Chemistry* **26**, 166-175, doi:10.1021/bc5003967 (2015).
6. Kim, J.-H., Deng, F., Castellano, F. N. & Kim, J.-H. High Efficiency Low-Power Upconverting Soft Materials. *Chemistry of Materials* **24**, 2250-2252, doi:10.1021/cm3012414 (2012).
7. Li, C. *et al.* Photocurrent Enhancement from Solid-State Triplet–Triplet Annihilation Upconversion of Low-Intensity, Low-Energy Photons. *ACS Photonics* **3**, 784-790, doi:10.1021/acsphotonics.5b00694 (2016).
8. van Sark, W. G., de Wild, J., Rath, J. K., Meijerink, A. & Schropp, R. E. I. Upconversion in solar cells. *Nanoscale Research Letters* **8**, 81, doi:10.1186/1556-276X-8-81 (2013).
9. Ramasamy, P., Manivasakan, P. & Kim, J. Upconversion nanophosphors for solar cell applications. *RSC Advances* **4**, 34873-34895, doi:10.1039/C4RA03919J (2014).
10. Hagstrom, A. L., Deng, F. & Kim, J.-H. Enhanced Triplet–Triplet Annihilation Upconversion in Dual-Sensitizer Systems: Translating Broadband Light Absorption to Practical Solid-State Materials. *ACS Photonics* **4**, 127-137, doi:10.1021/acsphotonics.6b00679 (2017).

11. Simon, Y. C. & Weder, C. Low-power photon upconversion through triplet-triplet annihilation in polymers. *Journal of Materials Chemistry* **22**, 20817-20830, doi:10.1039/C2JM33654E (2012).

12. Turshatov, A. *et al.* Room-Temperature High-Efficiency Solid-State Triplet–Triplet Annihilation Up-Conversion in Amorphous Poly(olefin sulfone)s. *ACS Applied Materials & Interfaces* **9**, 8280-8286, doi:10.1021/acsami.6b12625 (2017).

13. Dzebo, D., Moth-Poulsen, K. & Albinsson, B. Robust triplet-triplet annihilation photon upconversion by efficient oxygen scavenging. *Photochemical & Photobiological Sciences* **16**, 1327-1334, doi:10.1039/C7PP00201G (2017).

14. Ogawa, T., Yanai, N., Monguzzi, A. & Kimizuka, N. Highly Efficient Photon Upconversion in Self-Assembled Light-Harvesting Molecular Systems. *Scientific Reports* **5**, 10882, doi:10.1038/srep10882

15. Pincella, F., Isozaki, K. & Miki, K. A visible light-driven plasmonic photocatalyst. *Light: Science &Amp; Applications* **3**, e133, doi:10.1038/lsa.2014.14

16. Mubeen, S., Hernandez-Sosa, G., Moses, D., Lee, J. & Moskovits, M. Plasmonic Photosensitization of a Wide Band Gap Semiconductor: Converting Plasmons to Charge Carriers. *Nano Letters* **11**, 5548-5552, doi:10.1021/nl203457v (2011).

17. Primo, A., Corma, A. & Garcia, H. Titania supported gold nanoparticles as photocatalyst. *Physical Chemistry Chemical Physics* **13**, 886-910, doi:10.1039/C0CP00917B (2011).

18. Liu, Q., Feng, W., Yang, T., Yi, T. & Li, F. Upconversion luminescence imaging of cells and small animals. *Nature Protocols* **8**, 2033, doi:10.1038/nprot.2013.114

19. Liu, Q., Yang, T., Feng, W. & Li, F. Blue-Emissive Upconversion Nanoparticles for Low-Power-Excited Bioimaging in Vivo. *Journal of the American Chemical Society* **134**, 5390-5397, doi:10.1021/ja3003638 (2012).

20. Gray, V. *et al.* Porphyrin–Anthracene Complexes: Potential in Triplet–Triplet Annihilation Upconversion. *The Journal of Physical Chemistry C* **120**, 19018-19026, doi:10.1021/acs.jpcc.6b06298 (2016).

21. Theodorou, I. G. *et al.* Significant metal enhanced fluorescence of Ag2S quantum dots in the second near-infrared window. *Nanoscale* **8**, 12869-12873, doi:10.1039/C6NR03220F (2016).

22. Poorkazem, K., Hesketh, A. V. & Kelly, T. L. Plasmon-Enhanced Triplet–Triplet Annihilation Using Silver Nanoplates. *The Journal of Physical Chemistry C* **118**, 6398-6404, doi:10.1021/jp412223m (2014).

23. Khan, M.A.; Idriss, H., Advances in plasmon-enhanced upconversion luminescence phenomena and their possible effect on light harvesting for energy applications, *WIREs Energy and Environment* 6:e254., DOI: 10.1002/wene.254 (2017)

24. Chen, Y., Munechika, K. & Ginger, D. S. Dependence of Fluorescence Intensity on the Spectral Overlap between Fluorophores and Plasmon Resonant Single Silver Nanoparticles. *Nano Letters* **7**, 690-696, doi:10.1021/nl062795z (2007).

25. Cao, X., Hu, B., Ding, R. & Zhang, P. Plasmon-enhanced homogeneous and heterogeneous triplet-triplet annihilation by gold nanoparticles. *Physical Chemistry Chemical Physics* **17**, 14479-14483, doi:10.1039/C5CP01876E (2015).

26. Westbrook, E. G. & Zhang, P. Plasmon-enhanced triplet-triplet annihilation upconversion of post-modified polymeric acceptors. *Dalton Transactions*, doi:10.1039/C8DT00269J (2018).

27. Geddes, C. D. Metal Enhanced Fluorescence; John Wiley & Sons, Inc.: Hoboken, NJ, 2010

28. Wu, X.-F., Song, H.-Y., Yoon, J.-M., Yu, Y.-T. & Chen, Y.-F. Synthesis of Core−Shell Au@TiO2 Nanoparticles with Truncated Wedge-Shaped Morphology and Their Photocatalytic Properties. *Langmuir* **25**, 6438-6447, doi:10.1021/la900035a (2009).

29. Gao, M., Peh, C. K. N., Pan, Y., Xu, Q.-H. & Ho, G. W. Fine structural tuning of whereabout and clustering of metal-metal oxide heterostructure for optimal photocatalytic enhancement and stability. *Nanoscale* **6**, 12655-12664, doi:10.1039/C4NR03373F (2014).

30. Zhang, N., Liu, S., Fu, X. & Xu, Y.-J. Synthesis of M@TiO2 (M = Au, Pd, Pt) Core–Shell Nanocomposites with Tunable Photoreactivity. *The Journal of Physical Chemistry C* **115**, 9136-9145, doi:10.1021/jp2009989 (2011).

31. Awazu, K. *et al.* A Plasmonic Photocatalyst Consisting of Silver Nanoparticles Embedded in Titanium Dioxide. *Journal of the American Chemical Society* **130**, 1676-1680, doi:10.1021/ja076503n (2008).

32. Ingram, D. B. & Linic, S. Water Splitting on Composite Plasmonic-Metal/Semiconductor Photoelectrodes: Evidence for Selective Plasmon-Induced Formation of Charge Carriers near the Semiconductor Surface. *Journal of the American Chemical Society* **133**, 5202-5205, doi:10.1021/ja200086g (2011).

33. Li, J. *et al.* Plasmon-induced photonic and energy-transfer enhancement of solar water splitting by a hematite nanorod array. *Nature Communications* **4**, 2651, doi:10.1038/ncomms3651

34. Linic, S., Christopher, P. & Ingram, D. B. Plasmonic-metal nanostructures for efficient conversion of solar to chemical energy. *Nature Materials* **10**, 911, doi:10.1038/nmat3151 (2011).

35. Sousa-Castillo, A. *et al.* Boosting Hot Electron-Driven Photocatalysis through Anisotropic Plasmonic Nanoparticles with Hot Spots in Au–TiO2 Nanoarchitectures. *The Journal of Physical Chemistry C* **120**, 11690-11699, doi:10.1021/acs.jpcc.6b02370 (2016).

36. Cushing, S. K. *et al.* Photocatalytic Activity Enhanced by Plasmonic Resonant Energy Transfer from Metal to Semiconductor. *Journal of the American Chemical Society* **134**, 15033-15041, doi:10.1021/ja305603t (2012).

37. Cushing, S. K. *et al.* Controlling Plasmon-Induced Resonance Energy Transfer and Hot Electron Injection Processes in Metal@TiO2 Core–Shell Nanoparticles. *The Journal of Physical Chemistry C* **119**, 16239-16244, doi:10.1021/acs.jpcc.5b03955 (2015).

38. Kale, M. J., Avanesian, T. & Christopher, P. Direct Photocatalysis by Plasmonic Nanostructures. *ACS Catalysis* **4**, 116-128, doi:10.1021/cs400993w (2014).

39. Fei Guo, C., Sun, T., Cao, F., Liu, Q. & Ren, Z. Metallic nanostructures for light trapping in energy-harvesting devices. *Light: Science &Amp; Applications* **3**, e161, doi:10.1038/lsa.2014.42 (2014).

40. Li, J. *et al.* Plasmon-induced photonic and energy-transfer enhancement of solar water splitting by a hematite nanorod array. *Nature Communications* **4**, 2651, doi:10.1038/ncomms3651

41. Minutella, E., Schulz, F. & Lange, H. Excitation-Dependence of Plasmon-Induced Hot Electrons in Gold Nanoparticles. *The Journal of Physical Chemistry Letters* **8**, 4925-4929, doi:10.1021/acs.jpclett.7b02043 (2017).

42. Zhang, Y. *et al.* Surface-Plasmon-Driven Hot Electron Photochemistry. *Chemical Reviews* **118**, 2927-2954, doi:10.1021/acs.chemrev.7b00430 (2018).

43. Wang, H., You, T., Shi, W., Li, J. & Guo, L. Au/TiO2/Au as a Plasmonic Coupling Photocatalyst. *The Journal of Physical Chemistry C* **116**, 6490-6494, doi:10.1021/jp212303q (2012).

44. Liz-Marzán, L. M. Tailoring Surface Plasmons through the Morphology and Assembly of Metal Nanoparticles. *Langmuir* **22**, 32-41, doi:10.1021/la0513353 (2006).

45. Xie, F., Centeno, A., Ryan, M. R., Riley, D. J. & Alford, N. M. Au nanostructures by colloidal lithography: from quenching to extensive fluorescence enhancement. *Journal of Materials Chemistry B* **1**, 536-543, doi:10.1039/C2TB00278G (2013)

46. Zhao, J., Ji, S. & Guo, H. Triplet–triplet annihilation based upconversion: from triplet sensitizers and triplet acceptors to upconversion quantum yields. *RSC Advances* 1, 937-950, doi:10.1039/C1RA00469G (2011).

Chapter 7 Summary and future works

7.1 Summary

Plasmon-enhanced upconversion has attracted tremendous research interests in applications of solar energy harvesting and biomedical technologies. The PhD work demonstrated that the intrinsic upconversion efficiency of lanthanide-based upconversion and triplet-triplet annihilation based upconversion nanoparticles, can be dramatically enhanced by novel plasmonic nanostructures under optimized conditions. In this thesis, the properties of lanthanide-doped upconversion nanoparticles were firstly investigated. Several synthesis methods and Gd^{3+} doping strategy were applied to obtain UCNPs with different sizes, phases, upconversion quantum yields and selective lifetimes. These initial results laid the foundation of further studies. In chapter 4, mesoporous Au film substrates were used to enhance the UCPL of UCNP, with promising 41-fold enhancement achieved. The enhancement mechanisms were investigated experimentally and simulated by FDTD method. Furthermore, the designer plasmonic structures with chemically stable, reproducible and optically highly tunable properties were further fabricated, including nanotriangle arrays, nanohole arrays and the nanostructures coupled with Au and silica films as bottom layer and spacer layer, respectively. Nanoscale engineering were carried out to place the UCNPs in the hot spots of the optimized Au nanostructures that would produce significant enhancement factors. These structures could achieve reliable and dramatic UCPL enhancement in steady state photoluminescence measurement. In chapter 6, given the knowledge gained in previous chapters, we designed a photocatalytic system that could take advantages of both plasmonic and upconversion mechanisms to achieve broadband solar light absorption for as much as 5 times faster photocatalytic activity compared to benchmark sample, $Au@TiO_2$ product.

In summary, this work explored the properties of upconversion nanoparticles (UCNPs), especially upconversion photoluminescence (UCPL) and its enhancement by novel plasmonic nanostructures, including mesoporous film and periodic nanotriangle/nanohole arrays deposited on flat Au. Furthermore, the high efficiency TTA-UCNPs combined with plasmonic nanostructure realized remarkable photocatalytic activity enhancement compared to benchmark sample. These results demonstrated UCPL can be dramatically enhanced by plasmonic nanostructures and their great potential in sunlight harvesting.

7.2 Future works

With exciting discoveries and stimulating experimental achievements, there remains great room to be explored and improved.

1. The search for highly efficient of rare-earth based upconversion nanoparticles has been a topic that last for decades in the world. Although so many efforts have been conducted by researchers, there is still no breakthrough to tackle the problem of intrinsic low upconversion efficiency.

2. Plasmonic nanostructures allows great opportunities for the enhancement of UCPL, however, there are great potential to further improve the performance of UCPL by designing more advanced plasmonic nanostructure. In addition, some mechanisms remain unclear, including the energy transfer between plasmonic nanostructures and upconversion nanoparticles, the quantitively characterizations of contributions from absorption enhancement and emission enhancement, *et al*.

3. Triplet-triplet annihilation UCNPs represents a novel upconversion materials, which demonstrated high intrinsic upconversion efficiency compared to lanthanide-based UCNPs. However, the combination of TTA-UCNPs and TiO_2 should not be an excellent photocatalytic system owing to the very limited spectral overlap between the emissions of TTA-UCNPs and the absorption of TiO_2 nanoparticles. There are two ways to solve this drawback, 1. synthesis different TTA-UCNPs with emissions in ultraviolet ranges. 2. Apply different semiconductors with higher band energies to meet the emission spectra of TTA-UCNPs.

Moreover, it would be a very fascinating topic to synthesis UCNPs that are conductive and with even higher upconversion efficiency, in order to maximize the performance of upconversion nanoparticles in solar energy devices. I truly hope the studies in this thesis could push forward the field of plasmon-enhanced upconversion related technologies and sciences.